INFORMATION TO USERS

NOTE TO USERS

The original manuscript received by UMI contains light print. All efforts were made to acquire the highest quality manuscript from the author or school. Page(s) were microfilmed as received.

This reproduction is the best copy available

UMI

Electrodeposition of NiFe 3-D Microstructures

by

Steven D. Leith

.

A dissertation submitted in partial fulfillment of the
requirements for the degree of

Doctor of Philosophy

University of Washington

1998

Approved by _____
Chairperson of Supervisory Committee

_____

_____

_____

Program Authorized
to Offer Degree _____ Department of Chemical Engineering _____

Date _____ November 23, 1998 _____

UMI Number: 9916684

UMI
300 North Zeeb Road
Ann Arbor, MI 48103

In presenting this dissertation in partial fulfillment of the requirements for the Doctoral degree at the University of Washington, I agree that the Library shall make its copies freely available for inspection. I further agree that extensive copying of this dissertation is allowable only for scholarly purposes, consistent with "fair use" as prescribed in the U.S. Copyright Law. Requests for copying or reproduction of this dissertation may be referred to University Microfilms, 1490 Eisenhower Place, P.O. Box 975, Ann Arbor, MI 48106, to whom the author has granted "the right to reproduce and sell (a) copies of the manuscript in microform and/or (b) printed copies of the manuscript made from microform."

Signature _____

Date _____

University of Washington

Abstract

Electrodeposition of NiFe 3-D Microstructures

by Steven D. Leith

Chairperson of the Supervisory Committee: Associate Professor Daniel T. Schwartz
Department of Chemical Engineering

Many microelectromechanical systems incorporate magnetic materials such as electrodeposited NiFe in electromagnetically driven microactuators.   In these applications, the compositional structure of the NiFe deposit has a great impact on device performance. Thus, control of alloy composition during deposition is an important processing challenge. In this study, we report on the development of an electrodeposition process which allows the tailoring of the compositional structure in electrodeposited NiFe microstructures. Through fabrication of an electroplating device and control of plating electrolyte chemistry and mass transfer at the cathode surface we achieve unprecedented control of alloy composition. To illustrate the process, we first electrodeposit NiFe microstructures with uniform composition. Through understanding and continual optimization of the process, we realize greatly improved deposition rates and yields while maintaining compositional uniformity in geometrically complex microstructures. In the second part of the study, we use composition control to demonstrate the fabrication of new materials with spatially modulated composition. Precise spatial control of NiFe alloy composition allows creation of 3-dimensional electrodeposited NiFe microstructures.

Table of Contents

List of Figures

List of Tables

Acknowledgments

I would first like to thank my advisor, Dan Schwartz, for his guidance over the past four years. Dan's enthusiasm for my project and continual encouragement have made my experience at UW truly enjoyable. I would welcome the opportunity and would be privileged to work with him again. Many others in the department have had a direct impact on my research as well. I would like to thank my colleagues in Dan's research group (past and present) for their assistance and support as well as those in other research groups (you know who you are) who have contributed time and expertise.

Others have made significant contributions as well, but their efforts will not necessarily show up in the final boxscore. These unsung heroes primarily concerned themselves with improving my life outside of school, although some made technical suggestions as well. In no particular order I would like to thank Phil and Amy, Todd and Tera, Jeff and Tanya, Dani and Craig, Brian and Debbie, Mom and Dad, Bob and Carolyn and John Boy. Without your love and support, life wouldn't be much fun and the last four years would not have been nearly as enjoyable as they were. I would also like to give a big thank you to my beautiful wife Mary. You have always been there for me and I appreciate your loving support and understanding throughout the course of this adventure.

CHAPTER 1

Introduction

Through-Mold Electrodeposition of NiFe Alloys

Electrodeposited NiFe alloys ranging in composition from Permalloy ($Ni_{81}Fe_{19}$) to Invar ($Ni_{36}Fe_{64}$) exhibit a spectrum of magnetic and mechanical properties that have led to the widespread use of these materials in a variety of high technology applications [1-4]. For example, many magnetic microactuators and inductors such as solenoids, valves and cantilevers are fabricated by electrodeposition of Permalloy through patterned insulating molds [5-8]. The magnetic, mechanical and corrosion properties of NiFe electrodeposits are dictated by the metallurgical structure (*e.g.* grain size and growth orientation) and alloy composition [2, 9-11]. In turn, these parameters are affected by processing variables such as plating bath chemistry, pH and temperature as well as applied current density and electrolyte mixing conditions at the cathode surface [2, 12, 13]. While bath chemistry, pH and temperature can usually be controlled, significant variations in local current density and electrolyte mixing often occur during plating (especially in patterned molds), leading to non-uniformities in deposit composition. Deposition of NiFe alloys with engineered properties, therefore, depends in large part on minimizing non-uniformity in electrode polarization and electrolyte mixing during plating.

Length Scales

In general, plating microstructures through patterned molds requires consideration of current distribution and mass transfer characteristics on length scales associated with the workpiece, the molded pattern and individual molded features [14-19, 20]. The workpiece scale is the dimension characteristic of the entire object undergoing electrodeposition. An example of the workpiece scale is an entire patterned wafer. Typical dimensions of this scale are on the order of centimeters. Uniformity at the workpiece length scale is primarily governed by the design and operation of the electroplating device. The pattern scale is defined by regions on the workpiece surface that differ in distribution and density of electroactive area as defined by the patterned mold. Non-uniformities arise when different areas of the surface exhibit different densities or distribution of patterning. Adjacent regions of high and low active area

density can result in current distribution variations from one region to the next. In addition, the presence of the patterned mold can disrupt the concentration boundary layer. Typical dimensions of this scale are from 100's of microns to a few millimeters. To a great extent, uniformity on the pattern scale is dictated by the geometry of the molded layout. The feature scale is on the order of microns and represents the smallest patterned geometries on the wafer. Adequate control of electrolyte mixing and current density on this scale is often not possible due to physical constraints on mass transfer processes and current distribution characteristics [20]. For this reason, feature scale uniformity is arguably the most difficult to achieve. This idea of multiple length scales is illustrated schematically in Fig. 1.1 for a wafer patterned with rectangular features.

Workpiece   Pattern   Feature

cm   mm   μm
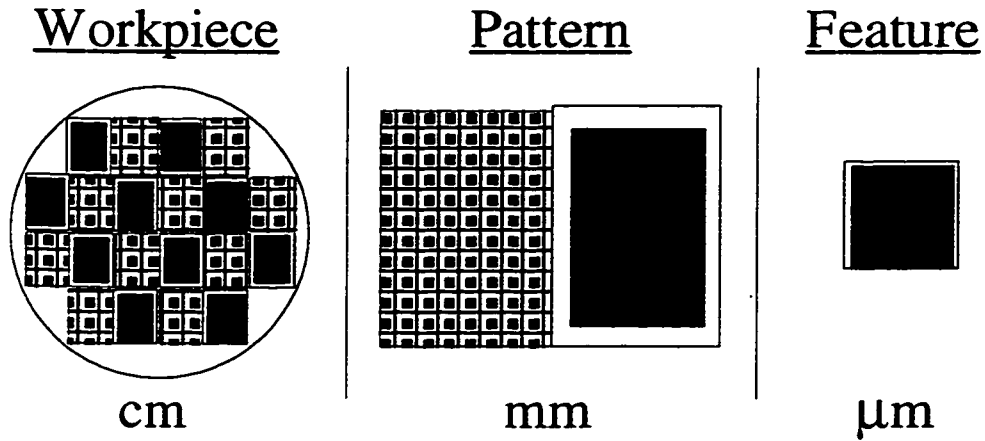
Figure 1.1. Conceptual illustration of the three length scales typically considered in through-mold electrodeposition.

Current Distribution

Potential-theory models allow the current distribution at every length scale to be determined [21]. Current distribution is related to potential through a form of Ohm's law:

$$i = -\kappa \frac{\delta \Phi}{\delta \mathbf{n}}$$

(1.1)

where κ is the conductivity of the electrolyte, Φ is the potential and $\mathbf{n}$ is a unit normal vector. The potential field is defined by Laplace's equation and boundary conditions :

$$\nabla^2 \Phi = 0 \tag{1.2}$$

$$\frac{\delta\Phi}{\delta n} = 0 \quad @ \text{ insulating surfaces and lines of symmetry} \tag{1.3}$$

$$\Phi = E - \eta \quad @ \text{ electroactive surfaces} \tag{1.4}$$

where E is the electrode potential and η is the total overpotential. For the reaction

$$O + ne^- \leftrightarrow R \tag{1.5}$$

the current-potential relationship can be represented by

$$i = i_o \left\{ \left(\frac{C_s}{C_b}\right)_R e^{\frac{\alpha_a F \eta}{RT}} - \left(\frac{C_s}{C_b}\right)_O e^{\frac{-\alpha_c F \eta}{RT}} \right\} \tag{1.6}$$

where i_o is the exchange current density, α_a and α_c are kinetic transfer coefficients, C_s and C_b are the surface and bulk concentrations of reactive species O and R, F is Faraday's constant, R is the gas constant and T is temperature. A number of researchers have used this approach to model the effects of a molded pattern on current distribution for a variety of simple mold geometries (*e.g.* holes and trenches) [15-19, 20]. These types of studies have been valuable in illustrating general strategies for minimizing pattern and feature scale non-uniformity in current distribution. The overriding principle is to create a pattern in which the density of electroactive area is maximized and evenly distributed across the wafer and between patterned features. To simplify the problem, however, these analyses typically ignore the effects of mass transfer (*i.e.* $C_s = C_b$ in Eq. (1.6)) or approximate its influence [17, 18]. The effects of electrolyte mixing, especially at the feature length scale, are absent from nearly all theoretical work. In the specific case of NiFe deposition, modeling efforts are further complicated by the non-ideal deposition kinetics of NiFe, characterized by so-called anomalous codeposition in which the less

noble species (iron) preferentially deposits over the more noble species (nickel). Even though a large body of work has been dedicated to investigation of this phenomena, the deposition mechanism remains subject to some uncertainty [22-24].

The shortcomings of modeling through-mold deposition of NiFe suggest that experimental studies are needed to explore the issues affecting deposit uniformity. Much work has been devoted to optimization of through-mold plating of uniform $Ni_{81}Fe_{19}$ deposits for use in magnetic data storage devices, but this previous work has generally focused on plating through relatively thin photoresist molds (< 5 μm thick) [2, 4]. With the increased interest in fabrication of much thicker (> 250 μm), high aspect ratio ($>10:1$) NiFe structures of different compositions for microelectromechanical systems (MEMS), there exists a need for development of an electrodeposition strategy suitable for these types of structures.

Objectives and Approach (Chapters 2 - 4)

The primary focus of this dissertation is to address uniformity across the three length scales through development and optimization of a through-mold plating process for fabrication of NiFe microstructures with controlled and uniform composition. The basic strategy is illustrated in Fig. 1.2. We first develop and characterize the performance of a NiFe plating bath in a systematic study using a well understood electrochemical cell. Relationships between current density, mass transfer and deposit composition are thoroughly explored for a variety of bath formulations. Next, we design, fabricate and characterize the performance of a plating device suitable for through-mold plating with primary consideration given to uniformity of current distribution and mass transfer on the workpiece length scale. The final aspect of the study explores pattern and feature scale uniformity through experimental investigation of composition variation in electrodeposited NiFe microstructures with geometrically complex features. Using results from the plating bath characterization, we then illustrate how compositional variation at these length scales can be minimized.

3-Dimensional Microstructures

While the mass transfer sensitivity of electrodeposited NiFe represents a challenge in plating microstructures with uniform composition, the ever expanding use of NiFe in fabrication of MEMS presents an opportunity to exploit this characteristic to aid in
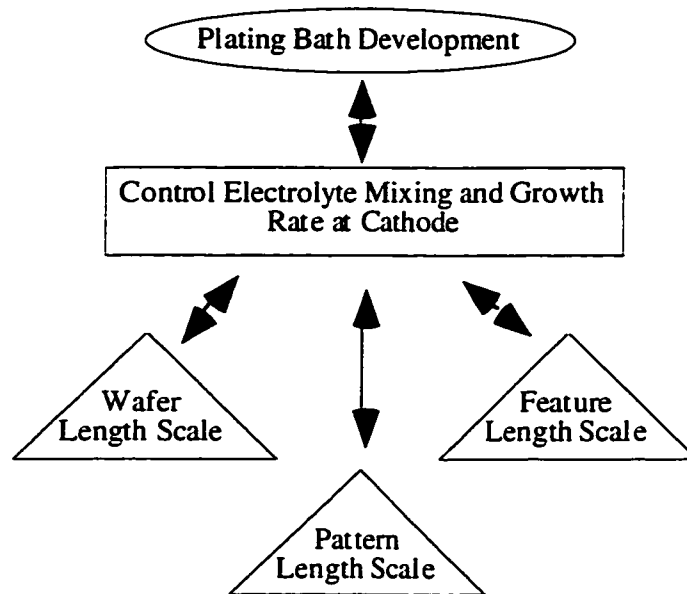
Figure 1.2. Research strategy for the development and optimization of a through-mold plating process for fabrication of NiFe microstructures with controlled and uniform composition.

engineering of 3-dimensional microstructures. The plating-through-mold technique discussed above allows fabrication of *quasi* 3-dimensional structures. Essentially, a 2-dimensional structure is defined by the pattern which is then expanded into the third dimension as deposition proceeds. Fabrication of truly 3-dimensional structures - ones in which the geometry varies in the vertical dimension - typically requires the use of sacrificial layers. A common characteristic of fabricating structures using sacrificial layers is the requirement to "build" the structure layer-by-layer using a time consuming repetition of masking, exposure, deposition and etching. Figure 1.3 shows the general steps needed to build a 3-dimensional structure. To create the final beam structure shown in (E), two masking, two deposition and three etching steps are involved. This general technique is routinely used in fabrication of geometrically complex microstructures, but, as illustrated, there is an associated cost in terms of time and materials [3, 25, 26].

The formation of sacrificial layers *in-situ* as the microstructure is deposited would represent a significant improvement in the fabrication procedure, eliminating additional masking, exposure and deposition steps. To have utility as a viable micromaching technique, such as process would have to 1) enable deposition of well-defined layers of
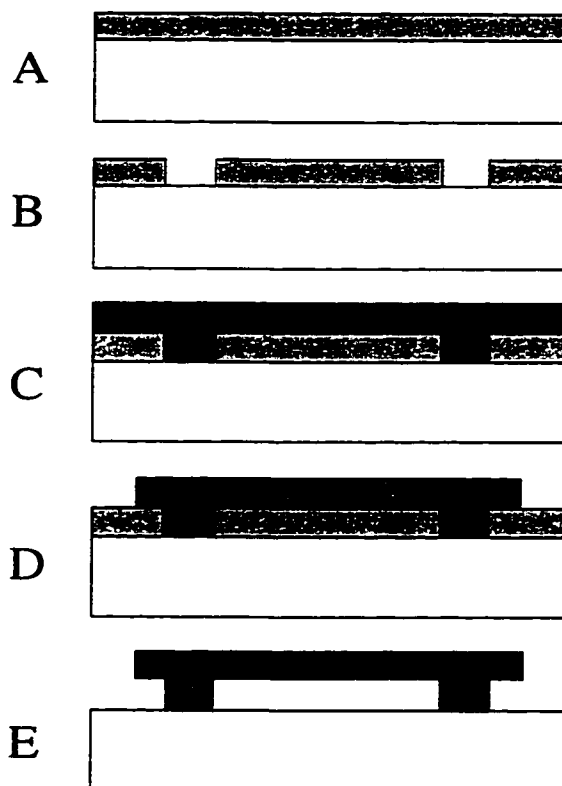
Figure 1.3. General technique used to build a 3-dimensional microstructure. (A) Sacrificial layer deposition. (B) Pattern with mask #1 and etch. (C) Deposition of structural material. (D) Pattern with mask #2 and etch. (E) Final etch of sacrificial layer.

sacrificial and non-sacrificial material and 2) exhibit selective etching for controlled removal of sacrificial material with minimal alteration of non-sacrificial structures. In typical fabrication processes (such as that illustrated in Fig. 1.3), the sacrificial material is chosen such that preferential removal is possible. Commonly this requires the sacrificial and non-sacrificial layers to be of different materials, such as copper and nickel [3, 25]. It is possible, however, to achieve selectivity in etching through alloying. This principle could, in theory, be applied to creation of NiFe sacrificial layers if one could create layers of iron-rich and nickel-rich alloy in a controlled manner *and* if one alloy was susceptible to preferential etching. One technique used to make layered structures of differing and controlled alloy composition is the electrodeposition of composition modulated alloys (CMAs).

Figure 1.4 is a schematic illustrating the general features of a CMA composed of metals A and B. As the figure shows, the interface between successive layers can be discrete or diffuse and the composition does not necessarily vary from pure species A to pure species B. Electrodeposited CMAs are made by modulating the deposition rate of one or more species through either 1) time periodic variation in deposition current (or potential), 2) modulation of the convective mass transfer rate or 3) a combination of pulsed current and modulated electrolyte flow. The electrodeposition of CMAs made from NiCu, AgPd, NiMo, CoCu and Cu/NiFe by methods 1 and 3 are well established [27-35]. CMAs made by galvanostatic deposition in a periodic or pulsed mass transfer environment are called flow-induced CMAs and fabrication requires that alloy composition exhibits a sensitivity to mass transfer. Specifically, the requirement is that one species deposits at its mass transfer limited rate and another species deposits under kinetic control. As discussed later, it is well established that the deposition of NiFe alloys is characterized by the mass transfer limited plating of iron and the deposition of nickel under kinetic control [12]. Thus, the basic criteria for electrodepositing flow-induced CMAs are satisfied by NiFe plating. What remains to be demonstrated, however, is the ability to deposit NiFe CMAs with controlled and predictable compositional structure by periodic modulation of mass transfer conditions. In addition, it has yet to be shown that one NiFe CMA layer can be selectively etched while the structural fidelity of another is retained.
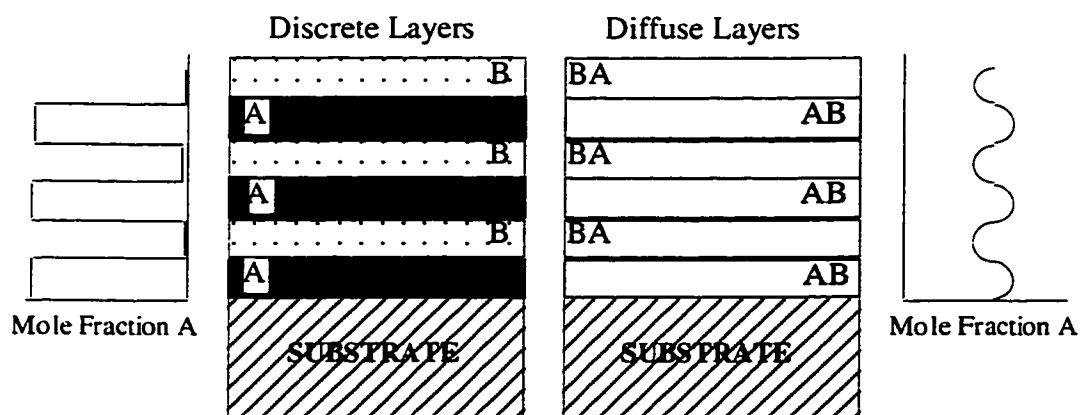
Figure 1.4. General features of a composition modulated alloy (CMA) composed of metals A and B.

Objectives and Approach (Chapters 5 and 6)

A secondary research objective of this dissertation is to develop a technique for electrodeposition of microstructures with *in-situ* sacrificial layers based on the concept of flow-induced NiFe CMAs. We first explore the possibilities of plating NiFe alloys with a spatially periodic composition variation in one dimension by time-periodic modulation of convective-diffusive mass transfer in a well understood electrochemical cell. We use this systematic study to define clear relationships between processing variables and the resulting compositional structure. These results are applied to create flow-induced composition modulated NiFe microstructures. Techniques for preferential etching of sacrificial layers based on alloy composition are then investigated.

Present Work

Chapter 2 describes the development and operating characteristics of a family of plating electrolytes for electrodeposition of NiFe alloys over a wide range of compositions and growth rates. Chapter 3 details the construction, operation and characterization of a new plating device suitable for through-mold plating of microstructures. Workpiece and pattern scale uniformity issues are explored using the device to electrodeposit NiFe microgears through a patterned mold. Chapter 4 further investigates plating of NiFe microstructures with focus on the minimization of feature scale non-uniformities. In Chapter 5, the results of Chapter 2 are expanded to explore plating of NiFe alloys using time periodic convective mass transfer conditions. Chapter 6 illustrates a technique for *in-situ* fabrication of sacrificial layers in electrodeposited NiFe microstructures based on the results of Chapter 5. In Chapter 7, general conclusions and recommendations for future work are presented. One appendix is included which describes an early study investigating the effects of an oscillating electrolyte flow field on composition in electrodeposited NiFe alloys.

CHAPTER 2

Characterization of Ni_xFe_{1-x} (0.10 < x < 0.95) Electrodeposition from a Family of Sulfamate-Chloride Electrolytes

Summary

In this chapter, the characteristics of a nickel sulfamate/iron chloride plating bath suitable for high rate electrodeposition of NiFe alloys are described. The effects of current density, electrolyte agitation and Ni^{+2}/Fe^{+2} content on deposit composition and plating current efficiency are explored via stripping voltammetry using a rotating ring-disk electrode (RRDE). Specific plating bath formulations and operating conditions for depositing a wide range of alloy compositions at a variety of growth rates are illustrated. Special attention is given to determination of polarization and electrolyte mixing conditions for plating Permalloy and Invar. X-ray diffraction (XRD) studies are used to investigate relationships between alloy composition and crystal structure. The implications for using the plating bath to electroplate composition modulated alloys (CMAs) and 3-D microstructures are discussed.

Background

NiFe alloys ranging in composition from Permalloy ($Ni_{81}Fe_{19}$) to Invar ($Ni_{36}Fe_{64}$) exhibit a spectrum of physical properties that have led to the widespread use of these materials in a variety of high technology applications [1-4]. The recent emergence of microstructure and microsystem fabrication by electroplating through thick patterned molds (e.g. LIGA processing) illustrates the potential for new and challenging NiFe plating applications. For example, many magnetic microactuators and inductors such as solenoids, valves and cantilevers are fabricated using electrodeposited Permalloy [5-8]. In addition, electrodeposited Invar structures have been studied for use as servo actuators for magnetic recording heads, an application in which dimensional stability over a wide temperature range is required [36].

The magnetic, mechanical and corrosion properties of NiFe electrodeposits are dictated by a number of factors including metallurgical structure (e.g. grain size, growth orientation) and alloy composition [2, 9-11]. In turn, these parameters are affected by processing variables such as plating bath chemistry, pH and temperature as well as the

applied current density and electrolyte mixing conditions at the cathode surface [2, 12, 13]. While bath chemistry, pH and temperature can usually be controlled, significant variations in current density and electrolyte mixing often occur during plating (especially in patterned molds), leading to non-uniformities in deposit composition. Deposition of NiFe alloys with predictable properties, therefore, depends in large part on understanding the effects of electrode polarization and electrolyte mixing on the composition of the deposit.

Numerous NiFe plating bath recipes have been proposed over the past 20 years and the roles of various salts and organic additives have been investigated [2]. Much of this previous work has been directed at understanding the anomalous codeposition phenomena of NiFe [22-24, 37-40]. The focus of this study, however, is not anomalous codeposition, but rather the development and performance characterization of a versatile NiFe plating bath.

The family of plating baths described here are a higher pH and lower total metals analog to the sulfamate/chloride bath used by Grimmett *et al.* [13, 41]. In these earlier studies, the effects of temperature and current waveform (direct, pulsed and pulse reverse) on the NiFe deposit composition, structure and mechanical properties were thoroughly investigated using planar and cylindrical electrodes. In the studies described here, we expand on the work of Grimmett *et al.* in two important ways. First, we consider in detail the role of electrolyte agitation on the deposit composition. Though Grimmett *et al.* did analyze a number of different hydrodynamic conditions, this was not the focus of their work. Nonetheless, it is well known that the composition of electrodeposited NiFe is very sensitive to electrolyte mixing [12, 42]. Second, we consider an electrolyte that is lower in total metals content and of higher pH than the sulfamate/chloride bath used by Grimmett *et al..* Plating with this bath ensures high current efficiencies (≥ 0.60) for all electrolyte mixing conditions of interest, whereas with the Grimmett bath we often measured current efficiencies as low as 40% when plating thin films onto a platinum substrate. In through-mold plating of high aspect ratio microstructures, low current efficiencies can lead to pit defects in plated parts [43].

In the studies described here, the effects of current density, electrolyte agitation and Ni^{+2}/Fe^{+2} content on deposit composition and plating current efficiency are explored

via stripping voltammetry using a rotating ring-disk electrode (RRDE). Due to their many technological applications, specific conditions for electroplating Permalloy and Invar are highlighted. X-ray diffraction (XRD) studies are used to investigate the effects of alloy composition on crystal structure and to illustrate the metallurgical similarities between deposits plated in this study and those made by others.

Experimental

A Pine Instruments RRDE with a platinum disk of radius $r_1=0.229$ cm and concentric platinum ring with inner radius $r_2=0.246$ and outer radius $r_3=0.269$ was used for all electroplating and stripping voltammetry experiments. The RRDE, a large area platinum mesh counter electrode and a saturated calomel (SCE) reference electrode were used in single chambered 500 ml electroplating and stripping vessels. A Pine instruments Model MSRX rotator was used to control the steady rotation rate of the RRDE. A Pine Instruments Model AFRDE5 Bi-Potentiostat was used to control the disk and ring polarization during plating and stripping. During stripping, disk and ring currents were monitored continuously using a Macintosh Centris 650 personal computer interfaced with the bi-potentiostat through a National Instruments 12 bit multi-function A/D board. Disk and ring current acquisition and calculation of the alloy composition were performed using custom software written in the LABVIEW programming environment.

Five different plating bath formulations were investigated. Each contained nickel sulfamate and iron chloride as the metal salts, with the molar ratio of Ni:Fe in the electrolyte varying between individual baths. Plating baths with Ni:Fe molar ratios of 25:1, 20:1, 15:1, 10:1 and 5:1 were prepared using reagent grade chemicals and 18 MΩ-cm distilled water. Every bath was composed of 0.2 M $Ni(H_2NSO_3)_2 \cdot 4$ H_2O, 0.40 M H_3BO_3, 1.5 g/l sodium saccharin, 0.2 g/l sodium dodecyl sulfate and 1.0 g/l ascorbic acid. An appropriate mass of $FeCl_2 \cdot 4$ H_2O was added to each bath to satisfy the specified dissolved metals molar ratio, e.g. 0.01 M $FeCl_2 \cdot 4$ H_2O in the 20:1 plating bath, 0.02 M in the 10:1 bath and so on. Each bath was operated at room temperature (~23 °C) and pH was kept constant at 3.00 +/- 0.01 by addition of HCl and/or NaOH between plating runs. The stripping bath composition was 0.2 M HCl and 0.5 M NaCl and was also operated at room temperature. For comparison, the sulfamate/chloride plating bath investigated by Grimmett et al. contained 1.0 M total dissolved metals with a Ni:Fe ratio of 3:1 and was operated at pH = 2 at 25 or 54 °C.

Prior to each plating run, the disk and ring electrodes were cleaned by cyclic potential scanning at 100 mV/s between -300 and +1300 mV vs. SCE for approximately 15 minutes in a 0.2 M HCl / 0.5 M NaCl electrolyte. After cleaning, NiFe thin films were electroplated galvanostatically onto the disk of the RRDE until a total charge of 500 to 1200 mC had passed, resulting in deposits between 0.6 and 2.1 μm thick. During plating, the ring potential was set to +800 mV vs. SCE to prevent metal deposition on the ring. After each plating run, the RRDE was removed from the plating bath, immersed in deionized water and rotated to prevent contamination of the stripping bath. The RRDE was then submerged in the stripping solution and rotated at a constant rate of 2500 rpm. The disk potential was set to 0 mV vs. SCE to oxidize the alloy, liberating Ni^{+2} and Fe^{+2} from the film surface. The ring potential was set to +800 mV vs. SCE to detect Fe^{+2} via the mass transfer limited reaction $Fe^{+2} \rightarrow Fe^{+3}$. The disk and ring currents were recorded continuously during stripping to allow determination of the deposit composition and plating current efficiency. The average composition of each alloy was calculated from the stripping data using the relationship

$$X_{Fe} = \frac{2}{N} \frac{Q_{R.S}}{Q_{D.S}} \quad , \tag{2.1}$$

where X_{Fe} is the average mole fraction iron in the deposit, N is the collection efficiency of the RRDE (N=0.217), $Q_{R.S}$ is the total charge at the ring during stripping, and $Q_{D.S}$ is the total charge at the disk during stripping [44]. The plating current efficiency, ε_p, for deposition of each alloy was determined from coulombic measurements using the relationship

$$\varepsilon_p = \frac{Q_{D.S}}{Q_{D.P}}, \tag{2.2}$$

where $Q_{D.S}$ is as defined above and $Q_{D.P}$ is the total charge on the disk during plating. The performance of each plating bath was characterized using a wide range of electrolyte mixing conditions and current densities. NiFe alloys were deposited onto the disk of the RRDE at rotation rates of 100, 400, 900, 1600, 2500, and 3600 rpm and current densities

of -20, -40, -60, -80, -100 mA/cm^2. In determination of Permalloy plating conditions, a number of disk rotation rates greater than 3600 rpm and current densities higher than -100 mA/cm^2 were investigated as well. To facilitate the application of our results to the deposition of NiFe using other plating cells, electrolyte mixing is reported here using a general mass transfer coefficient, k, which is related to the disk rotation rate through the Levich equation [45]

$$k = 0.62 \Omega^{1/2} D^{2/3} v^{-1/6}, \qquad\qquad (2.3)$$

where Ω is the rotation rate of the RRDE during plating, D is the diffusivity of the depositing species (here we use 4.7 x 10^{-6} cm^2/s for Fe^{+2} as determined in an earlier study [46]) and v is the kinematic viscosity of the electrolyte (0.011 cm^2/s).

Using the same potentiostat, rotator and plating bath described above, NiFe alloys were also deposited onto the removable disk of a rotating disk electrode (RDE). Prior to plating, the removable platinum disk electrode (radius = 0.25 cm) was cleaned by cyclic potential scanning and then rinsed with deionized water. The platinum RDE was then placed in a single chambered electroplating vessel with SCE reference electrode and platinum mesh counter electrode. NiFe alloys were plated onto the RDE using an applied current density of -20 mA/cm^2 until a charge of approximately 4100 mC had passed, resulting in a deposit 5 μm thick on average. Alloys were plated with compositions ranging from 10 to 75 mol% iron. After plating, the platinum disk electrode was removed from the RDE housing and X-ray diffraction patterns for each alloy were recorded using a computer-controlled Philips PW 1830 diffractometer with Cu K$_\alpha$ radiation.

Results and Discussion

Figure 2.1 shows a typical stripping voltammogram of an electrodeposited NiFe film. The particular film in Fig. 2.1 was plated from the 15:1 bath at -40 mA/cm^2 and k = 0.0024 cm/s (Ω = 400 rpm), but the general features of the voltammogram are representative of those from the other deposits investigated in the study. The figure shows that the disk current (top curve) rises at the onset of stripping and remains constant as the film is oxidized from the disk. The ring current (bottom curve) responds to and mirrors the disk current as Fe^{+2} liberated from the disk is detected at the ring. At the end
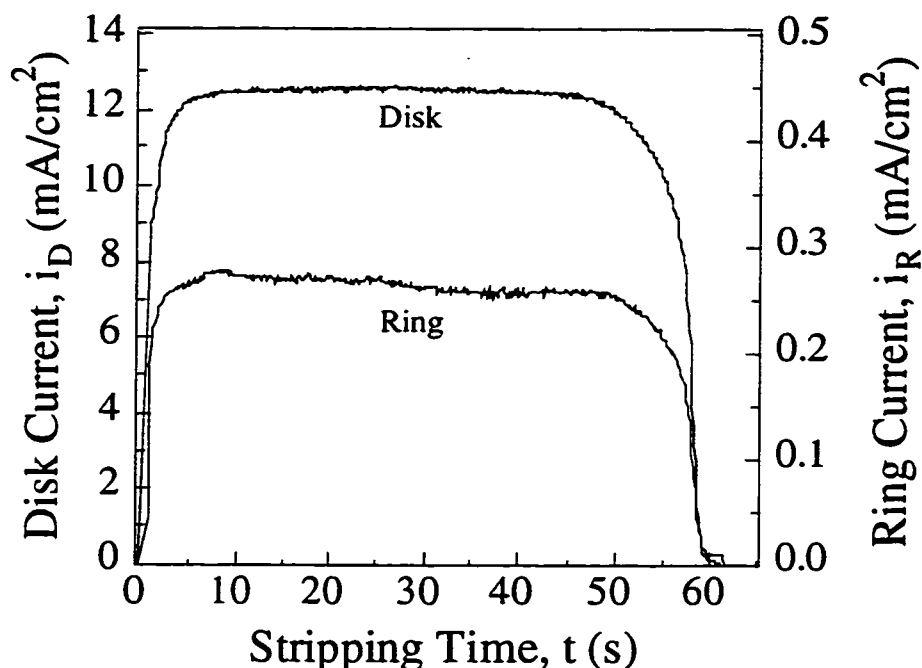
Figure 2.1. Typical stripping voltammogram of an electrodeposited NiFe film. The measured disk and ring currents are shown as a function of stripping time. The average composition of the film is determined from the time-integrated disk and ring currents using Eq. (2.1).

of stripping, the disk and then the ring current falls to zero. From the integrated disk and ring currents in Fig. 2.1, the average composition of this particular film was determined to be 20 mol% iron using Eq. (2.1).

Figure 2.2 was constructed from over 150 stripping voltammetry experiments and summarizes the characterization results for all five plating bath formulations. Here the effects of plating current density, electrolyte agitation and Ni^{+2}/Fe^{+2} content on average deposit composition are illustrated. A number of trends are evident between and within the different plating baths. In all bath formulations, the average mole fraction of iron in the deposit increases with agitation. In some instances, the flow sensitivity is quite significant. Consider, for example, plating with the 10:1 bath. Deposition from this bath at a rate of -20 mA/cm² allows plating of films with an iron composition as low as 27 mol% or as high as 80 mol%. Increase the current density to -40 mA/cm² and the compositions range from 16 mol% to 65 mol% iron. In all conditions shown, the mole fraction of iron is linear with agitation rate at high current densities, displaying a Levich-
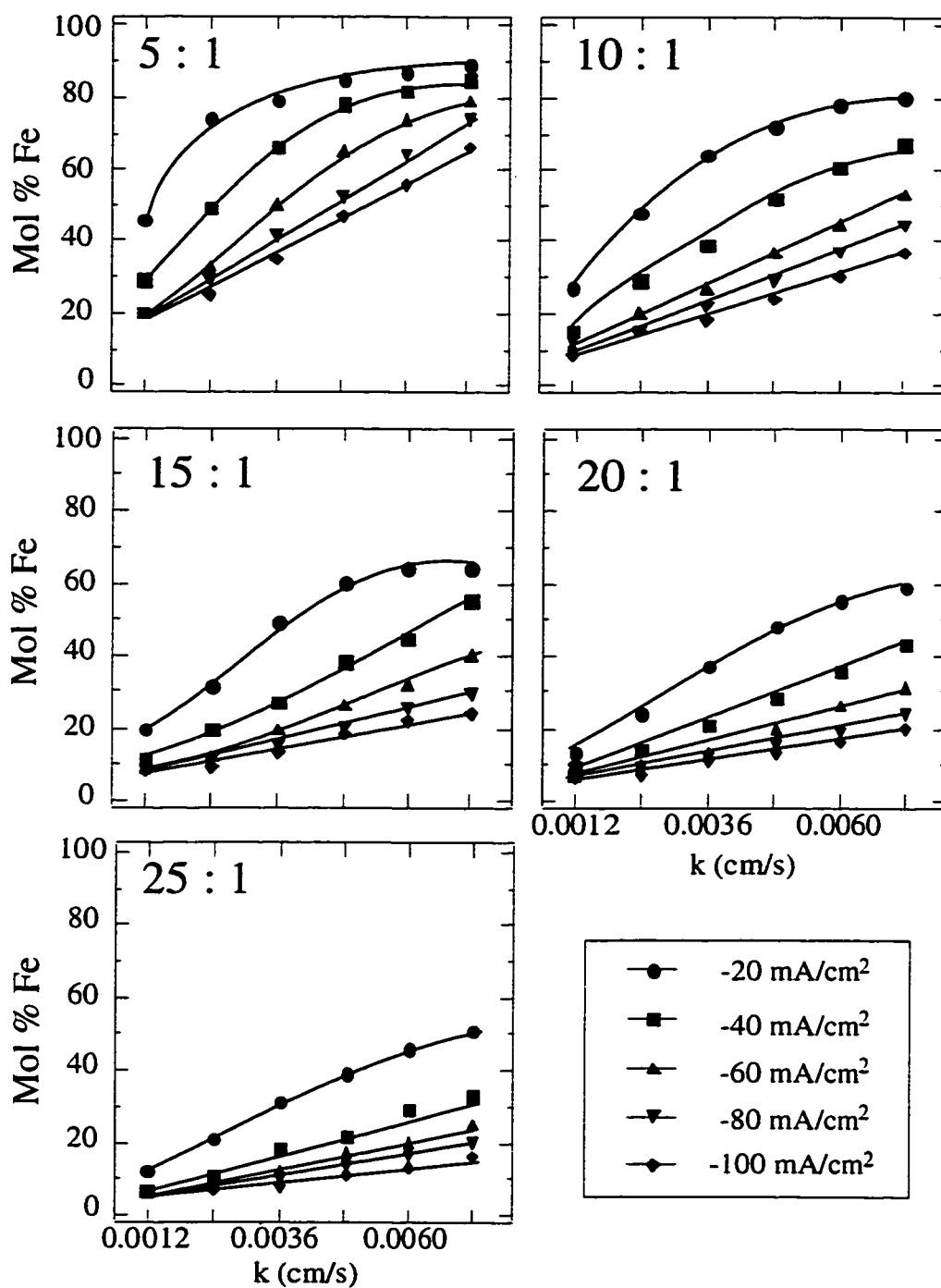
Figure 2.2. The effect of current density and electrolyte agitation on deposit composition for the family of sulfamate/chloride electrolytes. The dissolved Ni^{+2}:Fe^{+2} molar concentration ratio in the five baths varies from 5:1 to 25:1 as indicated.

like mass transfer limitation for iron deposition. At lower current densities, however, the flow dependence appears to be controlled by a more complex, coupled kinetic-mass transfer mechanism. These results for the 10:1 bath are consistent with the other electrolyte formulations as well. Figure 2.2 also illustrates that the effects of agitation vary between the different plating baths. In general, the baths with relatively more iron in solution (e.g. the 5:1 and 10:1 baths) are more sensitive to flow than the baths containing less iron (e.g. the 20:1 and 25:1 baths).

The composition of the deposit and the flow sensitivity of the process are also strongly affected by the plating rate. Under constant mass transfer conditions, the average mole fraction of iron in the deposit decreases with an increase in applied current density. Without exception, this trend is observed in each one of the five different plating baths. For instance, consider plating from the 10:1 bath with k = 0.0048 cm/s. Deposition using a current density of -20 mA/cm^2 results in an average composition of 71 mol% iron whereas deposition at -100 mA/cm^2 results in a film with an average iron composition of 24 mol%. The applied current density also has a direct effect on the flow sensitivity of alloy composition. In general, the sensitivity of deposit composition to electrolyte flow increases as the current density is reduced. While the flow-induced range in composition is roughly 53 mol% when plating at -20 mA/cm^2 from the 10:1 bath (i.e. 80 mol% iron at k = 0.0072 cm/s vs. 27 mol% at k = 0.0012 cm/s), the composition range is only 30 mol% when plating at -100 mA/cm^2 using the same mixing conditions. This general characteristic is observed in all the plating bath formulations except the 5:1 bath, which seems to exhibit significant flow sensitivity at all current densities.

The plating current efficiencies of the five different baths are relatively high, with higher current densities leading to higher efficiencies, as is commonly observed [12, 47]. Figure 2.3 summarizes the effects of bath agitation, current density and dissolved metals ratio on the measured plating efficiency of NiFe deposition from the sulfamate/chloride bath. In general, the plating efficiency varies from 0.60 to 0.95 for the conditions investigated here. Between the different baths the efficiencies were quite similar for films plated under identical conditions. For example, the plating efficiency is 0.77 for deposition at -20 mA/cm^2 and k = 0.0036 cm/s using both the 5:1 and 25:1 baths. Plating at -100 mA/cm^2 results in efficiencies consistently above 0.90, regardless of the bath used. Within any given bath, the efficiency increases with increased current density and
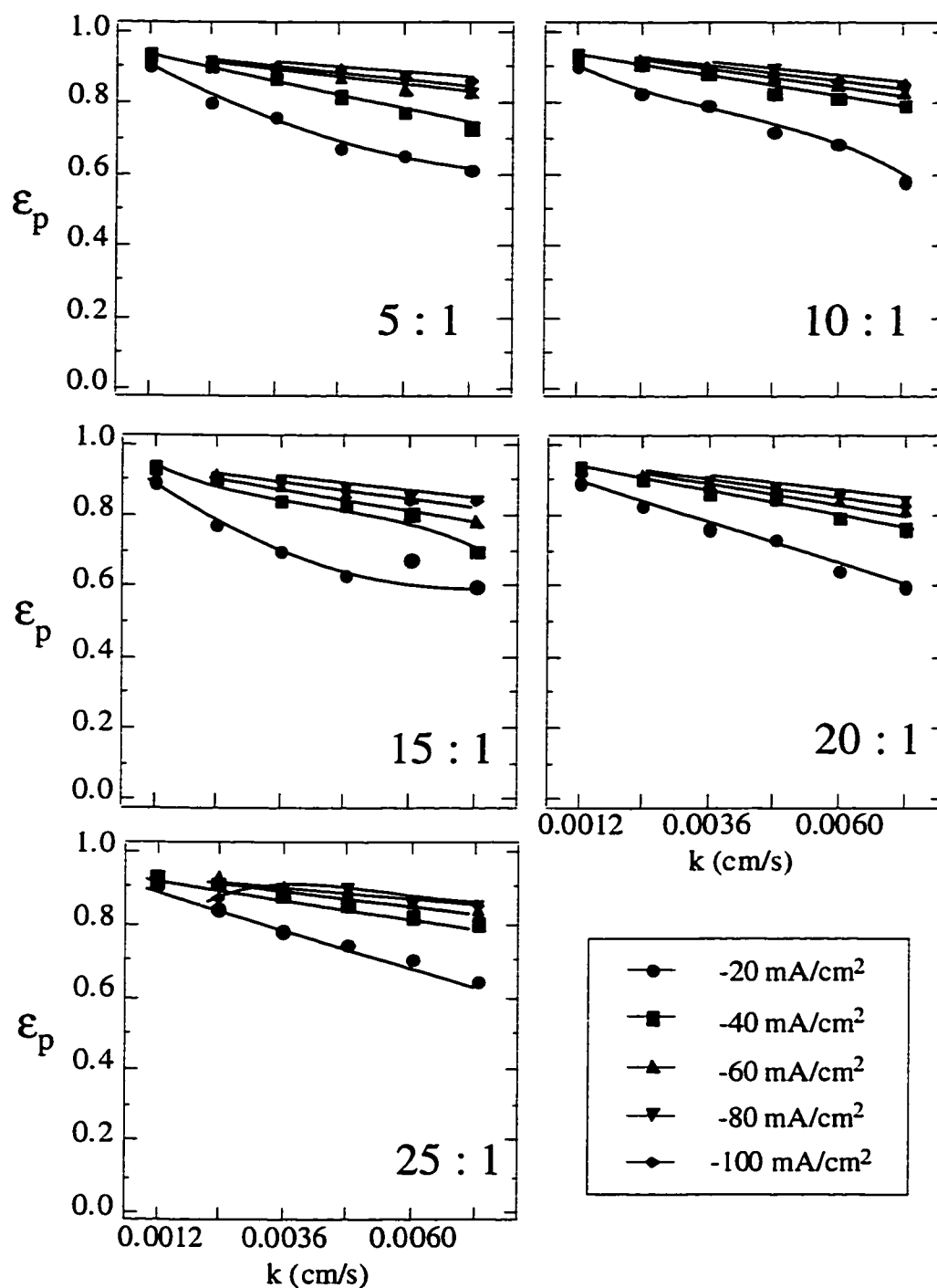
Figure 2.3. The effect of current density and electrolyte agitation on plating efficiency for the family of sulfamate/chloride electrolytes. The dissolved $Ni^{+2}:Fe^{+2}$ molar concentration ratio in the five baths varies from 5:1 to 25:1 as indicated.

decreases with increased bath agitation, consistent with mass transfer limited hydrogen evolution. The combination of high current densities and plating efficiencies results in relatively fast deposit growth. For the range of conditions investigated here, the film growth rates varied between 17 and 110 µm/hr. In general, the deposits were bright and reflective and adhered well to the platinum substrate. In addition, under no plating conditions were the deposits observed to peel or crack as a result of internal stress.

Even though the plating bath chemistries differ, the metallurgical characteristics of deposits made in this study are quite similar to those made by Grimmett *et al.*. Figure 2.4 shows a series of XRD patterns from alloys plated at -20 mA/cm^2 over a wide range of compositions. At low iron compositions, the alloy exhibits a (111) growth orientation with a significant (200) reflection as well. The intensity of the (200) peak decreases with increasing iron composition and disappears entirely between 55 and 60 mol% iron, the transition between the fcc and bcc crystal lattice. Above 60 mol% iron, the deposit is completely bcc with a (110) texture. The phase transition starting at 50 mol% iron is consistent with the results of Grimmett *et al.* for dc plating under similar hydrodynamic and polarization conditions [13].

Another indication of the structural similarities between the alloys plated here and those made by others is the measured lattice parameter. The lattice parameters of the alloys plated here are nearly identical to those determined by Grimmett *et al.* for dc plated films. Figure 2.5 shows the relationship between the lattice spacing and the composition of alloys plated at -20 mA/cm^2. For deposits with compositions less than 55 mol% iron, a steady increase in the fcc lattice parameter is evident as the iron composition increases. After the fcc/bcc phase transition, the lattice parameter decreases significantly (due to the close packed nature of the bcc lattice), but increases with iron composition (except for the outlier at 70 mol% iron). These trends and calculated values for the lattice parameter for both the fcc and bcc crystal lattice are nearly identical to those determined by Grimmett *et al.* as well as for thermally prepared NiFe alloys of similar composition [13].

The results shown in Figs. 2.2 and 2.3 illustrate the versatility of plating with the sulfamate/chloride bath. For plating applications in which high sensitivity to mixing and/or current density is desirable, a number of different bath formulations can be used.
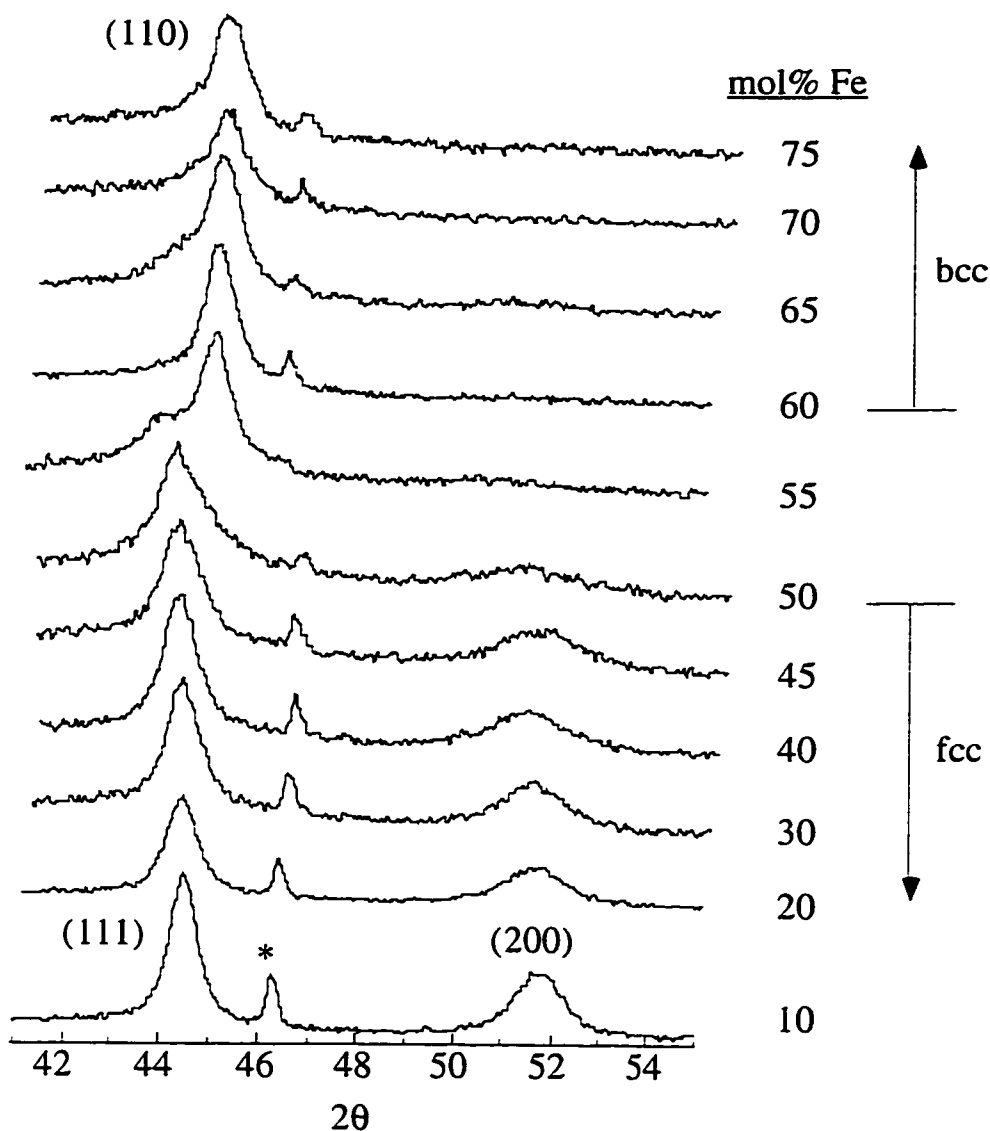
Figure 2.4. X-ray diffraction patterns for a number of NiFe films plated at -20 mA/cm². For deposits with iron content less than 50 mol%, the crystal structure is fcc and exhibits a (111) orientation with a strong (200) reflection. For iron compositions greater than 60 mol%, the alloy is bcc with a (110) growth texture. A mixed fcc/bcc phase exists for 50 < mol% iron < 60. Reflections from the platinum substrate are labeled (*).

As an example, consider the deposition of pulse plated or flow-induced NiFe composition modulated alloys (CMAs). Deposition of these alloys requires a bath in which the deposit composition is fairly sensitive to polarization and/or mixing conditions.
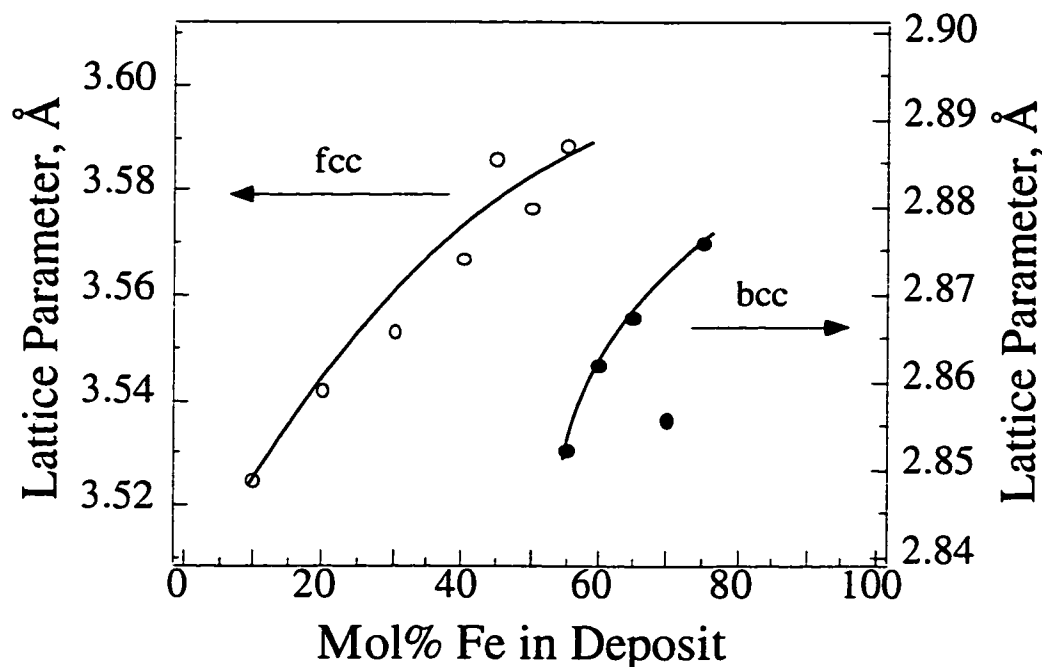
Figure 2.5. Relationship between lattice parameter and alloy composition for NiFe films plated at -20 mA/cm². The lattice parameter increases with increasing iron composition for both the fcc (o) and bcc (●) crystal lattice.

Depending on the extent of composition variation desired in the alloy, an appropriate plating bath recipe can be determined based on Fig. 2.2. For example, in Chapter 5 we show that flow-induced NiFe CMAs with moderate composition variations (*i.e.* in excess of 30 mol%) can be plated and characterized using the 20:1 bath recipe presented here. Based on Fig. 2.2, it appears that deposition (either pulsed or flow-induced) of NiFe CMAs with an even greater composition variation than 30 mol% is possible using the 10:1 bath recipe. In fact, it appears that one could deposit NiFe CMAs from this bath using either pulsed or flow-induced techniques in which the composition would vary between 27 and 80 mol% iron.

In many applications, however, it is undesirable to plate NiFe with such extreme compositional sensitivity to flow and current distribution. In the fabrication of NiFe microstructures by deposition through patterned molds, for instance, the desired alloy composition is often quite specific, such as Permalloy or Invar [5-8, 36]. In general, plating uniform NiFe microstructures is challenging due to unavoidable and significant

variations in current density and electrolyte mixing across the patterned cathode [15-18]. While the extent of current variations and mixing non-uniformities can often be minimized, these non-uniformities nearly always exist. Given the sensitivity of NiFe deposit composition to electrolyte mixing and current density, the engineering challenge becomes one of developing plating baths in which deposit composition is relatively insensitive to polarization and mass transfer conditions. Of the baths discussed here, it is clear that the formulations with less dissolved iron (*i.e.* 20:1 and 25:1) are the most promising for this type of application, although these baths are less flow and polarization sensitive only at higher current densities (-60, -80 and -100 mA/cm^2) and over a narrow range of deposit compositions.

For applications in which current density and electrolyte mixing are well controlled (or at least understood to some extent), specific operating conditions and plating bath recipes for deposition of Permalloy and Invar are summarized in Figure 2.6. In Fig. 2.6 (A), specific current density and electrolyte mixing conditions for plating Permalloy from the 10:1, 15:1, 20:1 and 25:1 baths are reported. A number of processing conditions can be used to plate Permalloy, and depending on the polarization and mixing conditions present in the plating apparatus, one set of conditions may be preferable to another. The 15:1 bath is the most robust of the four presented; Permalloy can be plated from this bath over a wide range of current densities and mixing conditions. The highest Permalloy plating rates are achieved using this bath. Deposition at -160 mA/cm^2, for example, results in a deposition rate of nearly 160 μm/hr. In through-mold plating of microstructures, however, exact control of current density and mass transfer in high aspect ratio features is often not possible. Thus, to plate Permalloy microstructures, the 25:1 bath would likely be the best choice given its relative insensitivity to variations in current density and electrolyte mixing conditions. This bath is capable of high rate plating as well, with a maximum deposit growth rate of approximately 120 μm/hr achieved using a current density of -120 mA/cm^2. High plating rates may be desirable when plating microstructures of significant thickness such as 500 or 1000 μm.

Figure 2.6 (B) illustrates the different baths and plating conditions that can be used to deposit Invar. Of the five plating baths developed for this study, three can be used to plate Invar, but only the 5:1 bath offers flexibility in applied current density and
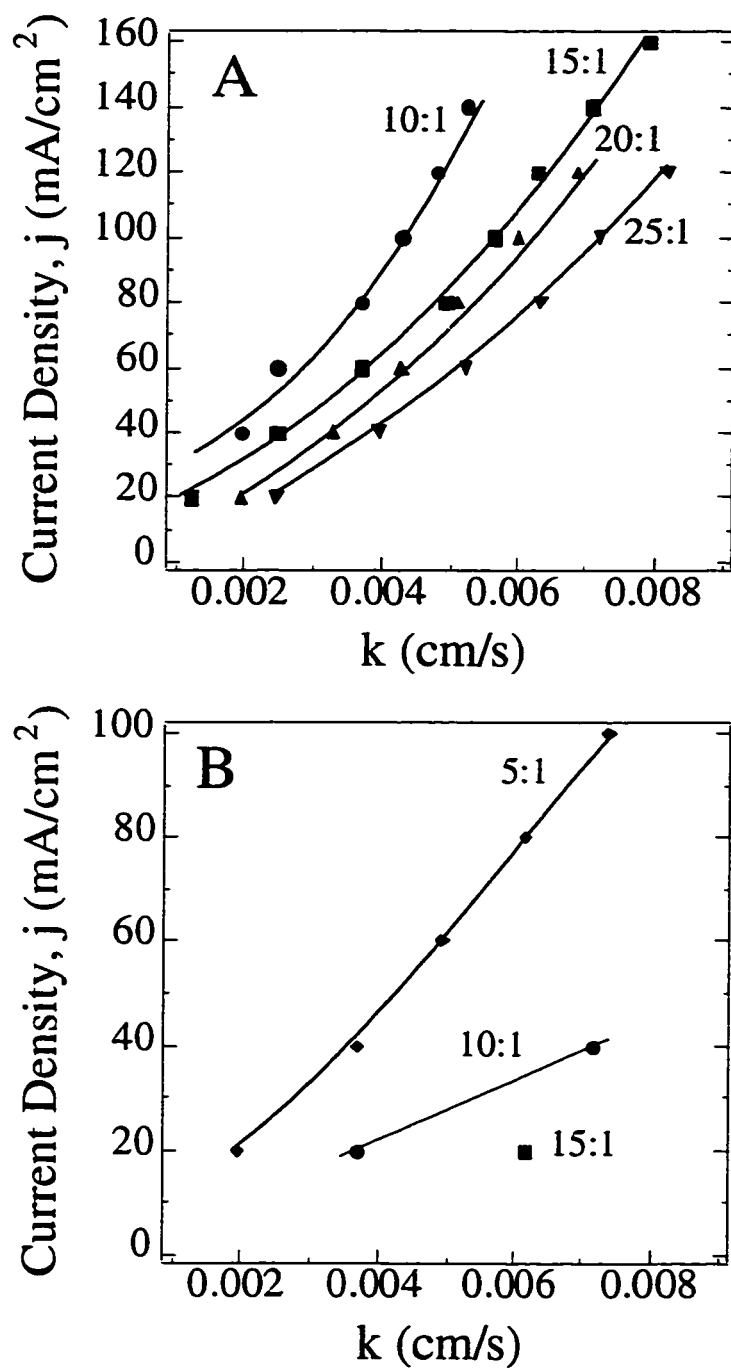
Figure 2.6. (A) Electrolyte agitation and polarization conditions for deposition of Permalloy from the 10:1 (●), 15:1 (■), 20:1 (▲) and 25:1 (▼) plating baths. (B) Electrolyte agitation and polarization conditions for deposition of Invar from the 5:1 (◆), 10:1 (●) and 15:1 (■) plating baths.

mixing rates. This bath can be used to plate Invar at rates between 20 and 108 μm/hr over a range of mass transfer conditions from k = 0.0012 to 0.0072 cm/s. The specific conditions used to plate Invar from this type of bath should be determined by the performance specifications of the deposit. For example, the grain size (and, thus, the magnetic and mechanical properties) of electrodeposited materials is in part dependent on the current density used during plating [48]. For any given application, therefore, the deposition conditions used to plate Invar from this bath should be chosen such that structural characteristics such as grain size are optimized so that the desired material properties are obtained.

Conclusions

In this chapter, we have expanded on previous work to develop a nickel sulfamate/iron chloride plating bath. Using a systematic experimental approach, we have characterized the performance of a NiFe plating bath that is both versatile and robust. The plating bath characterization provides specific recipes and operating guidelines for deposition of alloys with a wide range of compositions. Specific conditions for depositing two industrially important alloys, Permalloy and Invar, at a variety of growth rates are reported. Results of the study are presented in a general form that can easily be applied to plating NiFe alloys in any other plating apparatus with well understood current distribution and electrolyte mixing characteristics. It is our goal that the well defined relationships between applied current density, electrolyte mixing and deposit composition detailed in this study can be used by others to tailor a wide range of NiFe alloy compositions to meet specific needs. In subsequent chapters we apply the results of this bath characterization study in two ways : (1) Understanding and optimization of through-mold electrodeposition of compositionally uniform NiFe microstructures (discussed in Chapters 3 and 4) and (2) Plating of thin film and microstructure NiFe CMAs (discussed in Chapters 5 and 6).

CHAPTER 3

Through-Mold Electrodeposition using the Uniform Injection Cell (UIC) : Workpiece and Pattern Scale Uniformity

Summary

In this chapter, we report on the operation of an electroplating device based on the uniform injection cell (UIC) concept. Workpiece scale mass transfer characteristics are explored using limiting current measurements and are related to theoretical predictions. Results show that the device delivers predictable and controlled average mass transfer rates at the workpiece length scale. Pattern scale uniformity is explored by electrodeposition of NiFe microgears onto a patterned substrate. Statistical analysis of compositional differences between an electroplated NiFe film and electrodeposited NiFe microgears is used to explore mass transfer on the pattern scale. Results illustrate that the presence of a patterned mold influences the average mass transfer rate compared to the unpatterned electrode, but does not create additional variability in electrolyte mixing across the substrate. Implications for using the device in through-mold plating are discussed and future improvements to the device are suggested.

Background

Many high technology applications rely on electrodeposition of metals and alloys through patterned insulating molds ranging in thickness from a few to a few hundred microns [4, 26]. Features defined by the mold can be as small as 2 μm wide and often exhibit very high aspect ratios (e.g. > 10:1) [3, 49-51]. Plating microstructures requires consideration of current distribution and mass transfer characteristics on multiple length scales [4, 20]. Significant non-uniformities in current distribution and mass transfer can arise on length scales associated with the workpiece (order of cm), the masked pattern (order of mm) and individual structural features (order of μm) [14-20]. Depending on the performance requirements of the particular electrodeposited structure, uniformity of mass transfer and/or current distribution may be required at each length scale. Thus, a long-standing engineering challenge of through-mold electrodeposition is understanding and establishing uniformity of current and mass transfer on each length scale of interest.

Prior to considering the complexities involved in pattern and feature scale non-uniformities, the current distribution and mass transfer characteristics at the workpiece scale must first be resolved. Development of an electroplating device that delivers uniformity of current and mass transfer over the entire workpiece is the first step in this direction. The uniform injection cell (UIC) is a recently developed electrochemical cell that, in theory, exhibits many desirable traits including a uniform primary current distribution for all operating conditions, simple analytic expressions for predicting cell performance and easy scale-up and fabrication of a working device. Previous studies with this device have focused on theoretical and experimental characterization, but the application of the UIC for through-mold plating has not been explored [46, 52-54]. In this work, we report on the design of a plating device based on the UIC and explore issues affecting workpiece and pattern scale uniformity of current and mass transfer in through-mold plating of NiFe microstructures.

The design and fabrication of the device is based on previous theoretical work and considerations in scale-up for manufacturing applications. Mass transfer characteristics are investigated using limiting current measurements and results are compared to theoretical predictions. The device is used to plate thin NiFe films onto a copper coated silicon substrate from a well characterized plating electrolyte. The average composition of dissolved films is determined using uv-vis spectrophotometry and local variation in composition is explored with energy dispersive x-ray spectroscopy (EDS). These results are used to assess workpiece scale uniformity of mass transfer in the device. The utility of the UIC for through-mold electrodeposition is demonstrated by fabrication of 3-D microstructures. NiFe microgears are electrodeposited in plastic molds defined by x-ray lithography. Pattern scale composition uniformity of plated parts is studied using scanning electron microscopy (SEM) and EDS analysis. Statistical analysis of compositional differences between an electroplated NiFe thin film and electrodeposited NiFe microgears is used to explore mass transfer on the pattern scale.

Experimental

UIC Design and Operation

A conceptual illustration of the device is shown in Fig. 3.1. The device essentially consists of two parallel, coaxial disks with a narrow gap, L, between them [46, 54]. The upper disk is a porous frit of radius R mounted in an insulating tube. The lower

Counter Electrode
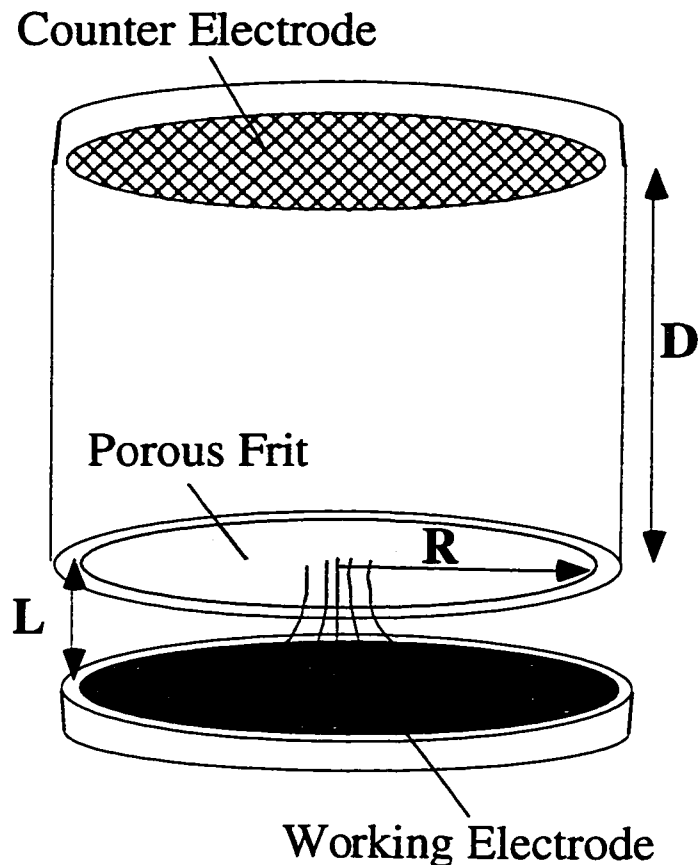
Figure 3.1. Conceptual illustration of the UIC device showing critical dimensions and the radial electrolyte flow pattern near the working electrode. The gap, L, is exaggerated in this schematic; in reality the porous frit and the working electrode are parallel and L/2R << 1.

disk, also of radius R and coaxial with the frit, is the working electrode. During operation, electrolyte is injected through the frit with a (nominally) uniform velocity V into the gap and onto the working electrode. In theory, operation of the device with small aspect ratio (*i.e.* L/2R << 1) and perfectly uniform injection results in a self-similar radial flow which ensures a spatially uniform hydrodynamic and concentration boundary layer over the working electrode [46, 54].

The device is shown schematically in Fig. 3.2 and consists of an adjustable assembly of insulating pipe constructed to direct electrolyte flow through the porous frit and onto the fixed working electrode. The shell of the device (A), is constructed from a
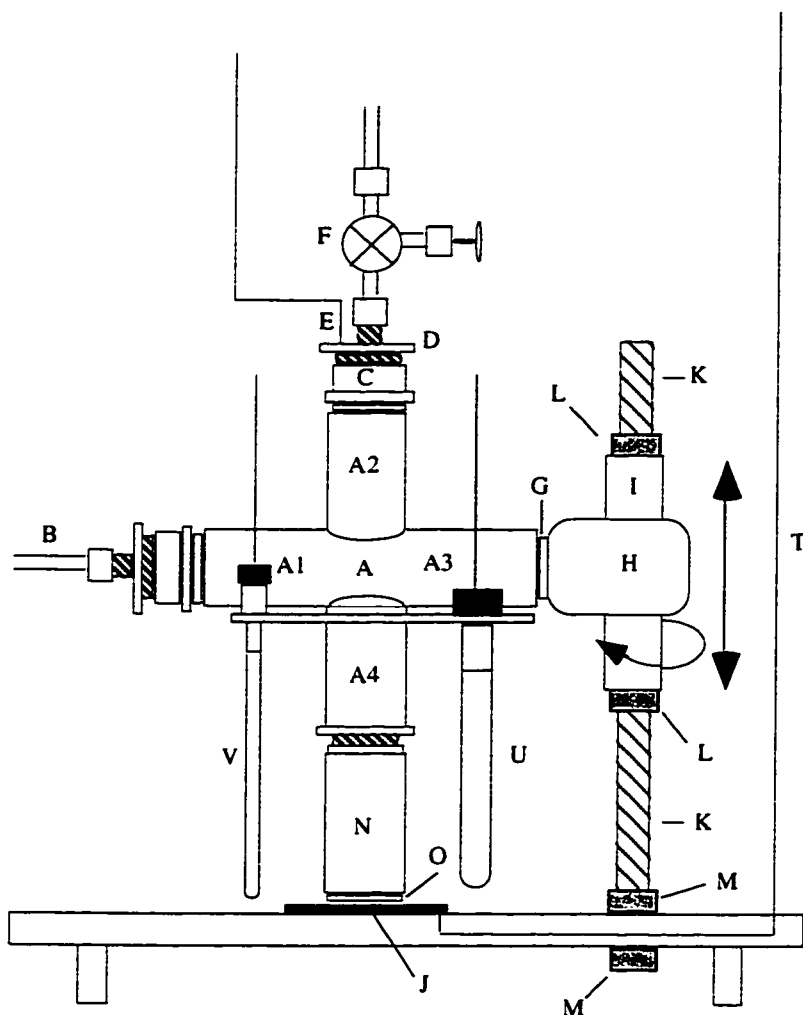
Figure 3.2. Schematic of the UIC device. The porous frit is located at O and the working electrode is labeled J. Directions of possible device positioning are indicated by the solid arrows.

42 mm OD polyvinylchloride (PVC) cross fitting with four arms, labeled in the figure A1, A2, A3 and A4. The inlet channel for electrolyte flow (A1) is connected via PVC fittings to Teflon tubing which serves as the inlet source for electrolyte to the device (B).

The shell section (A2) houses the counter electrode and a counter electrode gas vent. At the end of (A2) is a PVC fitting (C), the interior of which is modified to accommodate a porous glass shelf for placing sacrificial metal anode material during

electroplating. The shelf itself is a sintered glass disk approximately 25 mm in diameter and 3 mm thick with an average pore size of 150 μm. Above the glass shelf is a high area platinum mesh counter electrode which is used to make contact with the sacrificial anode material during operation. The counter electrode exits the device through the cap (D) via a hole approximately 100 μm in diameter. Silicone is used to seal the platinum wire exit point (E). The PVC cap (D) is tapped and threaded for attachment of Teflon tubing that connects directly to an in-line Teflon needle valve (F) used to relieve gas generated at the counter electrode. Gas is vented via the needle valve (F) through Teflon tubing. Any electrolyte that escapes the valve is recycled to the plating bath.

The device positioning arm is labeled (A3). This part of the device is used solely for positioning the porous injector relative to the working electrode and, thus, is made inaccessible to electrolyte flow via a PVC plug (G). The plug is bonded to (A3) at one end and to a PVC cap fitting (H) at the other. A vertical hole is drilled through the cap (H) and a Plexiglas sleeve (I) is fit through the hole and glued in place. The entire device is raised, lowered and rotated relative to the working electrode (J) by sliding the Plexiglas sleeve over a stainless steel, all-thread rod (K). Directions of possible device positioning are indicated by solid arrows in Fig. 3.2. The device is immobilized on the rod by tightening stainless steel nuts (L) above and below the sleeve. The threaded rod is held in place by two stainless steel nuts (M) clamped around a clear Plexiglas plate which serves as the base stand for the UIC device.

The electrolyte injection arm is labeled (A4). Bonded to one end of A4 is a fitting which serves to connect and disconnect the device shell (A) from a removable porous frit injector housing (N), shown in greater detail in Fig. 3.3. At the other end of the housing (N) is a modified PVC fitting (O) which is machined to create a thin, flat lip (P) approximately 1 mm wide at the base (see Fig. 3.3 (B)). The lip serves as a backing to which a 3 mm thick, 25 mm diameter sintered glass disk (Q) is glued. The average pore size of the sintered glass disk is between 25 and 50 μm. The glass disk serves as the porous frit through which electrolyte is injected into the gap. The frit injector housing was made removable so that a variety of porous frits could be used. Operation of the device with glass frit injectors of different porosity were studied, but the 25-50 μm frit allowed the largest range of injection velocities to be investigated. For this reason, the 25-50 μm frit was used exclusively in this study.

A   B

N

O

Side View   Axial View
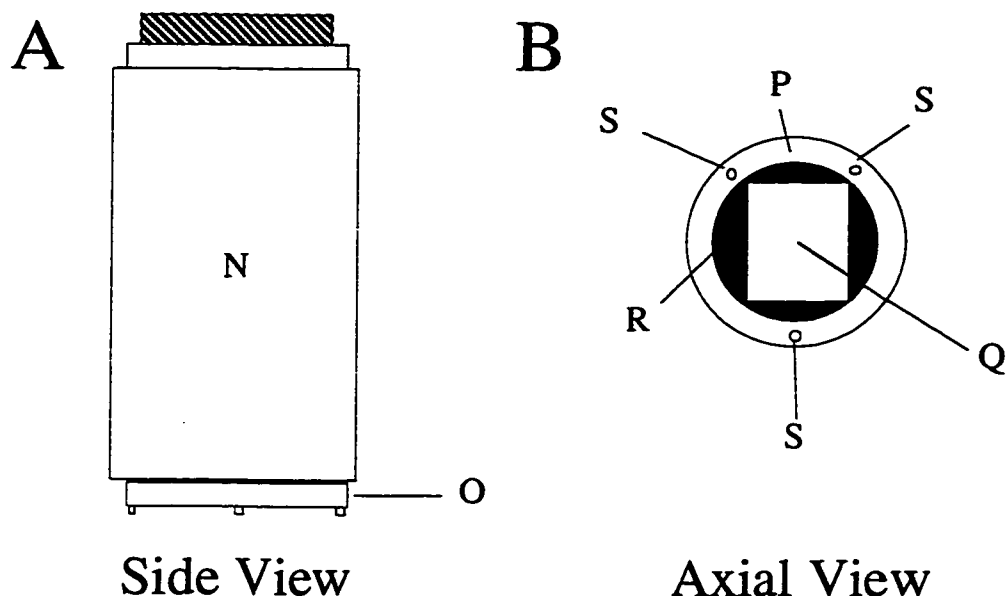
Figure 3.3. The removable porous frit injector housing in side (A) and axial (B) view.

A slight modification to the circular injector was made due to the geometry of the plastic mold used during plating of microgears. A rectangle 0.9 cm wide and 1.4 cm long was cut from a thin sheet (500 μm) of plastic (R) which was glued to the glass frit before mounting, effectively changing the flow channel. The rectangular flow area removes the axial symmetry of the flow field and may affect the mass transfer characteristics of the device, as will be discussed later. Three stainless steel set screws 1.5 mm in length (S) are mounted on the lip of the injector housing to provide accurate spacing between the injector and the working electrode. We estimate that the gap spacing can be set using a digital micrometer with an accuracy of +/- 50 μm using this technique. Contact between the working electrode and the power supply is made with 100 μm diameter insulated platinum wire (T). A Plexiglas plate with a centered hole is slid over and glued onto the injector arm (A4). Two holes are drilled through the plate so that necessary auxiliary electrodes such as a reference electrode (U) and pH probe (V) can be placed very near the working electrode during operation.

The general operation of the plating device is illustrated schematically in Fig. 3.4. Here the device is shown sitting in an open-topped Plexiglas box containing the plating electrolyte. The electrolyte is recirculated from the box to the device inlet via a digitally controlled Ismatic Model 07617-70 positive displacement pump through Teflon tubing. Prior to all experiments with the UIC device, a pump calibration curve was determined using room temperature distilled water. Dashed arrows in Fig. 3.4 indicate the electrolyte flow direction during operation. After leaving the pump, the electrolyte is passed through a 20 μm Whatman Polycap 75 HD filter capsule before entering the device. With the gas relief valve closed, electrolyte is injected from the device, into the gap and onto the working electrode. Polarization is controlled by an EG&G Princeton Applied Research (PAR) Model 173 Potentiostat. During deposition, the gas relief valve is opened slightly to release gas generated at the counter electrode. Compared to the flow through the porous frit injector, a negligible volume of electrolyte passes through the gas relief valve.

Limiting Current Measurements

The Fe^{+2}/Fe^{+3} redox couple was used to characterize steady state mass transfer in the plating device. A well supported, room temperature (~23°C) electrolyte composed of 20 mM Fe^{+2} and 40 mM Fe^{+3} (from sulfate salts) and 1.0 M H_2SO_4 was used in all limiting current experiments. The kinematic viscosity of the electrolyte and diffusivity of Fe^{+2} were estimated to be 0.011 cm^2/s and 4.75 x 10^{-6} cm^2/s based on earlier studies [46, 54]. No ohmic compensation was used, but earlier studies suggest that proper placement of the reference electrode (*i.e.* very near the edge of the disk) effectively eliminates ohmic contributions [46, 54]. A high area platinum mesh counter electrode was used during all limiting current measurements. A rectangular platinum foil working electrode with an area of 1.5 cm^2 was mounted with insulating plating tape on the Plexiglas base. The dimensions of the working electrode were chosen such that the rectangular porous frit injector could be positioned directly over the electroactive area. The working electrode was then cleaned using acetone, methanol and distilled water. Using the injector set screws, the gap, L, was set to 500 μm. After placing the UIC device in the electrolyte bath, the working electrode was further cleaned by cyclic potential scanning from -450 to 1800 mV vs. SCE at 100 mV/s for 30 minutes.

The experimental procedure consisted of measuring the mass-transfer limited current for different injection velocities, V, for a single gap spacing of 500 μm. The
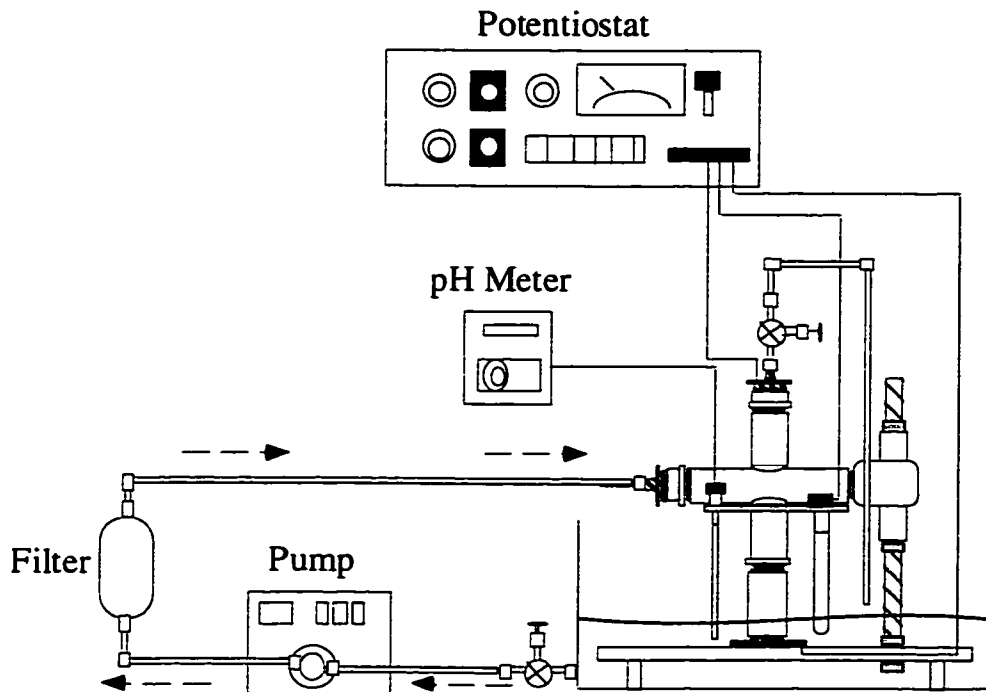
Figure 3.4. Schematic representation of the complete plating apparatus including UIC, digital pump, microfilter, pH meter and power supply. Dashed arrows indicate direction of electrolyte flow during operation.

working electrode was held at 1450 mV vs. SCE, a potential in the mass transfer limited plateau for oxidation of Fe^{+2}, yet still cathodic of oxygen evolution in this electrolyte. After waiting 15 seconds for the system to reach steady state, the limiting current was recorded and the injection velocity was then changed. Experiments were performed for volumetric flow rates ranging from 0.2 to 41.4 cm^3/s, corresponding to average injection velocities ranging from 0.13 to 27.6 cm/s.

NiFe Thin Film Electrodeposition

NiFe films were galvanostatically electrodeposited at room temperature from a well characterized nickel sulfamate/iron chloride plating electrolyte. The bath was composed of nickel and iron salts, boric acid, sodium saccharin, sodium dodecyl sulfate and ascorbic acid. Two slightly different baths were used in this study, one in which the dissolved Ni:Fe molar ratio was 10:1 and another in which Ni:Fe was 25:1. The exact composition of each plating bath is detailed in Chapter 2. Prior to plating, the copper

surface of the working electrode was cleaned by immersion in 5% H_2SO_4 for 60 seconds followed by a distilled water rinse. During deposition, the pH of the plating bath was continuously monitored and adjusted to 3.00 +/- 0.05 by addition of NaOH.

Two different traits of electrodeposited NiFe were explored : (1) The average composition of 20 μm thick films plated from the 10:1 bath and (2) Local composition variation in 5 μm thick films plated from the 25:1 bath. NiFe films were plated from the 10:1 bath onto a copper coated silicon substrate to a thickness of approximately 20 μm using current densities of -30, -40 and -60 mA/cm², corresponding to growth rates of approximately 32, 45 and 65 μm/hr. Six different convective-diffusive mass transfer conditions were investigated, representative of the entire range of injection velocities delivered by the pump. The average composition of each 20 μm thick film plated from the 10:1 bath was determined using a UV-vis spectrophotometric technique.

After deposition, the wafer was weighed using an Ainsworth AA-200D electronic analytical balance. The NiFe films were then dissolved in a solution containing 5 ml concentrated H_3NO_3 and 2 ml of 30% H_2O_2. The substrate was weighed again and the mass of the deposit was calculated from the difference in substrate mass before and after dissolution of the film. After dissolution of each film the total mass of NiFe in solution was recorded and the solution was diluted to approximately 500 ppm by addition of distilled water. A small volume of this diluted solution (5 ml) was then combined with 5 ml of 3 M KSCN, 1 ml of 30% H_2O_2 and 89 ml distilled water. Upon vigorous mixing, the dissolved iron is completely oxidized to Fe^{+3}, with which the -SCN group forms a bright red complex. The intensity of the red solution is directly proportional to the complexed iron concentration. The optical absorbance of each solution relative to a deionized water standard was then measured at 480 nm using a Cecil CE 1011 spectrophotometer. To determine the mass of iron in each solution, an absorbance vs. iron composition calibration curve was constructed using solutions containing dissolved iron powder of known concentrations. The average composition of each film was then calculated by dividing the measured mass of iron in solution by the total mass of NiFe determined gravimetrically.

NiFe films were plated from the 25:1 bath onto a copper coated silicon substrate to a thickness of approximately 5 μm at -90 mA/cm² using an injection velocity of 22

cm/s. Local variations in composition of the 5 μm thick films were investigated using a JEOL JSM-5200 scanning electron microscope (SEM) with QX 2000 energy dispersive x-ray spectroscopy (EDS) instrumentation and software developed by Link Analytical Ltd. Quantification of EDS spectra from areas of the film measuring 1 x 1 mm^2 was accomplished using relative peak intensities from the Ni K$_\alpha$ line of the NiFe film and a polished nickel standard, taking into account ZAF corrections for matrix interactions within the NiFe deposit [55].

Through-Mold Electrodeposition of NiFe Microgears

NiFe microgears 1200 μm in diameter and 220 μm thick were electrodeposited onto a copper coated silicon substrate through a polymethylmethacrylate (PMMA) mold defined by x-ray lithography (*i.e.* the LIGA process [51, 56]). The gears were plated at room temperature (~23° C) from the 25:1 plating bath. During deposition, the bath pH was continuously monitored and adjusted to 3.00 +/- 0.05 by addition of NaOH.

The patterned working electrode was mounted on the Plexiglas base of the UIC using insulated plating tape. An electroactive area measuring 1.1 x 1.6 cm and containing approximately 85 individual microgear parts was defined using plating tape. The frit was then positioned directly over and centered on the electroactive area. The gap, L, was adjusted to 500 μm using the set screws on the porous frit injector housing. Immediately prior to plating, the copper surface of the patterned working electrode was cleaned by immersion in 5% H$_2$SO$_4$ for 60 seconds followed by a distilled water rinse.

Microgears were electrodeposited using a current density of -60 mA/cm^2 (a rate of approximately 65 μm/hr) and an average electrolyte injection velocity of 23 cm/s. Plating the gears to a thickness of 220 μm required 5.5 hours due to overplating at the insulating edges of the plastic mold. After plating, the microgears were planarized to a thickness of approximately 200 μm while still confined within the PMMA mold using 15, 6 and 1 μm Engis 1313-T4 oil-based lapping slurries. Further polishing of microgear parts was accomplished using 1 μm Metadi II diamond paste from Buehler. The PMMA was then dissolved from the substrate by immersion in methylene chloride for approximately 30 minutes. Structural and compositional features of the plated microgears were investigated using SEM and EDS. Quantitative EDS composition maps of individual microgears were constructed using relative peak intensities from the Ni K$_\alpha$

line of the NiFe gear and a polished nickel standard, taking into account ZAF corrections for matrix interactions within each NiFe sample [55].

Results and Discussion

Convective-diffusive mass transfer characteristics for the plating device are presented in terms of dimensionless parameters Sh, Sc and Re. The Sherwood number, Sh, is directly proportional to the limiting current density, j_l, through the relationship Sh = j_lL/nFD_ic_i, in which L is the injector gap, D_i is the mass diffusivity of reacting species i, c_i is the concentration of species i, n is the number of electrons transferred and F is Faraday's constant. The influence of electrolyte properties and the strength of electrolyte flow on limiting current behavior are characterized by the Schmidt number, Sc = v/D, and the Reynolds number, Re = VL/v, respectively, where v is the kinematic viscosity. In theory, the mass transfer characteristics in the UIC follow two distinct relationships with the electrolyte injection rate [46, 54]. For low Reynolds flows (Re<3) the mass transfer characteristics are described by the relationship

$$Sh/Sc^{1/3} = 1.12Re^{1/3} \qquad (3.1)$$

while at higher injection velocities (Re>10) mass transfer is described by

$$Sh/Sc^{1/3} = 0.85Re^{1/2}. \qquad (3.2)$$

Plotted in Fig. 3.5 is a single log-log curve of $Sh/Sc^{1/3}$ vs. Re which summarizes the limiting current measurements for the device using an injector gap L = 500 μm. The symbols are data points from the limiting current measurements and the solid lines represent the expected relationship predicted by Eqs. (3.1) and (3.2) for low and high Reynolds flows using an electrolyte with D = 4.75 x 10^{-6} cm²/s and v = 0.011 cm²/s. The experimental results compare well with theory over the entire range of electrolyte injection velocities. For low injection velocities, the best-fit slope of $Sh/Sc^{1/3}$ vs. Re is 0.36 for the experimental data, which is in close agreement with the value of 1/3 predicted by Eq. (3.1). For high Re flows (Re > 10), the experimental measurements are also close to theory, with the $Sh/Sc^{1/3}$ vs. Re best-fit slope of 0.51 nearly identical to the value of 1/2 predicted by Eq. (3.2). In addition, the constants in Eqs. (3.1) and (3.2) are also nearly matched by experiment. For the low Re flows, the experimental constant is
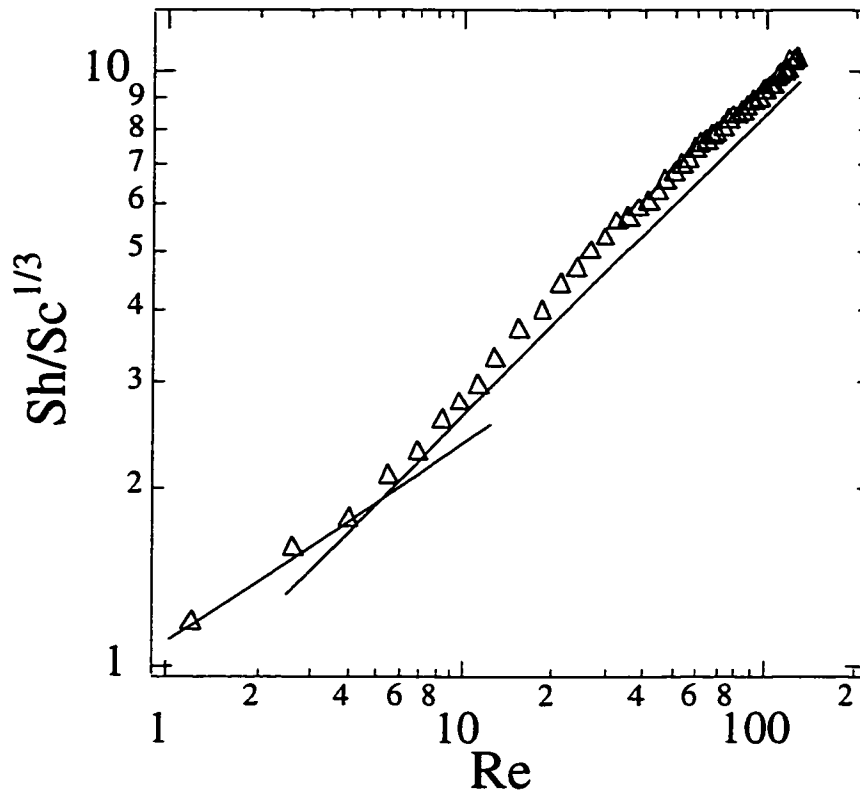
Figure 3.5. Reynolds number dependence of the dimensionless convective mass transfer rate ($Sh/Sc^{1/3}$) in the UIC. The symbols ($\triangle$) are data points from limiting current measurements with a gap setting of $L = 500$ μm and the solid lines represent the expected relationship predicted by Eqs. (3.1) and (3.2).

1.13 and for the high flow regime, the measured constant is 0.92. Both are within 10% of their respective theoretical values. The moderate difference between experiment and theory may be attributable to the gap spacing, L. For a relatively small gap, such as 500 μm used in this study, the experimental measurement of j_l is expected to be sensitive to errors in the gap setting. In Fig. 3.5, for example, the experimental data would have fallen more closely to the best fit lines if the gap was assumed to be $L = 475$ μm instead. A difference of 25 μm is within the experimental error of defining the gap using the set screws on this device.

Since the measured limiting current is an average over the entire working electrode, these results suggest that the workpiece scale mass transfer characteristics of

the device compare well with those predicted for the ideal UIC with perfectly uniform injection and axial symmetry. This is true even with the flow modification to the porous frit injector. While the flow modification does not appear to significantly alter the workpiece scale operation of the device, these results do not ensure uniformity of flow at smaller length scales.

In the limit of infinitesimal aspect ratio (L/2R → 0), the primary current distribution in the UIC is, in theory, spatially uniform [46, 54]. Thus, assuming uniformity of current across the wafer, any variation in mass transfer will affect the deposit composition when electroplating an alloy in which one species deposits under mass transfer control. The well-known fact that the composition of electrodeposited NiFe is highly sensitive to mass transfer conditions [2, 12, 13] makes the plating of NiFe films a good diagnostic for assessing local flow uniformity in the device. Based on this idea, two sets of experiments were conducted, one in which NiFe films were plated onto an unpatterned substrate and another in which NiFe microstructures were deposited through a patterned mold. Identical electrolyte injection velocities and polarization conditions were used in each study. Comparison of average and local deposit compositions between the patterned and unpatterned samples illustrates the effects of the molded pattern on mass transfer.

Shown in Fig. 3.6 are measured relationships between the convective-diffusive mass transfer coefficient, k, the applied current density and the average deposit composition for NiFe films electroplated from the 10:1 bath. Here the mass transfer coefficient is used as a general measure of electrolyte mixing at the electrode surface; it is related to the Sherwood number by the relationship $k = ShD/L$. The measured mole fraction of iron in the deposit, X_{Fe}, increases with enhanced mixing (i.e. with higher k) and decreases with increasing current density, as demonstrated in Chapter 2 and illustrated by others [12, 13, 41].

Investigation of alloy composition on smaller length scales (< 1 mm) shows the presence of compositional non-uniformity. Figure 3.7 is a schematic representation of a 5 μm thick NiFe film plated from the 25:1 bath covering an area of 9 x 14 mm^2 (the porous frit dimensions) on the copper coated substrate. At nine different locations on the film, quantitative EDS analysis of 1 x 1 mm^2 areas illustrates the extent of the local
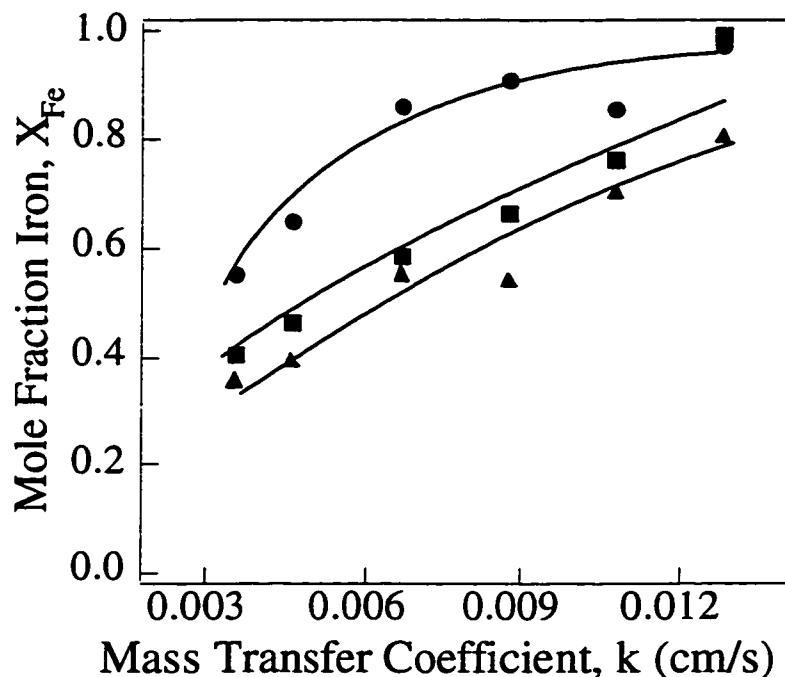
Figure 3.6. Relationship between the convective-diffusive mass transfer coefficient (k) and composition of NiFe thin films plated using the UIC at current densities of -30 (●), -40 (■) and -60 (▲) mA/cm². Solid lines are drawn to guide the eye.

composition variation. The nine locations from which spectra were acquired are labeled A through I in Fig. 3.7.

The average composition of the film represented in Fig. 3.7 is 24 mol% iron, but local composition variations in the film are evident, as illustrated in Table 3.1. The nature of the composition variation does not seem to follow any clear trends, rather it appears that the compositions are more or less randomly distributed. The standard deviation is 7 mol% and seems somewhat high relative to the average composition. As a result, the 95% confidence interval (two-sided) also covers a wide range. These values are biased, however, by the one area with an exceptionally high iron content at location G. In fact, with the exception of location G, the variation in composition across the wafer is moderate. In Table 3.1, values in parentheses represent the wafer statistics for the eight points excluding location G.

9 mm

14 mm

A   B   C

D   E   F

G   H   I
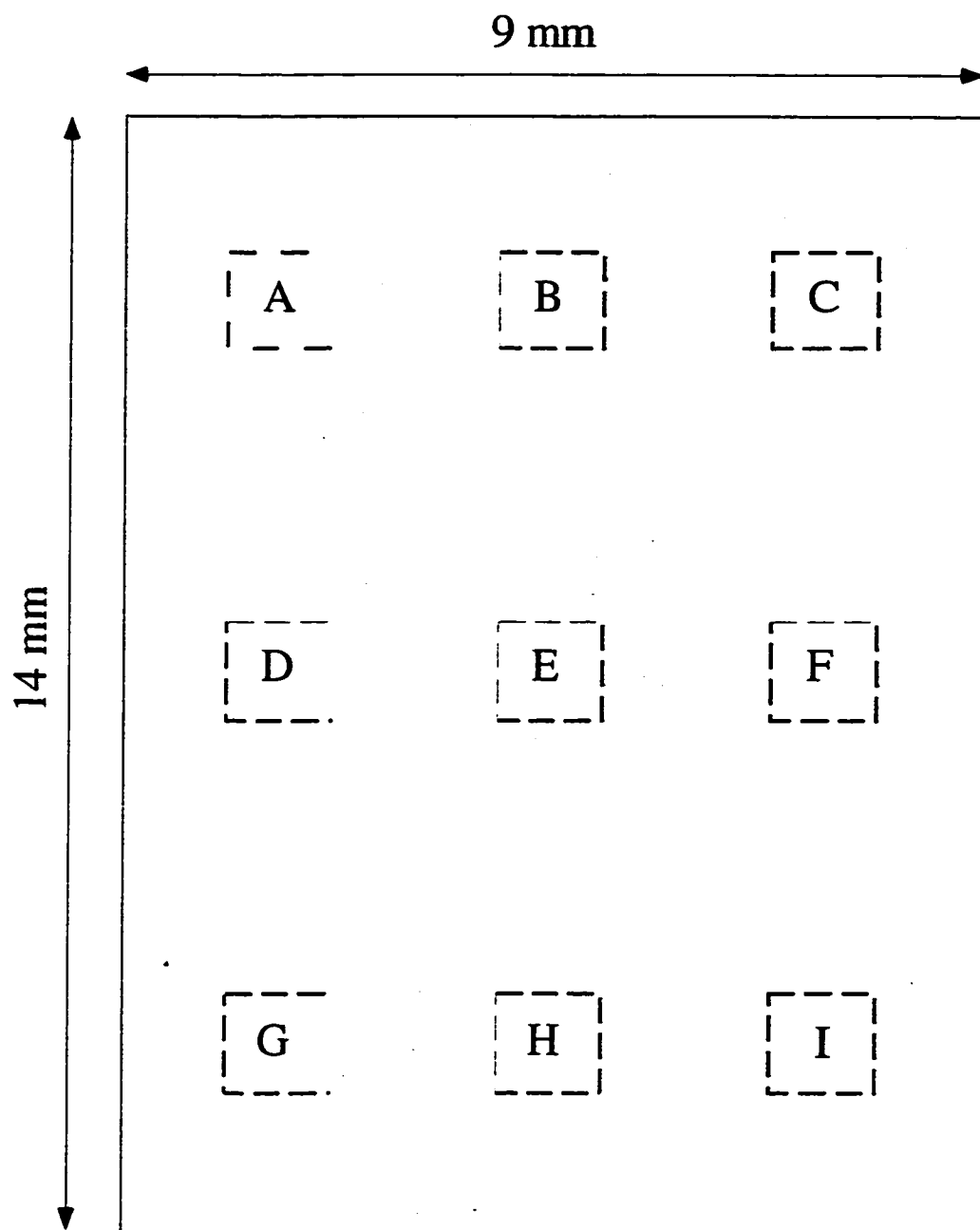
Figure 3.7. Schematic representation of a NiFe film plated from the 25:1 bath covering an area of 9 x 14 mm². Quantitative EDS analysis at nine locations on the actual film labeled A through I illustrate the local composition of areas measuring 1 x 1 mm².

Table 3.1. Composition summary for thin film and microgear deposition at wafer locations A through I. The values in parentheses represent statistics with the exclusion of data from location G.

	Deposit Composition : Mole Fraction Iron, X_{Fe}	
Location on Substrate	Thin Film	Microgear
A	0.24	0.30
B	0.17	0.28
C	0.21	0.34
D	0.23	0.22
E	0.20	0.33
F	0.20	0.29
G	0.42	0.44
H	0.26	0.32
I	0.23	0.26
Average	0.24 (0.22)	0.31 (0.29)
Standard Deviation	0.07 (0.03)	0.06 (0.04)
95% Confidence Interval	+/- 0.05 (0.02)	+/- 0.05 (0.03)

The nature of the compositional variation across the wafer (*i.e.* random) suggests that significant variation in hydraulic permeability may exist within the porous frit. Based on results shown in Fig. 3.6 and our previous work plating NiFe alloys (*c.f.* Chapter 2), we see that areas of relatively high iron content can be caused by either a locally high electrolyte injection rate or a locally suppressed current density (or some combination of the two). Given the characteristics of sintered glass, it is not surprising to observe that the porous frit used in this study performs adequately on average, but appears to exhibit some degree of variation in porosity and hydraulic permeability at small length scales. The area of the frit over location G, for example, may exhibit either a

relatively high permeability (leading to enhanced mass transfer rates) or a relatively low conductivity (leading to decreased current density).

Previous work with the UIC supports this idea of non-uniformity in the frit permeability. In preliminary studies, qualitative experimentation revealed that different frits of the same average porosity exhibited varying degrees of flow uniformity even though the frits were purchased from the same vendor. Despite our efforts to select a frit with good flow uniformity (determined visually), the frit still exhibited imperfect injection characteristics. Thus, while the average performance of the frit is good at the workpiece scale, the sintered glass injector appears to contribute significantly to non-uniformity at smaller length scales.

The presence of a patterned plastic mold on the substrate also influences mass transfer to the exposed substrate. Figure 3.8 (A) is an SEM image of plated microgears after planarization, polishing and removal of the PMMA mold. The gears in this figure were deposited from the 25:1 bath under flow and polarization conditions identical to those used in plating the NiFe film reported in Table 3.1. Figure 3.8 (B) is a quantitative EDS composition map of the microgear highlighted in Fig. 3.8 (A). Here, lighter regions of the gear represent relatively higher iron concentrations. The average composition of the gear is approximately 30 mol% iron. Within the gear itself, the composition is relatively uniform, with slightly lower iron compositions at the tips of the gear teeth. Note that a small micromachined hole 50 μm in diameter appears just to the right of the central gear hub (both the hub and the small hole appear completely white and were not included in determination of the average composition).

The pattern scale effects of plating through an insulated mold are explored by comparison of microgear and thin film compositions. The microgear illustrated in Fig. 3.8 was electrodeposited through the patterned mold at a position on the wafer corresponding to location A in Fig. 3.7. The compositions of eight other microgears plated on the same wafer at positions corresponding to locations B through I in Fig. 3.7 were also determined. Figure 3.9 is a collection of quantitative EDS composition maps of the nine microgears deposited at wafer locations corresponding to those in Fig. 3.7. As in Fig. 3.8 (B), lighter regions in the maps illustrate areas of higher iron concentration. Table 3.1 lists the composition of each microgear deposited at the wafer locations A
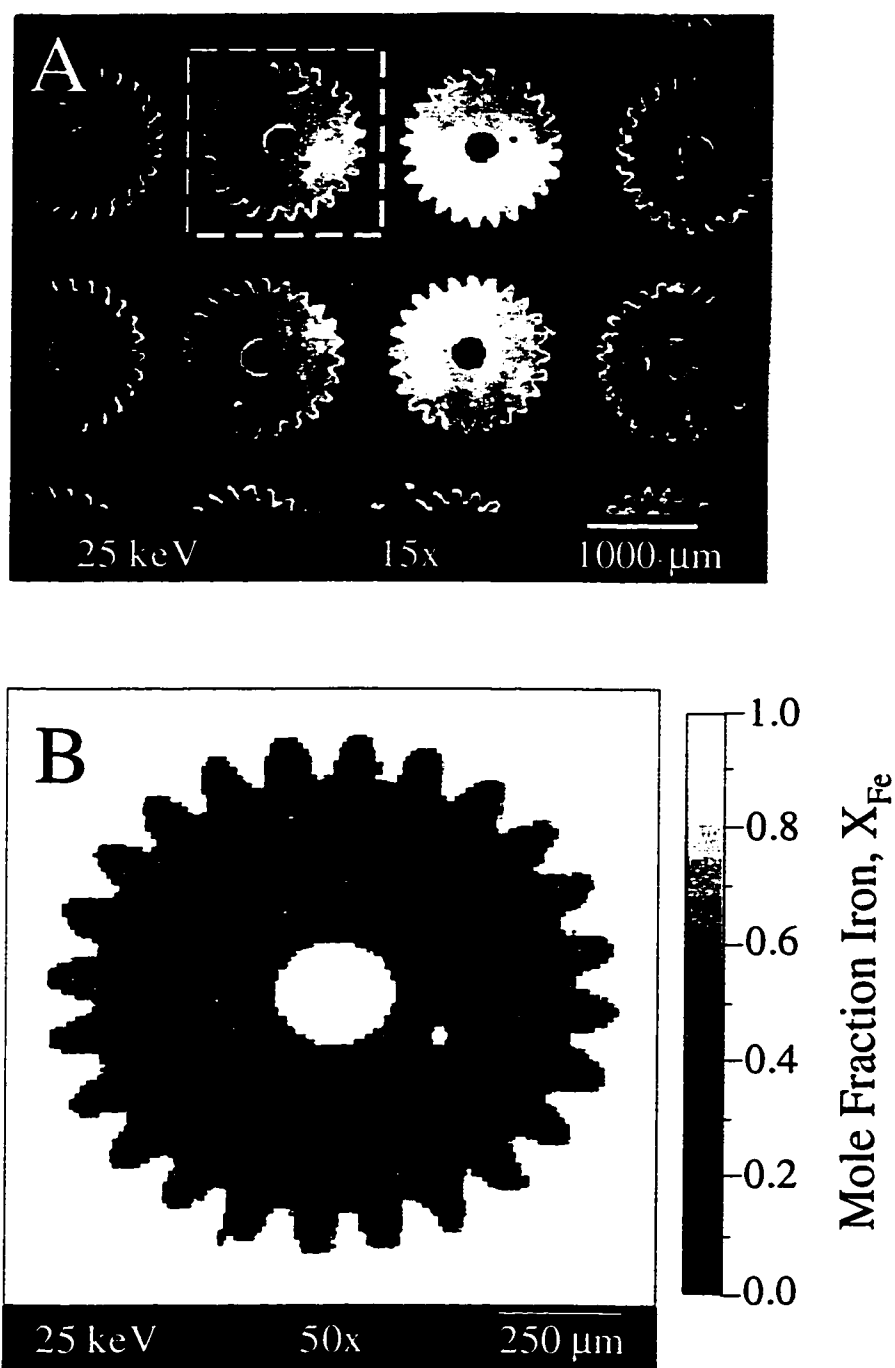
Figure 3.8. (A) Scanning electron micrograph of electrodeposited microgears after planarization, polishing and removal of the PMMA mold. (B) Quantitative EDS composition map of the microgear highlighted in (A).
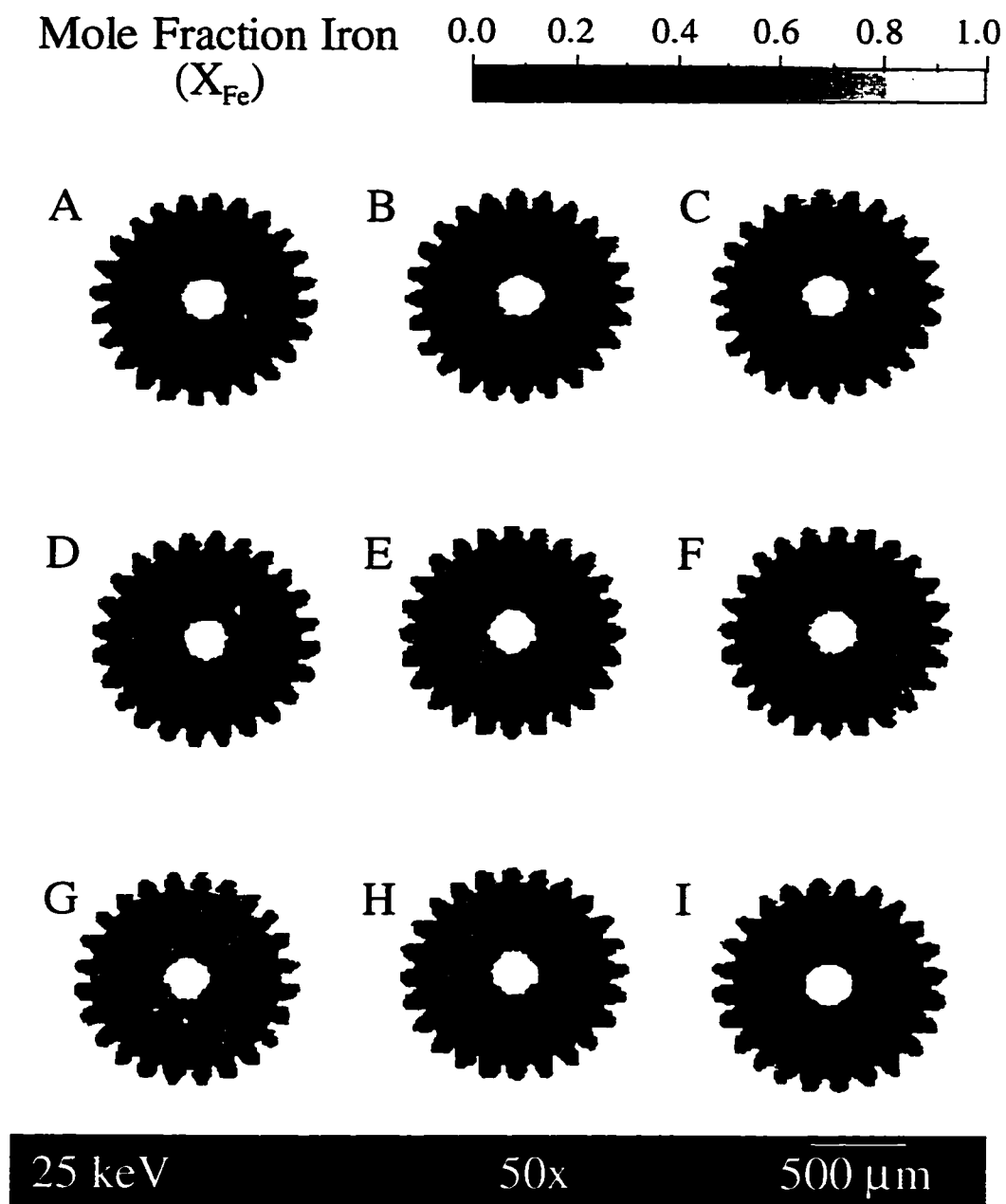
Figure 3.9. Quantitative EDS composition maps of nine microgears electrodeposited at wafer locations corresponding to those labeled A through I in Fig. 3.7.

through I and summarizes the statistical variation in composition. The average composition of the nine microgears is 31 mol% iron with a standard deviation of 6 mol%.

The 95% confidence interval for the nine samples is +/- 5 mol% (two-sided). As was the case in thin film deposition, the statistical results are biased by the gear plated at location G. Analysis excluding the gear from this location results in a slightly lower average composition (29 mol%) as well as a smaller standard deviation and confidence interval. The values in parentheses in Table 3.1 summarize the statistical analysis of microgear composition calculated with the exclusion of the gear from location G.

The average microgear composition is higher in iron content by 7 mol% over the average composition of the corresponding nine locations on the thin film. This variation in average composition is statistically significant ($t_{16} = 2.17, p < 0.05$) and is explained by differences in the development of the concentration boundary layer over the patterned and unpatterned substrate. On the unpatterned substrate, the concentration boundary layer is fully developed and mass transfer limited deposition of iron occurs across the entire electrode. In contrast, the patterned surface has large molded regions where iron is not consumed at the surface, providing a higher average iron composition in the boundary layer.

These results illustrate the need to modify process conditions when plating flow-sensitive alloys through patterned molds. For example, Permalloy ($Ni_{81}Fe_{19}$) can be electroplated onto a rotating disk electrode at -40 mA/cm^2 and k = 0.0041 cm/s using the 25:1 bath, as shown in Chapter 2. Due to the enhanced mixing caused by the molded pattern, however, plating Permalloy microstructures with this bath requires nominal mixing conditions less than 0.0041 cm/s and/or an increased current density. The degree to which mass transfer and polarization must be modified depends on the electrolyte used and the geometry and layout of the patterned features.

A one-way analysis of variance illustrates that there is no statistical difference between the composition variation within the thin film and the composition variation among the microgears ($F_{1,16} = 0.002, p > 0.10$). This shows that while the molded pattern does affect the average composition of the plated parts, it does not introduce additional variability in electrolyte mixing from one location to another when compared to plating onto an unpatterned substrate.

These results suggest that improvements to the UIC will need to focus on re-engineering of the injector. As discussed in Chapter 7, future work should explore the possibility of using micromachining techniques to fabricate an injector with well-defined and spatially uniform flow channels. Two methods appear promising, x-ray lithography to create extremely high aspect ratio and spatially uniform micropores in a PMMA disk and the formation of microchannels in a silicon wafer using deep reactive ion etching. Fabrication of a new frit using either of these techniques is expected to greatly improve pattern scale uniformity in the next generation UIC.

Conclusions

An electroplating device has been designed and characterized based on the uniform injection cell (UIC) concept. Results show that the device delivers predictable and controlled average mass transfer rates at the workpiece length scale. The presence of a patterned mold influences the average mass transfer rate compared to an unpatterned electrode, but does not create additional variability in electrolyte mixing across the substrate. Pattern scale variations in mass transfer result from an imperfect porous frit injector. The device is used to electrodeposit 3-D microstructures and it appears suitable for this application. Improving spatial uniformity in local mass transfer will require fabrication of an engineered frit. As discussed in Chapter 7, future work should focus on the possibility of using micromachining techniques to fabricate a frit with highly uniform electrolyte injection.

CHAPTER 4

Through-Mold Electrodeposition using the Uniform Injection Cell (UIC) :
Feature Scale Uniformity

Summary

In this chapter, an electrodeposition process for achieving high growth rates and yield in NiFe microgears is described with special attention given to feature scale compositional uniformity. Microgears are electrodeposited from a mixed nickel sulfamate/iron chloride electrolyte through a 230 μm thick PMMA mold patterned using synchrotron x-ray radiation. Despite the use of a plating cell with nearly ideal wafer-scale electrolyte mixing characteristics (the uniform injection cell - UIC), a degree of compositional variation in the microgears can arise. The composition variation is shown to be due primarily to non-uniformities in microscopic electrolyte mixing patterns within the mold. To a lesser extent, non-uniformity in the local current distribution also contributes to feature scale composition variation. Improved composition uniformity is achieved when the plating bath is formulated to reduce the sensitivity to electrolyte agitation. Electrodeposition of MEMS components from a low-flow-sensitivity electrolyte using the UIC results in NiFe growth rates greater than 60 μm/hr, yields in excess of 90% and good compositional uniformity.

Background

Many MEMS actuators and sensors incorporate soft magnetic alloys such as electrodeposited NiFe [1, 2, 4-7, 57, 58]. The magnetic properties of electroplated NiFe are dictated by the composition and structure of the deposit which, in turn, are primarily determined by electrolyte mixing at the cathode surface (*i.e.* mass transfer) and the applied current density during plating [2, 12, 13]. Control of these processing variables on multiple length scales is essential for successful through-mold plating of geometrically complex NiFe MEMS components with uniform magnetic properties.

As discussed in previous chapters, three length scales are typically considered in the electrodeposition of microstructures; the workpiece scale (order of 10's of cm), the pattern scale (order of mm), and the feature scale (order of μm) [15, 20]. For LIGA [51, 59, 60] and other thick resist technologies [3, 49, 61-64], the aspect ratio of the plated

component is an especially important dimension of the feature scale. Control of electrolyte mixing and current density at the workpiece (or wafer) scale is primarily governed by the design and operation of the electroplating cell while control of current and mass transfer at the pattern length scale is dictated by details of the mold layout such as the total resist area and the spatial distribution of parts. Considerations in workpiece and pattern scale uniformity in the UIC were addressed in Chapter 3. Precise control of electrolyte mixing and current density on the feature scale, however, is often not possible due to physical constraints on mass transfer processes and current distribution characteristics. A major engineering challenge in the electrodeposition of microstructures with tailored and reproducible properties, therefore, is development of an optimized through-mold plating process in which mass transfer and current density are adequately controlled on the workpiece and pattern scales while non-uniformities on the feature scale are minimized. This challenge is further accentuated by the need to control deposit composition through molds many 100 μm thick with aspect ratios in excess of unity.

Much work has been devoted to optimization of through-mold plating of uniform NiFe deposits for use in magnetic data storage devices [2, 4], but this previous research has generally focused on plating through relatively thin photoresist molds (< 5 μm thick). With the increased interest in fabrication of much thicker, high aspect ratio magnetic MEMS components there exists a need for further development of an electrodeposition process specifically suited for fabrication of these types of structures. In this chapter, we report on the development and optimization of a high rate, through-mold electrodeposition process for fabrication of magnetic NiFe MEMS components with special consideration given to uniformity at the feature length scale. To achieve this goal, we consider the formulation and characterization of a NiFe plating bath, the design and fabrication of a wafer-scale plating apparatus and the traits of a well conceived mold pattern.

To assess and optimize the through-mold plating process, NiFe microgears were galvanostatically electroplated onto a Si/Ti/Cu substrate through a patterned polymethylmethacrylate (PMMA) mold using the UIC plating device described in Chapter 3. Growth and composition uniformity within individual parts and across the wafer were studied using scanning electron microscopy (SEM) in conjunction with energy dispersive x-ray spectroscopy (EDS). Results from the composition and deposit

growth analysis are used to probe the effects of local mixing and current distribution during plating and to investigate effects of process modifications. Based on our studies, a through-mold plating process has been developed capable of plating NiFe MEMS components with a high degree of compositional uniformity at rates of 60 μm/hr with minimal yield loss due to deposit defects.

Experimental

A family of nickel sulfamate/iron chloride electrolytes capable of high rate NiFe plating were developed to operate at room temperature and pH = 3.00, as described in Chapter 2. These baths were comprised of nickel and iron salts, boric acid, sodium saccharin, sodium dodecyl sulfate and ascorbic acid. The chemistry of each bath was identical except for the molar ratio of dissolved nickel and iron (*i.e.* Ni:Fe). In this study, two different plating baths were investigated, one bath in which the dissolved Ni:Fe ratio was 10:1 and another in which Ni:Fe was 25:1. To determine the effects of electrolyte agitation and applied current density on alloy composition, NiFe films were galvanostatically electroplated onto the platinum disk of a rotating ring-disk electrode (RRDE) using a wide range of current densities and well controlled electrolyte mixing rates. The composition of the resulting deposits was determined using potentiostatic stripping voltammetry, a well known electroanalytic technique commonly used to determine the composition of alloys electroplated using the RRDE [12, 44, 65, 66]. Relationships between the electrolyte mixing rates, applied current density and deposit composition for the two plating baths were determined for alloys plated at current densities ranging from -20 to -100 mA/cm^2 (corresponding to growth rates from 23 to 108 μm/hr) and convective mass transfer rates characteristic of weak, moderate and very strong electrolyte agitation. In all RRDE plating and stripping experiments, a Pine Instruments Model AFRDE-5 Bi-Potentiostat was used to control electrode polarization conditions and a Pine Instruments Model MSRX rotator was used to control the steady rotation rate (*i.e.* steady mass transfer conditions) of the RRDE. Details of RRDE experiments are given in Chapter 2.

The electroplating apparatus used in this study is based on the design of the uniform injection cell (UIC), shown conceptually in Fig. 3.1 [46, 54]. As described in Chapter 3, the device essentially consists of two parallel, coaxial disks with a narrow gap, L, between them. The upper disk is a porous frit of radius R mounted in an insulating

tube. The lower disk, also of radius R and coaxial with the frit is the cathode. The anode is placed at the other end of the insulating tube at a distance D>>R. During operation, electrolyte is injected through the frit, into the gap and onto the patterned cathode. In theory, operation of the UIC with small aspect ratio (L/2R << 1) ensures a uniform current distribution and uniform convective mass transfer across the entire workpiece. The device used in this study was fabricated such that L = 0.05 cm, R = 1.1 cm and D = 20 cm, dimensions that satisfy the theoretical operating constraints of the device (*i.e.* L/2R = 0.023).

In all microstructure plating experiments, electrolyte flow to the cathode was controlled using an Ismatic Model 07617-70 positive displacement pump. The pump was capable of delivering a wide range of steady mass transfer conditions to the cathode surface. Before the device was used for plating, convective mass transfer rates in the UIC were characterized by limiting current measurements of ferrous to ferric oxidation in an electrolyte containing 0.02 M $FeSO_4$, 0.04 M $Fe_2(SO_4)_3$ and 1.0 M H_2SO_4. The limiting current density, j_l, is related to physical parameters of the system through the equation $j_l = nFkC_b$ [67]. Here we see that the mass transfer limiting current density, j_l, is proportional to the mass transfer coefficient, k, and the bulk concentration of the ferrous cation, C_b (n=1 is the number of electrons transferred in the reaction and F is Faraday's constant). The mass transfer coefficient is proportional to the strength of electrolyte agitation at the cathode surface with typical values used in this study ranging from $0.0012 \leq k \leq 0.0072$ cm/s (*i.e.* from weak to strong mixing). The DC power supply used during deposition was an EG&G Princeton Applied Research Model 173 Potentiostat. The instrument was operated in galvanostatic mode and microgears were deposited using current densities of -30, -40 and -60 mA/cm^2, corresponding to growth rates ranging from 33 to 65 μm/hr. Further details of the construction, operation and mass transfer characteristics of the electroplating device are presented in Chapter 3.

NiFe microgears 230 μm thick and 1200 μm in diameter were electrodeposited from the nickel sulfamate/iron chloride plating bath onto a Si/Ti/Cu substrate through a PMMA mold defined by synchrotron x-ray radiation [56]. A typical pattern measured 1.1 x 1.6 cm^2 and contained approximately 85 individual microgear components. Plating gears to a thickness of 230 μm typically required between four and seven hours, depending on the current density used. After plating, the microgears were planarized

(while still confined within the PMMA mold) using 15, 6 and 1 μm Engis 1313-T4 oil-based lapping slurries. Microgear parts were further polished using 1 μm Metadi II diamond paste from Buehler. The PMMA was then dissolved from the wafer by immersion in methylene chloride for approximately 30 minutes. Structural and compositional features of the plated microgears were studied using a JEOL JSM-5200 scanning electron microscope (SEM) with QX 2000 energy dispersive x-ray spectroscopy (EDS) instrumentation and software from Link Analytical, Ltd. Quantitative EDS composition maps were constructed using relative peak intensities from the Ni K_α line of the NiFe gears and a polished nickel standard, taking into account ZAF corrections for matrix interactions within the NiFe samples [55].

Results and Discussion

Figure 4.1 illustrates the relationships between plating current density, electrolyte mixing strength and deposit composition as determined from characterization of the 10:1 (A) and 25:1 (B) plating baths. The figure shows that the NiFe deposit composition is sensitive to variations in applied current density and electrolyte agitation, as has been shown for other NiFe plating bath formulations [2, 12, 13]. In general, the iron content in the alloy is enhanced by increases in electrolyte agitation strength and/or decreases in the current density. For a given current density, the composition of the deposit can vary greatly, depending on the mass transfer conditions. Likewise, variations in the current density can dramatically alter the composition of the alloy under constant electrolyte mixing conditions. Consider, for example, plating with the 10:1 bath under controlled mass transfer conditions in which k = 0.0072 cm/s. A change in current density from -20 to -100 mA/cm² results in an alloy composition that varies from 80 to 40 mol% iron.

While both baths exhibit sensitivity to mixing and polarization, the extent of the composition sensitivity depends on the particular bath used. For example, when plating from the 10:1 bath at -60 mA/cm², variation in the mass transfer coefficient from 0.0012 to 0.0072 cm/s results in a deposit that ranges in composition from 12 to 55 mol% iron. Plating under the same polarization and electrolyte agitation conditions using the 25:1 bath, however, results in a deposit in which the composition varies only from 9 to 29 mol% iron. In fact, under all plating conditions, the 25:1 bath is less sensitive to variations in electrolyte mixing and current density. This characteristic of the bath makes
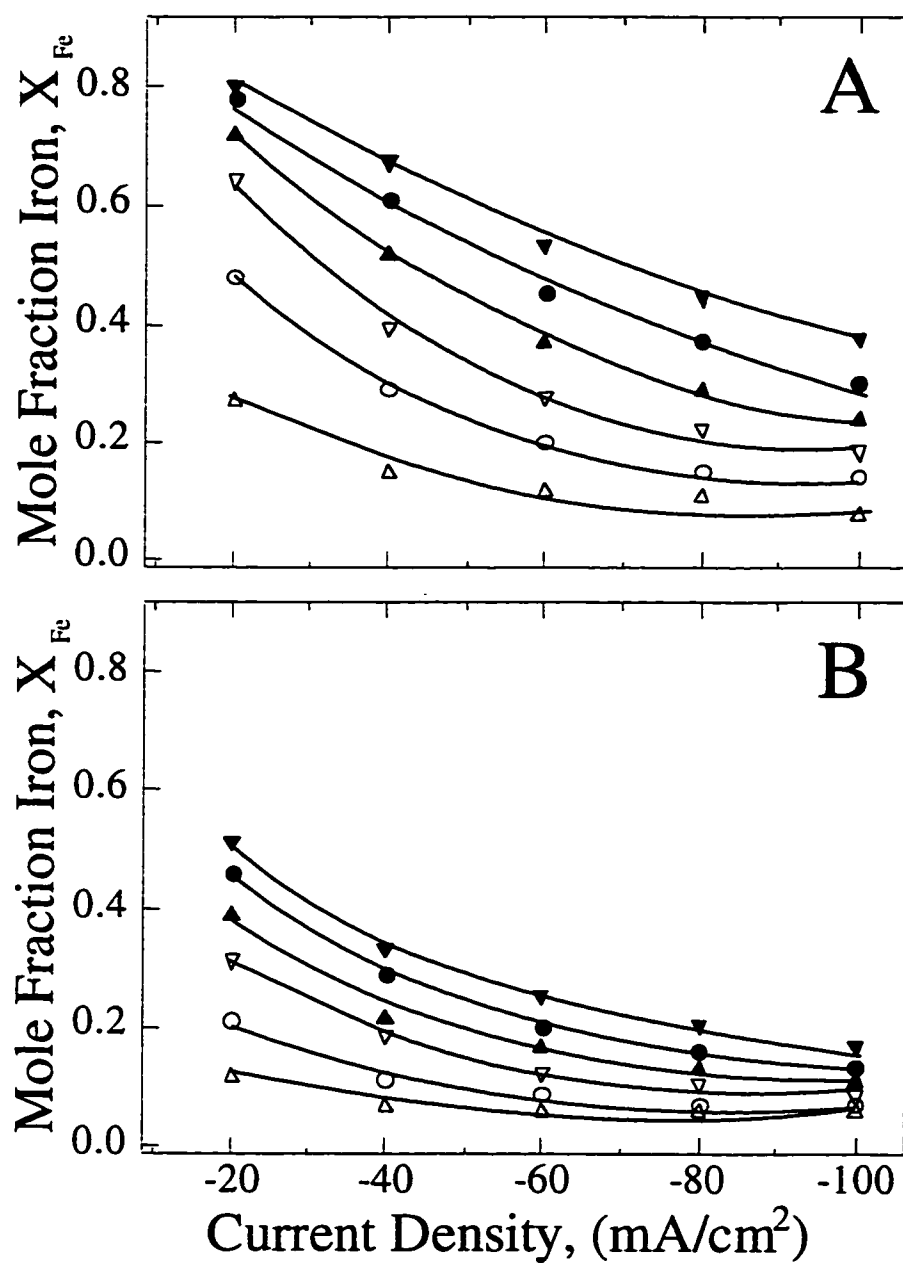
Figure 4.1. Relationships between current density, electrolyte mixing strength and NiFe deposit composition for electrodeposition using the 10:1 (A) and 25:1 (B) plating baths. Results are presented for convective mass transfer rates k = 0.0012 ($\triangle$), 0.0024 (o), 0.0036 (∇), 0.0048 ($\blacktriangle$), 0.0060 ($\bullet$) and 0.0072 ($\blacktriangledown$) cm/s. Solid curves are drawn to aid the eye.

it better-suited for deposition of NiFe microstructures with nearly uniform compositions, as will be discussed later. Nonetheless, Fig. 4.1 shows that with proper control of electrolyte mixing and current density, engineered NiFe alloys with a variety of compositions (and therefore properties) can be electrodeposited from either bath.

While the results in Fig. 4.1 were determined using an unpatterned, planar electrode, the same relationships are applicable to electroplating NiFe MEMS components. MEMS actuators, for example, are sometimes fabricated using electrodeposited Permalloy ($Ni_{81}Fe_{19}$) or Invar ($Ni_{36}Fe_{64}$) [5-8, 36]. From the results in Fig. 4.1, precise mass transfer and polarization conditions required for deposition of these materials are easily determined. Using the 10:1 bath, Invar structures can be deposited at -20 and -40 mA/cm^2 (ca. 23 and 45 µm/hr) so long as adequate electrolyte mixing is provided. Similarly, Permalloy structures can be deposited from the 25:1 bath at rates ranging from -20 to -100 mA/cm^2 (ca. 23 to 108 µm/hr), again provided that proper control of electrolyte mixing is used.

Even though the UIC provides uniform mixing and current distribution at the workpiece scale, composition uniformity in plated microgears is influenced by non-uniformities in electrolyte mixing and current density at the pattern and feature length scales [15, 20]. Non-uniformities in current and electrolyte mixing at the pattern scale have been investigated theoretically and experimentally for a number of simple geometries (e.g. holes and trenches) [14, 16-19]. In Chapter 3, pattern scale uniformity in plated microgears was explored. Based on these previous studies, general principles regarding mold layout and design have been determined which can be applied to any through-mold plating application. The easiest way to significantly minimize pattern scale non-uniformities is to maximize and evenly distribute the electroactive area of the cathode (i.e. the patterned area not covered by resist).

Figure 4.2 is an optical micrograph which shows a representative area of the mold used in this study. This layout represents a good distribution of parts (i.e. evenly spaced and not clustered together) and a relatively high electroactive area covering approximately 62% of the wafer. The close packing and uniform distribution of structures helps reduce current non-uniformities. Further optimization of the pattern is possible, such as removing PMMA from the diamond-shaped regions illustrated in Fig.
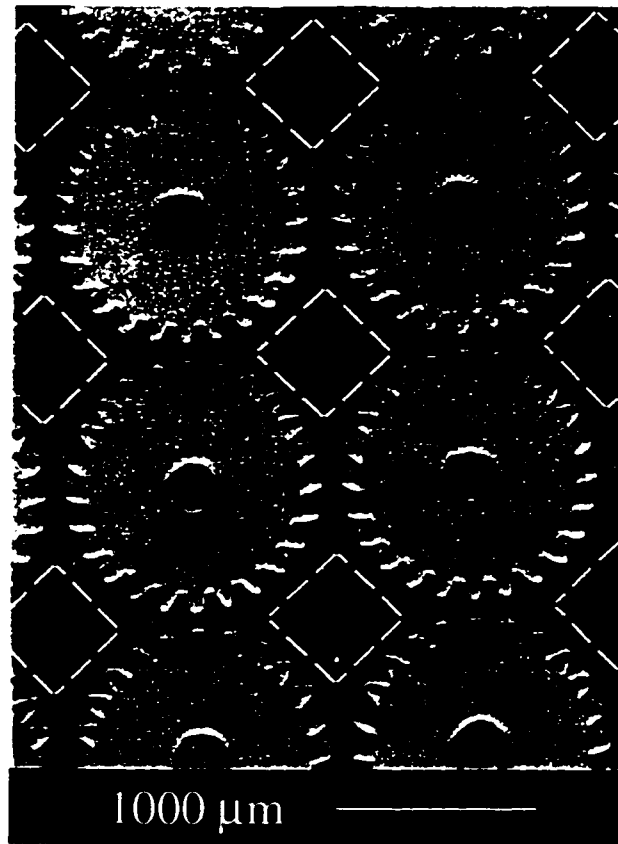
Figure 4.2. Optical micrograph of the PMMA mold used to electrodeposit microgears. The dashed lines illustrate regions of resist that could have been patterned to improve the current distribution across each microgear.

4.2, but such modifications would require study of possible adhesive failure between the PMMA and the wafer.

Figure 4.3 shows an EDS composition map of a microgear electrodeposited from the 10:1 bath at -60 mA/cm^2 and k = 0.0024 cm/s, conditions that should lead to a nominally Permalloy deposit (see Fig. 4.1). In Fig. 4.3, light shading represents areas with relatively higher concentrations of iron. Figure 4.3 (A) shows subtle, but significant composition variation across the entire gear. Electrodeposition theory and practice show that the local current density should be highest near insulating regions of the mold, such

Mole Fraction Iron (X_{Fe})
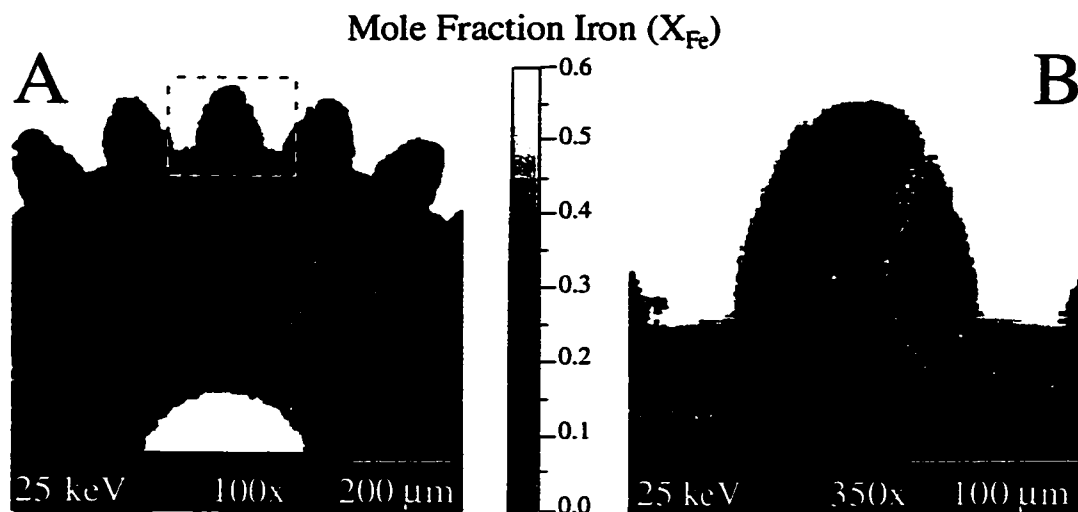
Figure 4.3. EDS composition map of a NiFe microgear electrodeposited from the 10:1 bath at -60 mA/cm². Light shading represents areas with relatively higher concentrations of iron. Composition non-uniformities are evident across the entire gear (A) as well as within individual gear teeth (B).

as in the gear teeth and near the center hub of the gear [4, 15, 20]. From Fig. 4.1, we see that the higher current density should lead to a deposit with lower iron content in these features. However, Fig. 4.3 does not illustrate consistently lower iron concentrations near the hub or throughout the gear teeth. Rather, it appears that local variations in electrolyte agitation within the gear results in composition non-uniformities in these features.

The influence of non-uniform mixing is most easily seen in Fig. 4.3 (B), which illustrates composition variation within an individual gear tooth. In the particular tooth illustrated in Fig. 4.3 (B), the iron content varies from 6 mol% in the dark, central area of the feature to nearly 30 mol% in the light bands that run along either side. The sharp transition from low to high iron concentration suggests the presence of strong mixing eddies in this tooth during plating. Such regions of enhanced electrolyte mixing lead to higher iron content, as can be predicted from Fig. 4.1. Nearly all the gear teeth plated under these conditions exhibited some evidence of small-scale mixing non-uniformities such as this when plating from the 10:1 bath.

Since the local mixing variations at the feature length scale are caused by the complex geometry of the patterned parts, it is not feasible to completely eliminate them while still providing enough mixing to achieve the Permalloy composition. Instead, the feature-scale mass transfer non-uniformity can be minimized by deposition of NiFe microgears from a plating bath that is less sensitive to the electrolyte mixing conditions. Figure 4.4 shows an EDS composition map of the top (A and B) and bottom (C and D) of a microgear electrodeposited from the 25:1 bath at -60 mA/cm^2 and k = 0.0060 cm/s, conditions that should lead to a nominally Permalloy deposit. The gears shown in Fig. 4.3 and Fig. 4.4 both came from the same location on each respective wafer so that cross-wafer variation does not bias the results. Figures 4.3 and 4.4 also use the same gray-scales. It is clear that plating with the 25:1 bath significantly reduces the composition non-uniformities that were so apparent in Fig. 4.3. In Fig. 4.4, the composition is nearly uniform across the entire gear with only slight variations in composition present at the tips of the gear teeth and near the gear hub. As determined from the EDS map, the composition of the top of the gear is a nearly uniform 22 mol% iron (A), close to the Permalloy composition that would result from plating onto an unpatterned cathode. The composition of the bottom, or wafer side, of the microgear (C) is also fairly uniform, exhibiting an average composition of approximately 20 mol% iron. Thus, variations in electrolyte mixing strength as the part grows within the mold result in only slight variation in composition (about 2 mol%) from top to bottom of the gear.

Closer investigation of an individual feature, shown in Fig. 4.4 (B and D), illustrates that the non-uniformities in mixing that caused the significant variations in composition in Fig. 4.3 (B) do not result in widely varying composition when plating from the 25:1 bath. In fact, the average composition of a typical gear tooth is 22 mol% iron on the top and 20 mol% iron at the bottom. This is a direct result of plating with the 25:1 bath. Even though a range of electrolyte mixing conditions are present in a single gear tooth during deposition (as illustrated in Fig. 4.3), the composition does not vary significantly because the 25:1 bath is relatively insensitive to changes in mixing conditions (as shown in Fig. 4.1). Through careful formulation and characterization of the plating bath, a good measure of feature-scale composition uniformity can be achieved.

In addition to deposition of MEMS components with relatively uniform composition, the process described here can also be used to achieve a high throughput of
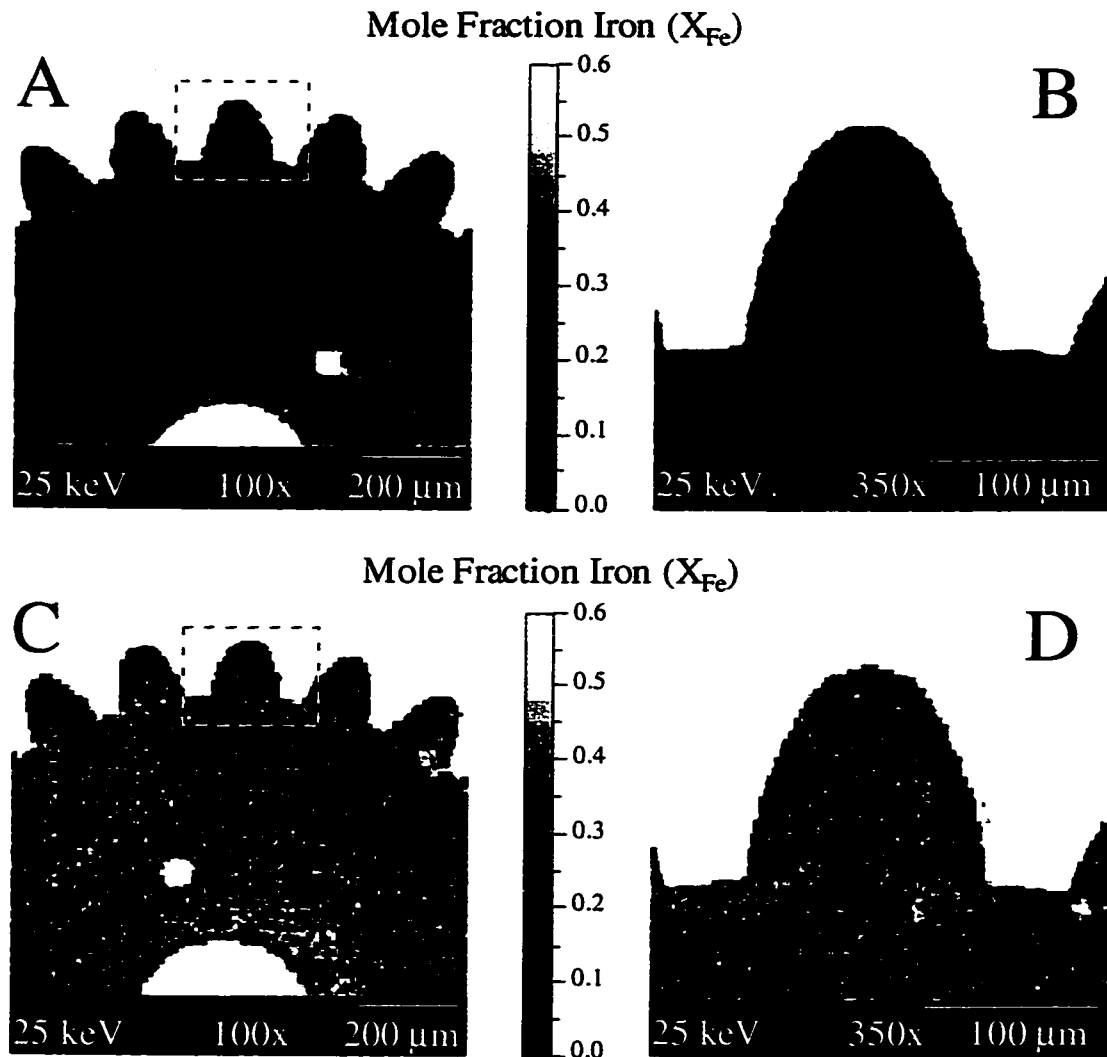
Figure 4.4. EDS composition map of a NiFe microgear electrodeposited from the 25:1 bath at -60 mA/cm². Light shading represents areas with relatively higher concentrations of iron. The composition of the top (A and B) and bottom (C and D) of the microgear is nearly uniform across the entire diameter as well as within individual gear teeth. Note that this microgear has a 50 μm diameter hole in addition to the central hub of the gear.

MEMS components with minimal defects. Figure 4.5 (A) is an SEM micrograph showing electroplated Permalloy microgears before release from the wafer substrate. Microgears shown in this figure were plated at -60 mA/cm² (corresponding to a deposit growth rate of *ca.* 65 μm/hr) using an early design of the UIC, one that incorporated a vertical wafer orientation and no anode gas venting. In many gears plated using this early
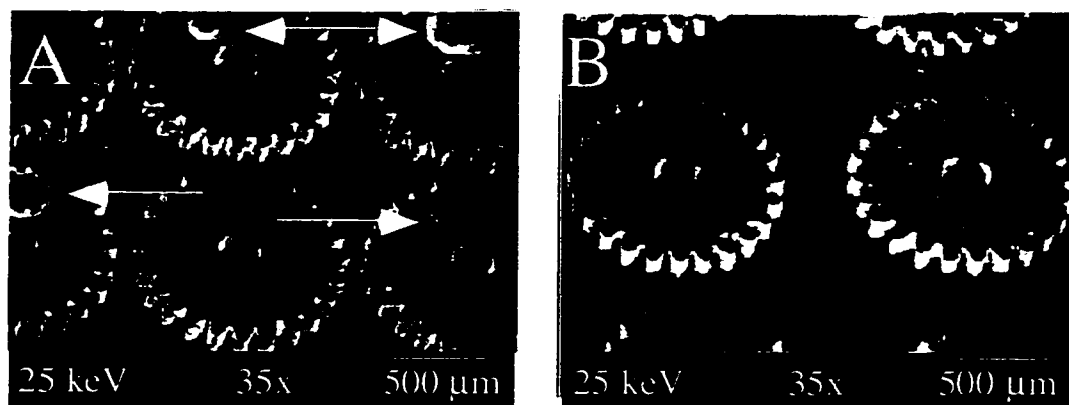
Figure 4.5. SEM micrograph of NiFe microgears electrodeposited at -60 mA/cm² using two different designs of the UIC plating device. Gears plated using an early design are illustrated in (A) and those plated using the re-engineered device are shown in (B). The arrows in (A) point to pit defects in the plated gears.

design, gas evolution and entrapment resulted in pit defects as indicated by the arrows in Fig. 4.5 (A). This problem led to poor component yields (< 20%) in initial studies. The UIC design used in this study incorporates a horizontal wafer orientation with more precise positioning of a re-designed porous frit injector, as described in Chapter 3. These changes, in addition to a different counter electrode placement and a new gas venting system, have resulted in the elimination of gas-entrapment defects during plating. Figure 4.5 (B) is an SEM micrograph of gears plated under similar conditions as those in Fig. 4.5 (A) and illustrates the improved performance of the modified UIC. No pit defects are evident and the resulting gears exhibit smooth and well defined vertical side walls. Design improvements to the UIC have led to higher part throughput (NiFe plating rate > 60 µm/hr) and yields exceeding 90%.

Conclusions

By addressing and optimizing the fundamental aspects of through-mold electrodeposition, we have developed an electroplating process especially suited for high throughput, high yield deposition of magnetic NiFe MEMS components. Compared to plating with an earlier (but not naive) bath formulation and plating device, we have realized a 10-fold increase in NiFe part throughput. Results of plating with the optimized process illustrate that composition variation within electrodeposited parts can be

minimized through the systematic investigation of current distribution and electrolyte mixing characteristics on the workpiece, pattern and feature length scales.

In some plating applications, however, controlled composition variation can be desirable. In Chapters 5 and 6 we explore NiFe electrodeposition under well-controlled modulated mass transfer conditions and illustrate the value of plating thin films and 3-dimensional microstructures using this technique.

CHAPTER 5

Characterization of Flow-Induced Compositional Structure in Electrodeposited NiFe CMAs

Summary

In this chapter, we expand on the results of Chapter 2 to explore plating of NiFe alloys using time-periodic convective mass transfer conditions. Flow-induced NiFe composition modulated alloys (CMAs) are plated onto the disk of a rotating ring disk electrode (RRDE) by oscillating the RRDE rotation rate during galvanostatic deposition. The relationships between processing and compositional structure in the electrodeposited CMAs are explored using an optimized potentiostatic stripping voltammetry (PSV) technique, scanning electron microscopy (SEM) and energy dispersive x-ray spectroscopy (EDS). Results show that the CMA wavelength scales as the inverse of the flow oscillation frequency and the composition modulation amplitude is strongly affected by variations in both electrolyte flow oscillation frequency and amplitude. Fast Fourier transform (FFT) analysis is used to probe the dynamic time scales of NiFe electrodeposition and to investigate the sensitivity of NiFe deposition to the oscillating electrolyte flow field. Results indicate that critical deposition chemistries occur over time scales much slower than those governing typical mass transfer processes.

Background

An emerging area of materials research is the plating of alloys with a spatially periodic composition in one dimension, referred to as composition modulated alloys (CMAs). The composition modulation wavelength and the modulation amplitude are two parameters often used to define the periodic structure of a CMA. The wavelength represents the repeat length, or period, of the composition modulation, and the amplitude is a measure of the interlayer composition variation. It is well established experimentally that many CMA properties (*e.g.* magnetostriction, magnetoresistance, electrical resistivity, and yield strength) are strongly affected, directly or indirectly, by the alloy wavelength and amplitude [68-71]. The engineering of alloys with specific properties, therefore, depends in part on the ability to tailor the compositional structure (*e.g.* CMA wavelength and amplitude) through the control of processing variables.

CMAs with a wide range of composition modulation wavelengths and amplitudes have been made in a variety of ways, including electrodeposition and vapor phase techniques [27-32]. Electrodeposited, short wavelength CMAs are typically made by periodic pulsing of the plating current during deposition. CMAs with nanometer-scale wavelengths can also be made by galvanostatic deposition in a sub-Hertz oscillating electrolyte flow field using the rotating ring disk electrode (RRDE), as described in Appendix A. In this previous study, potentiostatic stripping voltammetry (PSV) was used to evaluate the wavelength of flow-induced NiFe CMAs and to relate this alloy feature to processing variables such as current density and flow oscillation frequency. While this previous study was the first to illustrate the experimental electrodeposition of flow-induced CMAs and the use of PSV in quantitative assessment of the modulation wavelength, the RRDE stripping technique was not optimized, preventing accurate determination of the composition modulation amplitude.

To better explore the relationships between processing variables and compositional characteristics in flow-induced CMAs, we have optimized the PSV technique so that it is possible to assess both the CMA wavelength and amplitude, at least semi-quantitatively. In this chapter, composition profiles of NiFe CMAs deposited in the time periodic flow of a RRDE are analyzed using the improved PSV technique. The profiles show periodic composition variation with modest attenuation throughout the depth of the deposit. Analysis of the composition profiles using fast Fourier transforms (FFTs) results in a reciprocal space composition profile which allows quantitative analysis of the average CMA wavelength and semi-quantitative characterization of the modulation amplitude. The FFT analysis is also used to probe the dynamic time scales of NiFe electrodeposition and to investigate the sensitivity of NiFe deposition to a low frequency oscillating electrolyte flow field. Comparison to CMA analysis using scanning electron microscopy (SEM) and energy dispersive x-ray spectroscopy (EDS) illustrates that the optimized PSV technique is a fast and accurate characterization tool.

Experimental

A Pine Instruments RRDE with a platinum disk of radius $r_1=0.229$ cm and concentric platinum ring with inner radius $r_2=0.246$ cm and outer radius $r_3=0.269$ cm was used throughout the electroplating and stripping voltammetry experiments. The RRDE, a large area platinum mesh counter electrode and a saturated calomel (SCE) reference

electrode were used in single chambered plating and stripping vessels. A Pine Instruments Model MSRX rotator driven by an external voltage source was used to control the instantaneous rotation rate of the RRDE. During electrodeposition, a Wavetek function generator was used to drive the disk rotation with a well-defined periodic waveform (sinusoidal). A Pine Instruments Model AFRDE5 Bi-Potentiostat was used to control the disk and ring polarization during plating and stripping. Disk and ring currents were monitored continuously during stripping using a Macintosh Centris 650 personal computer interfaced with the bi-potentiostat through a National Instruments 12 bit multi-function A/D board. Disk and ring current acquisition and calculation of the alloy composition profile were performed using custom software written in the LABVIEW programming environment. FFT analysis of the composition profiles was performed using the Igor Pro software package.

The plating bath was composed of 0.2 M Ni $(H_2NSO_3)_2 \cdot 4 \; H_2O$, 0.01 M $FeCl_2 \cdot 4 \; H_2O$, 0.40 M H_3BO_3, 1.5 g/l sodium saccharin, 0.2 g/l sodium dodecyl sulfate and 1.0 g/l ascorbic acid and was operated at room temperature ($\sim$23 °C). Bath pH was kept constant at 3.00 +/- 0.01 by addition of HCl and/or NaOH between plating runs. The stripping bath composition was 0.2 M HCl and 0.5 M NaCl and was also operated at room temperature. Both plating and stripping baths were made from reagent grade chemicals and 18 MΩ-cm deionized water.

Prior to each plating run, the disk and ring electrodes were cleaned by cyclic potential scanning at 100 mV/s between -300 to +1300 mV vs. SCE for approximately 15 minutes in a 0.2 M HCl / 0.5 M NaCl electrolyte. After cleaning, NiFe thin film CMAs were plated galvanostatically onto the disk of the RRDE using an applied current density of -20 mA/cm^2. During plating, the ring potential was set to +800 mV vs. SCE to prevent metal deposition on the ring. Unless noted otherwise, plating during PSV experiments was terminated after a total charge of roughly 500 mC, resulting in a deposit nearly 1000 nm thick.

During deposition, convective mass transfer to the disk surface was modulated in a time-periodic manner by oscillating the disk rotation rate with the sinusoidal waveform

$$\Omega(t) = \Omega_0 + \Delta\Omega \cos (2\pi\sigma t), \qquad (5.1)$$

where $\Omega(t)$ is the instantaneous rotation rate, Ω_0 is the mean rotation rate, $\Delta\Omega$ is the rotation rate oscillation amplitude and σ is the oscillation frequency. The dimensionless disk rotation oscillation amplitude is defined as $\alpha = \Delta\Omega/\Omega_0$. Throughout the study, a constant mean rotation rate of $\Omega_0 = 26.67$ Hz (1600 rpm) was employed. In all experiments, plating was initiated and terminated at the minimum rotation rate of the waveform. To fully investigate the effect of time periodic flow on alloy composition, a range of disk rotation oscillation amplitudes and frequencies were used. Compositional characteristics of NiFe CMAs were determined for alloys plated in sinusoidal flows with disk oscillation frequencies of 4, 10, 20, 40, 80, 160 and 320 mHz and dimensionless disk oscillation amplitudes of 0.1, 0.3, 0.5, 0.7, 0.9 and 0.95.

After each plating run, the RRDE was removed from the plating bath, immersed in deionized water and rotated to prevent contamination of the stripping bath. The RRDE was then submerged in the stripping solution and rotated at a constant rate of 2500 rpm. The disk potential was set to +250 mV vs. SCE to oxidize the alloy, liberating Ni^{+2} and Fe^{+2} from the film surface. The ring potential was set to +800 mV vs. SCE to detect Fe^{+2} via the mass transfer limited reaction $Fe^{+2} \rightarrow Fe^{+3} + e^-$. The disk and ring currents were recorded continuously during stripping to allow determination of the film composition profile, as detailed in Appendix A. Preliminary stripping studies were performed to determine the best disk stripping potential to achieve high quality, reproducible composition profiles. The primary concern in optimization of the PSV technique was to determine a stripping potential which resulted in oxidation of successive compositional strata in the CMA film. The use of an appropriate oxidation potential was evident in the stripping voltammograms by the absence of significant attenuation in the modulation amplitude of the alloy as stripping progressed (*cf.* Fig. 5.1 here and Fig. A.2 in Appendix A). Potentials from 0 to +300 mV vs. SCE were investigated to find the optimum stripping conditions and +250 mV proved to be the best potential for the NiFe films investigated here.

Using the same potentiostat, rotator and plating bath described above, flow-induced NiFe CMAs were also plated onto the removable disk of a rotating disk electrode (RDE). Prior to plating, the removable copper disk electrode (radius = 0.25 cm) was polished to a mirror finish using 1.0 μm diamond paste and cleaned by immersion in 5%

H_2SO_4 for 60 seconds. After rinsing with deionized water, the copper RDE was placed in a single chambered electroplating vessel with SCE reference electrode and platinum mesh counter electrode. NiFe CMAs were plated galvanostatically using an applied current density of -20 mA/cm^2 until a charge of roughly 10,700 mC had passed, resulting in a deposit 15 μm thick on average. During deposition, the disk rotation rate was oscillated at a frequency of $\sigma = 4$ mHz and dimensionless amplitude of $\alpha = 0.95$ using a constant mean rotation rate $\Omega_o = 26.67$ Hz. After plating, the RDE was again rinsed with deionized water and then immersed in a standard Watt's plating bath [27] from which a 300 μm thick nickel layer was electroplated over the NiFe film.

The plated copper disk electrode was removed from the RDE housing and cut in cross section using a diamond wafering blade. Cross section samples were polished to a mirror finish using 1.0 μm diamond paste and mounted on standard 1.25 cm diameter aluminum SEM sample stubs. NiFe CMA cross sections were studied using a JEOL JSM-5200 SEM and EDS instrumentation and software developed by Link Analytical Ltd. Quantitative EDS composition maps and profiles were constructed using relative peak intensities from the Ni K_α line of the NiFe sample and a polished nickel standard, taking into account ZAF corrections for matrix interactions within the NiFe sample [55]. Structural and compositional details of the NiFe CMAs were investigated at a number of radial positions on the cross section, from the center of the disk to the edge, although an intermediate radial position was used for all analyses that were compared directly to results from PSV, as described later.

Results and Discussion

Potentiostatic Stripping Voltammetry

Figure 5.1 shows a typical stripping voltammogram (A) and corresponding composition profile (B) for a NiFe CMA electrodeposited at -20 mA/cm^2 in an oscillating flow field of frequency $\sigma = 40$ mHz and dimensionless oscillation amplitude $\alpha = 0.95$. As shown in (A), the disk and ring currents oscillate as the CMA is electrochemically stripped from the disk. The disk current oscillates due to the enhanced oxidation rate of Fe-enriched strata and the ring current oscillates in response to the periodic flux of liberated ferrous ions from the oxidized film. At the end of stripping, the disk and then the ring current falls to zero.
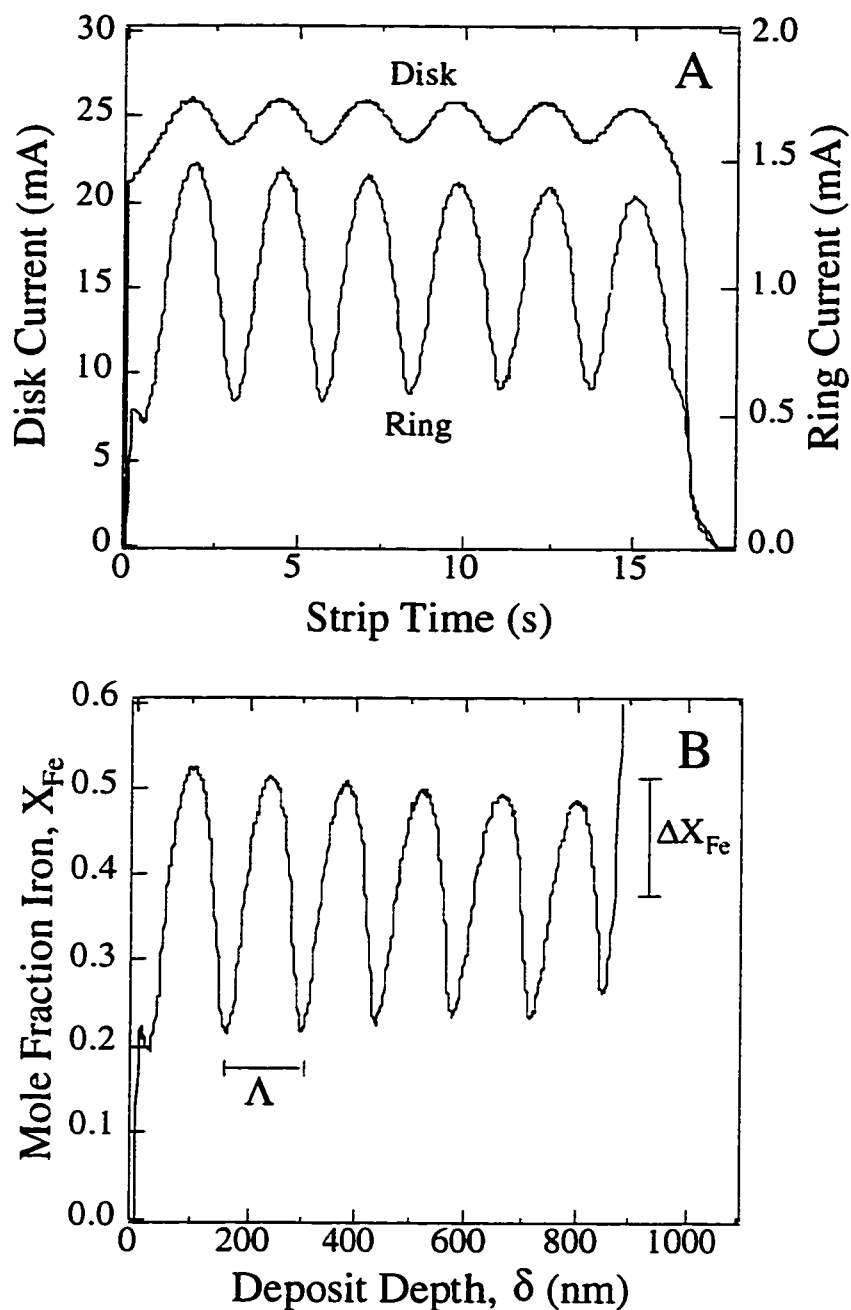
Figure 5.1. (A) Typical stripping voltammogram for a NiFe CMA deposited in a sinusoidal oscillating flow with $\sigma = 40$ mHz and $\alpha = 0.95$. The measured disk and ring currents are shown as a function of stripping time. (B) Corresponding composition profile determined from the stripping voltammogram in (A). The mole fraction iron in the deposit is plotted as a function of deposit depth. The average CMA wavelength, Λ, and composition modulation amplitude, ΔX_{Fe}, can be estimated as indicated.

The corresponding composition profile is shown in Fig. 5.1 (B). Here the mole fraction of iron in the deposit, X_{Fe}, is plotted as a function of alloy depth, δ. The alloy composition and depth were determined using the measured disk and ring currents in the manner described in Appendix A. The variation in iron content is evident throughout the depth of the deposit. Six complete composition modulation cycles are present in the deposit, with each cycle being roughly 140 nm in length (as measured between consecutive maxima or minima). This repeat length is the average wavelength of the CMA, denoted Λ. The composition modulation amplitude, ΔX_{Fe} for the deposit is defined here by the difference between the average composition maxima and the mean composition of the alloy. The CMA in Fig. 5.1 exhibits an average composition modulation amplitude of about 14 mol% and a mean iron content of 36 mol%. Thus, on average, the alloy has a minimum iron content near 22 mol% and a maximum around 50 mol%. The shape of the PSV composition profile is similar to the computed composition profile for an ideal non-interacting binary pair [72]. Specifically, the profile is characterized by broad, high concentration regions followed by quick '"dips" into the low mole fraction strata. However, as discussed later, the electrodeposition of NiFe displays a number of dynamic traits quite different from an ideal binary pair.

A desirable consequence of using the optimized stripping technique is the high spatial fidelity of the composition profile (here we use the term high spatial fidelity to describe a profile in which all composition modulations are evident and only modest attenuation from the first period to the last is observed). Using the non-optimized stripping conditions in our previous study, one typically found that the amplitude of each successive modulation decreased appreciably (cf. Fig. A.2 in Appendix A). In general, the spatial fidelity of profiles from the optimized PSV technique is better than one typically finds using destructive characterization methods such as Auger spectroscopy with sputtering [28]. This is presumably due to the matching of plating and stripping current distributions on the disk electrode. That is, even though the deposit plates faster and is thicker at the disk edge (compared to the center of the disk), the stripping rate matches this non-uniformity and etches the edge region proportionally faster. The result is a high fidelity composition profile with features representative of the average properties of the film. To assess the utility of the optimized PSV technique in characterization of NiFe CMAs, we compared the method to deposit analysis using SEM imaging and x-ray spectroscopy.

SEM and EDS Analysis

Figure 5.2 (A) is a secondary electron image of a polished NiFe CMA cross section plated onto a copper substrate. The film was deposited at -20 mA/cm^2 in an oscillating flow field of frequency σ = 4 mHz and dimensionless oscillation amplitude α = 0.95. The micrograph clearly shows the substrate, compositional strata in the NiFe film and the protective nickel overlayer. As one would expect, given the non-uniform current distribution on the RDE, typical CMA cross sections exhibited a relatively thin NiFe film (~10 μm) near the center of the disk and a much thicker deposit (~17 μm) at the disk edge. The micrograph in Fig. 5.2 (A) illustrates the compositional structure of the film at a radial location midway between the center and edge of the disk, at a film thickness of roughly 13 μm. This film location was chosen for characterization because analysis at an intermediate radial position is the closest approximation to sampling the average properties of the film as is possible using EDS. Since the PSV technique provides information about average film properties, composition analysis at this radial position allows a more accurate comparison between the EDS and PSV characterization methods.

Figure 5.2 (B) shows an EDS composition map and typical x-ray energy spectra of compositional strata from the boxed region in Fig. 5.2 (A). Contrast differences in the map correspond to different alloy compositions; Fe-enriched regions appear dark and Fe-deficient regions are lighter. A periodic composition variation is clearly evident in the film. Using Ni $K\alpha$ peak intensities from the sample and a pure nickel standard, quantitative composition analysis of the region in Fig. 5.2 (B) allowed construction of the CMA composition profile shown in Fig. 5.3 (A). The figure shows the composition variation across five successive strata of the film and illustrates a CMA with a wavelength of approximately 1,400 nm and a modulation amplitude of nearly 9 mol%. The resolution of the profile, however, limits the utility of this technique, as discussed below. Figure 5.3 (B) is a PSV composition profile of a NiFe CMA plated under identical polarization and flow oscillation conditions as were used to plate the alloy shown in Fig. 5.2. The two profiles in Fig. 5.3 illustrate similar features; both techniques capture the general shape of the composition wave and either could be used to estimate Λ and ΔX_{Fe}. The PSV technique, however, measures a modulation amplitude nearly 7 mol% greater than the EDS method and the shape of the composition wave is more
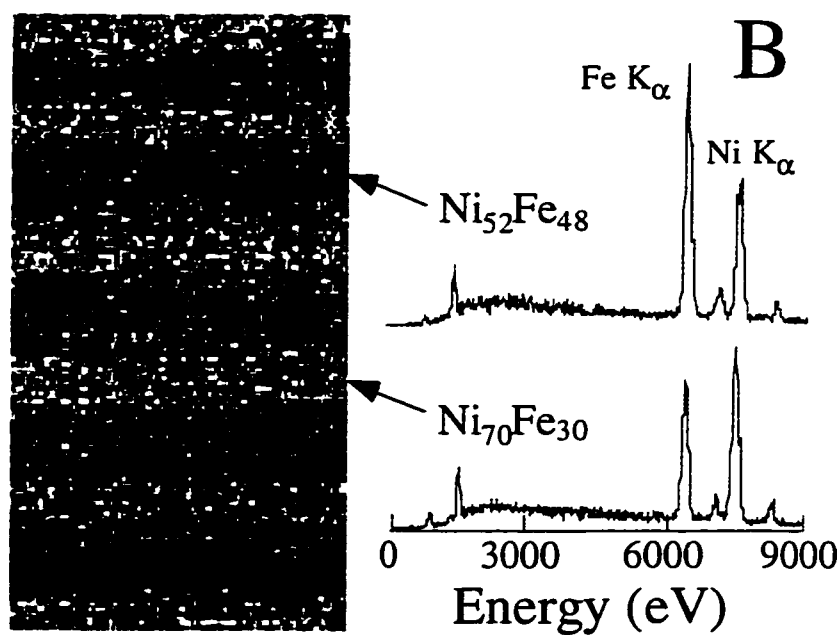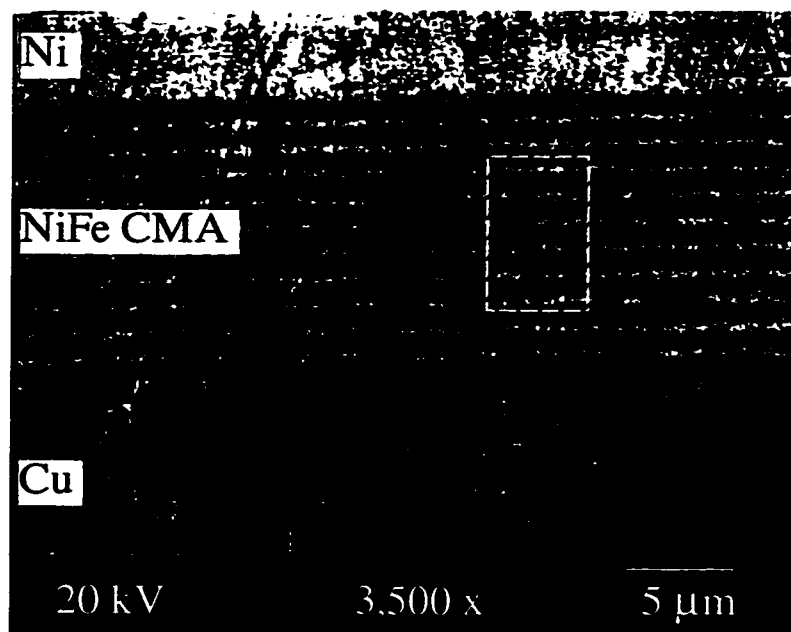
Figure 5.2. (A) SEM micrograph of a polished NiFe CMA cross section. The micrograph shows the copper substrate, compositional strata in the NiFe alloy and the protective nickel overlayer. (B) EDS composition map and x-ray energy spectra of compositional strata from the boxed region of the CMA in (A). Fe-enriched strata appear dark and Fe-deficient regions are lighter.
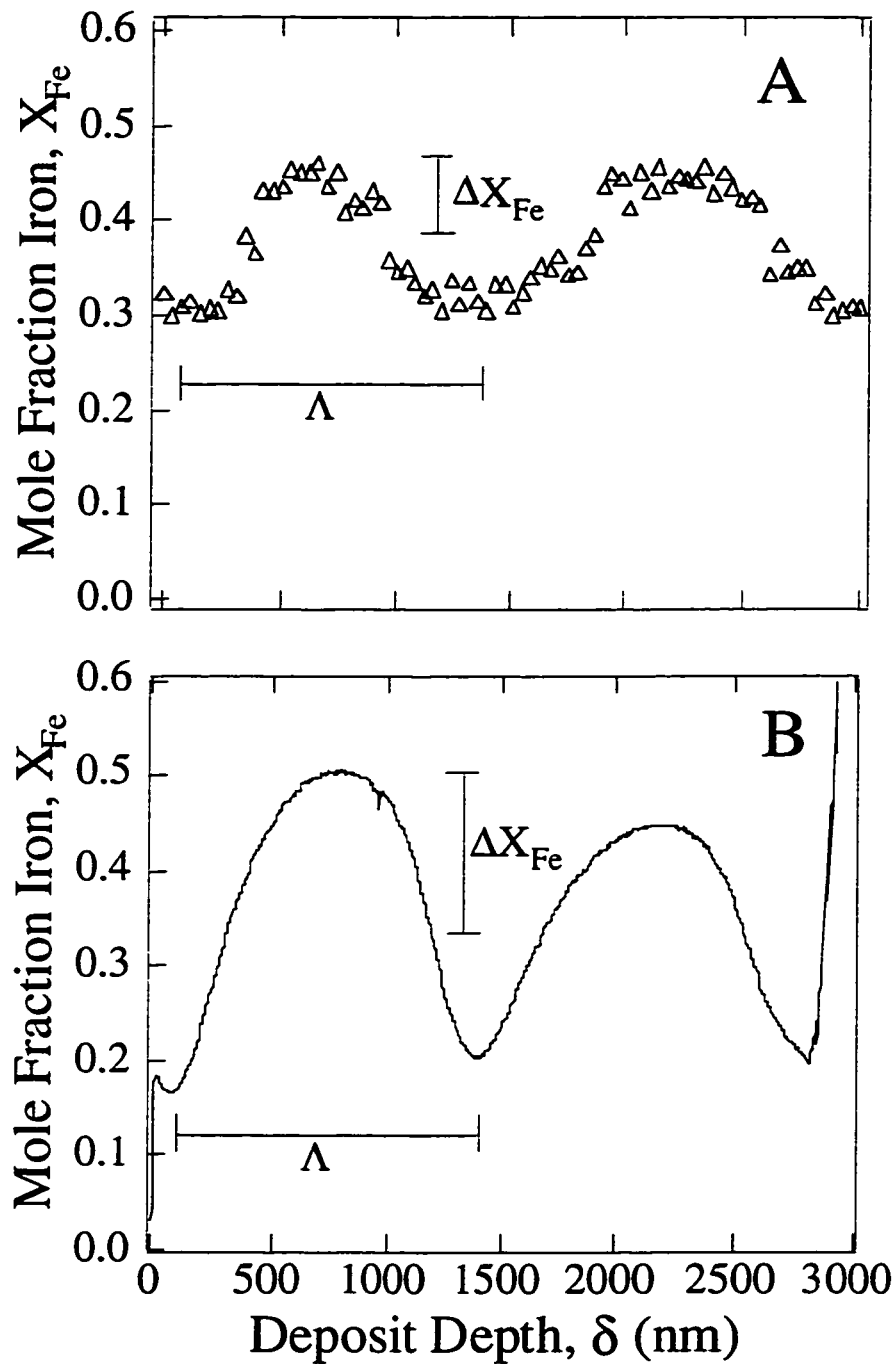
Figure 5.3. (A) Composition profile of NiFe CMA constructed using quantitative EDS analysis. Spatial and compositional resolution in the EDS profile is compromised due to lateral spreading of the x-ray signal from the sample surface. (B) PSV composition profile of a NiFe CMA plated under identical polarization and flow oscillation conditions as the film in (A).

readily apparent, *i.e.* the broad, high iron regions and the more narrow, low iron regions are clearly represented in the PSV profile, but are not discernible in the EDS analysis.

Accurate determination of Λ and ΔX_{Fe} using either characterization technique is subject to the spatial and compositional resolution of the given method. In EDS analysis, spatial and compositional resolution is compromised due to lateral spreading of the x-ray signal from the sample surface during acquisition [55]. Since the detected x-ray signal originates from an interaction volume with a diameter approaching 1 μm, high resolution quantification of successive strata of this or smaller length scales (such as in the CMA of Figs. 5.2 and 5.3) becomes difficult. The "'smearing" of signal between successive CMA strata suggests that the modulation amplitude determined using EDS should be viewed as an absolute lower bound to the actual composition modulation present in the alloy film. Effectively, the EDS method is only reliable in analysis of CMAs with wavelengths greater than 1 μm, with resolution improving for thicker, micron scale composition modulations. The spatial and compositional resolution of the PSV technique, however, is tied directly to how well the plating and stripping current distributions are matched. If the current distributions are not well matched, then simultaneous etching of many compositional strata will occur and the true composition of any given strata will be underestimated, much like the "smearing" of signals in x-ray analysis. Conversely, if the plating and stripping current distributions are well matched, the result is a high fidelity composition profile such as those in Fig. 5.1 and Fig. 5.3 (B).

Quantitative Composition Profiling Using FFT Analysis

We have shown that the optimized stripping voltammetry technique can be used to construct reasonably high fidelity composition profiles of the flow-induced CMAs. Using Fig. 5.1, the general characteristics of the spatially periodic waveform can be determined by inspection, *i.e.* the CMA wavelength is roughly 140 nm and the composition modulation amplitude is about 14 mol%. Subtle differences in compositional structure, however, are not always evident when the data is plotted as a spatial profile. Fourier transformation of the original composition profile not only illustrates details of the alloy composition profile, but also reveals the influence of electrolyte flow dynamics on the resulting alloy composition waveform.

To illustrate the procedure and utility of using FFTs in the present study, consider Fig. 5.4. Figure 5.4 (A) is a composition profile determined from the electrochemical stripping of a film made at -20 mA/cm^2 in a sinusoidal flow of oscillation frequency σ = 80 mHz and dimensionless amplitude α = 0.95. As in Fig. 5.1, the variation in iron mole fraction throughout the depth of the film is clearly evident in Fig. 5.4 (A), and an estimate of alloy modulation wavelength and amplitude can be made directly from the figure. The average wavelength is approximately 70 nm and the average modulation amplitude is about 9 mol%.

The FFT of the composition profile Fig. 5.4 (A) is shown in Fig. 5.4 (B) and the construction and interpretation of the FFT representation merits brief discussion. The FFT algorithm requires a data set in which the number of data points is an integral power of 2. We selected 512 data points from the composition profile $X_{Fe}(\delta)$, starting from the end of the first complete modulation as labeled in Fig. 5.4 (A). In this example, the 512 data points contain 8 complete composition modulation periods. Depending on the wavelength of the CMA, 2 to 32 complete modulation periods were typically included in the 512 points. A Hanning window was then applied to minimize the effect of aliasing. The FFT of the composition profile $X_{Fe}(\delta)$ results in a complex data vector, $\chi_{Fe}(k)$, containing real and imaginary values representing the composition profile in reciprocal space. For the original data set $X_{Fe}(\delta)$, the FFT was computed using

$$\chi_{Fe}(k) = \frac{2}{N} \sum_{m=0}^{N-1} X_{Fe} e^{2\pi i \cdot mk/N} = A_k + iB_k , \qquad (5.2)$$

where $\chi_{Fe}(k)$ represents the mole fraction of iron as a function of CMA reciprocal space (k), A_k is the real part of $\chi_{Fe}(k)$, B_k is the imaginary part of $\chi_{Fe}(k)$, and $i^2 = -1$. The magnitude of each discrete peak in reciprocal space, $|\chi_{Fe}(k)|$, was calculated using the real and imaginary parts of the transformed data,

$$\left|\chi_{Fe}(k)\right| = \sqrt{A_k^2 + B_k^2} . \qquad (5.3)$$

Figure 5.4 (B) shows $|\chi_{Fe}(k)|$ as a function of location in reciprocal space. Peaks occur at k = n /Λ, where Λ is the spatial period of the CMA and n is an integer $\geq$ 1. The
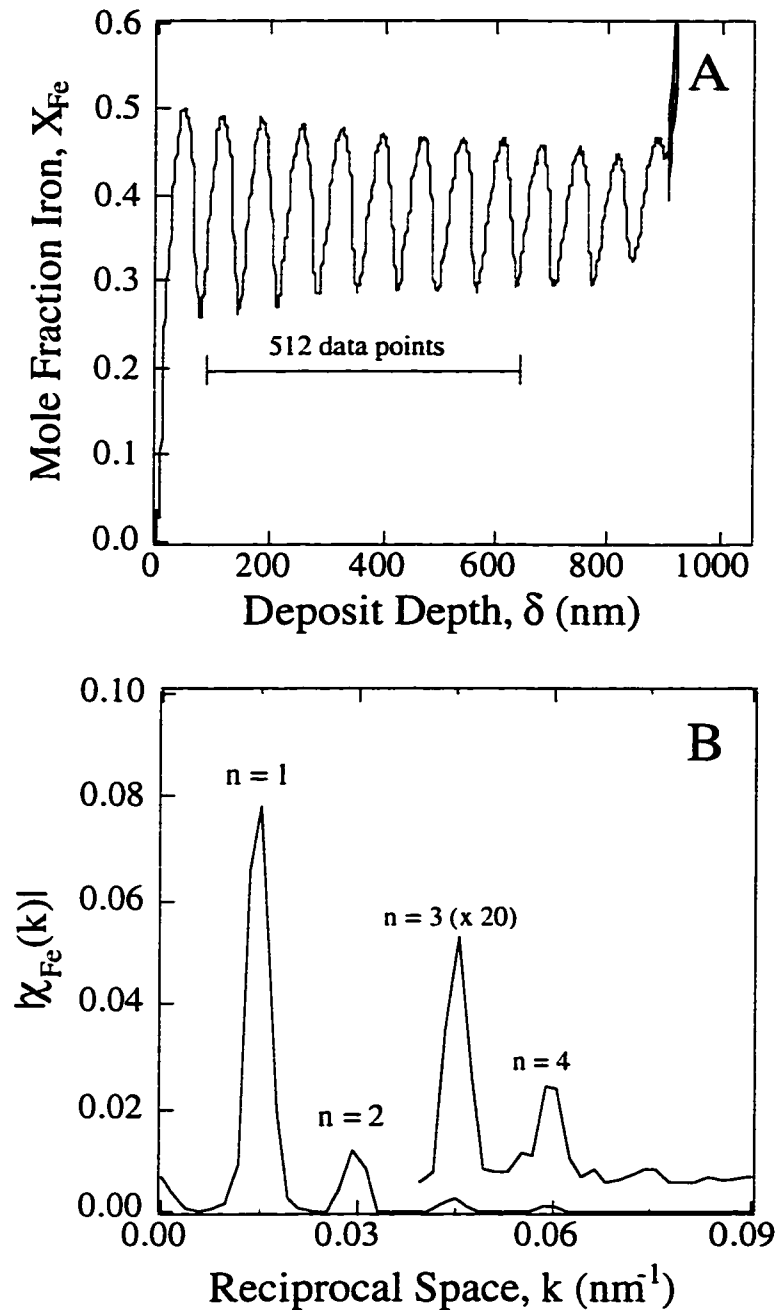
Figure 5.4. (A) Spatial composition profile of a NiFe CMA deposited in a sinusoidal flow with σ = 80 mHz and α = 0.95. (B) FFT of the composition profile shown in (A). The characteristic CMA amplitude, $|\chi_{Fe}(k)|$, is plotted as a function of reciprocal space, k. The fundamental peak at k = $1/\Lambda$ is used to quantify the average CMA wavelength and characteristic amplitude.

peak at $k = 1/\Lambda$ is the fundamental peak of the waveform and is used to determine the average wavelength and characteristic amplitude of the CMA. In Fig. 5.4 (B), $1/\Lambda = 0.015$ nm^{-1}, or $\Lambda = 67$ nm, which agrees with the estimated average wavelength determined from Fig. 5.4 (A). The characteristic composition modulation amplitude is read directly from Fig. 5.4 (B) as the magnitude of the fundamental peak at $n = 1$. In this example, the magnitude is 0.08 (corresponding to a modulation amplitude of 8 mol%), which represents the characteristic amplitude for all modulations in the CMA. This value also agrees with that determined from Fig. 5.4 (A).

While both modulation wavelength, Λ, and modulation amplitude, ΔX_{Fe}, are readily determined in either real space or reciprocal space, subtle traits of the compositional waves are more apparent in the reciprocal space representation. The magnitude and location in reciprocal space of each peak relative to the fundamental peak provides detail about the compositional structure in the CMA and the role of nonlinear dynamic response to the sinusoidal disk oscillation. For example, when operated under small amplitude, linear conditions, disk oscillations at a single frequency (*e.g.* a sinusoidal waveform) produce a response (*e.g.* the periodic composition variation) containing only a single peak at $k = 1/\Lambda$. Conversely, large amplitude, sinusoidal disk oscillations produce a nonlinear dynamic response characterized by the presence of harmonic satellites in the reciprocal space profile [73]. For example, in Fig. 5.4 (B), the presence of satellite peaks located at $k = n/\Lambda$, where $n \geq 2$, indicates that the large amplitude sinusoidal disk oscillation ($\alpha = 0.95$) results in a non-sinusoidal compositional variation.

Relationship between Processing and Compositional Structure

Figure 5.5 illustrates the effect of varying the waveform oscillation frequency on the alloy composition profile. Shown are real and reciprocal space composition profiles for films plated with a disk rotation oscillation amplitude of $\alpha = 0.90$ and oscillation frequencies of $\sigma = 40, 80$, and 160 mHz. These figures show that when the disk rotation oscillation frequency is doubled, the average modulation wavelength is halved. The reduction in wavelength at higher frequencies is represented by shifts in the peak locations in reciprocal space. At higher frequencies, all peaks shift to larger values of reciprocal space, *i.e.* shorter wavelengths. For example, at 40 mHz, the fundamental peak occurs at $k = 1/\Lambda = 0.0075$ nm^{-1}, or $\Lambda = 133$ nm. At an oscillation frequency of 80 mHz,
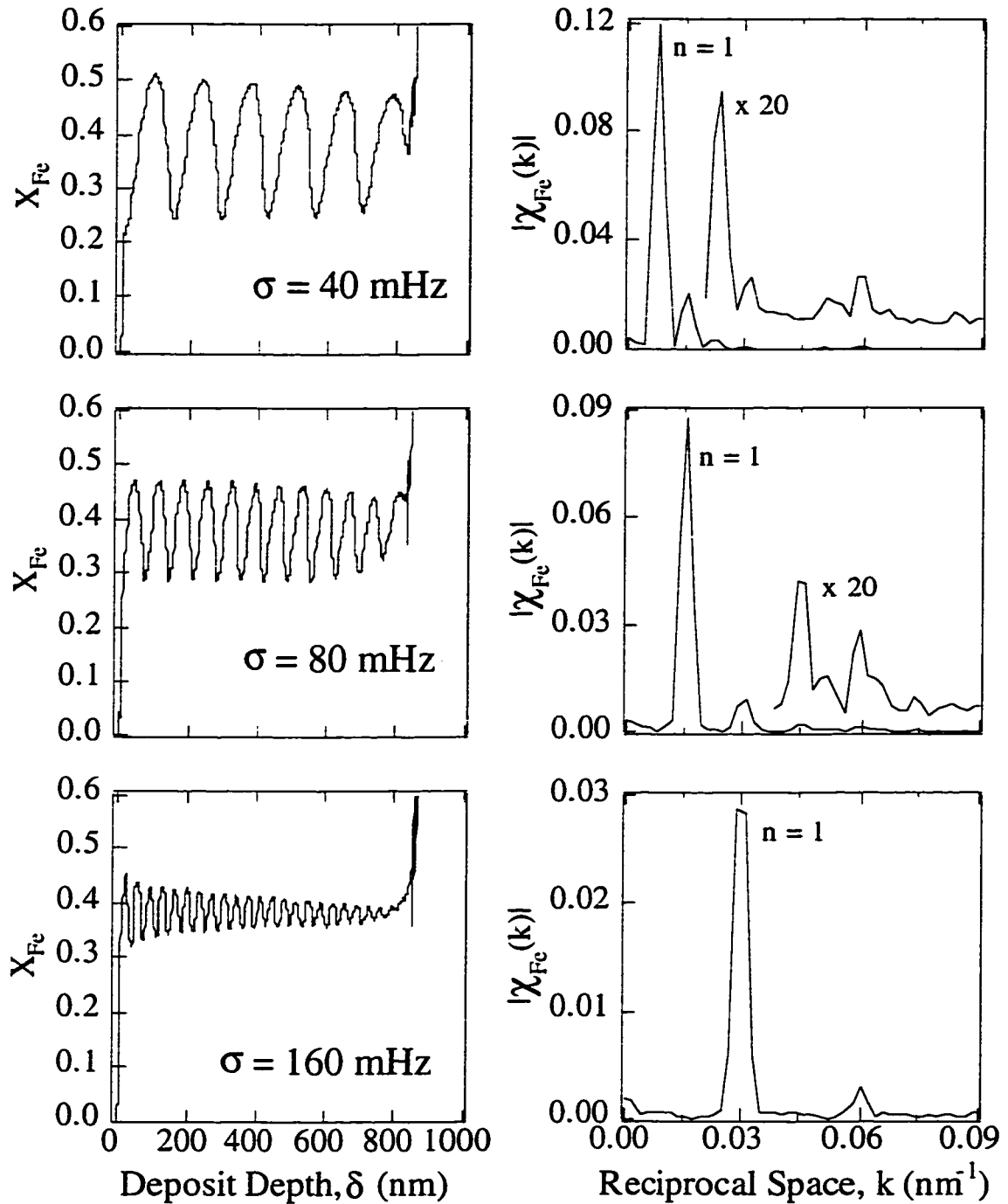
Figure 5.5. Real and reciprocal space composition profiles for NiFe CMAs deposited in a sinusoidal flow with oscillation amplitude $\alpha = 0.90$ and oscillation frequencies of $\sigma =$ 40, 80 and 160 mHz. At higher flow oscillation frequencies, all peaks shift to higher values of reciprocal space (shorter wavelengths) and the characteristic modulation amplitude at $k = 1/\Lambda$ decreases.

$\Lambda = 67$ nm and at 160 mHz, $\Lambda = 33$ nm. In addition to the peak shifts, it is also seen that as the oscillation frequency is increased, the composition modulation amplitude decreases. For example, the magnitude of the fundamental peak decreases from 0.12 at 40 mHz to 0.09 at 80 mHz to 0.03 at 160 mHz.

For a given frequency, a change in the oscillation amplitude affects the alloy composition profile as well. Figure 5.6 shows reciprocal space composition profiles from three films made at a frequency of 80 mHz and oscillation amplitudes of 0.70, 0.50 and 0.30. Again, characteristic modulation amplitudes and wavelengths can easily be determined from the composition profile in reciprocal space. As the disk rotation oscillation amplitude is decreased, the composition modulation amplitude decreases as well. The magnitude of the fundamental peak and all satellite peaks is reduced at lower disk rotation oscillation amplitudes. The composition modulation amplitude decreases from 0.035 at dimensionless oscillation amplitude $\alpha = 0.70$, to 0.016 at $\alpha = 0.50$ to 0.005 at $\alpha = 0.30$. Since the three films in Figure 5.6 were plated with the same oscillating flow frequency, no peak shifts are evident in reciprocal space and the fundamental peak falls at $k = 0.015$ nm^{-1} for each film, corresponding to an average CMA wavelength of 67 nm. In addition to affecting the magnitude of the fundamental and satellite peaks in reciprocal space, the flow oscillation amplitude, α, also has a significant impact on the distribution, or relative magnitude, of the satellite peaks. As shown in Fig. 5.6, the reciprocal space spectrum becomes dominated by the fundamental peak at $k = 1/\Lambda$ as the flow oscillation amplitude decreases. The declining magnitude of the satellite peaks relative to the fundamental peak at low flow oscillation amplitudes (most clearly seen at $n = 2$, or $k = 2/\Lambda$) illustrates the expected non-linear response of the oscillating RDE system [73].

The relationships between processing and compositional structure in NiFe flow-induced CMAs are summarized in Fig. 5.7 and Fig. 5.8. Figure 5.7 (A) is a plot of the measured average CMA wavelength as a function of the flow oscillation frequency. The expected inverse relationship between oscillation frequency and CMA wavelength is evident, indicating that the PSV-FFT method provides a quantitative picture of the characteristic modulation period. Plotted are data points from each stripping voltammetry experiment at every oscillation amplitude and frequency (except $\sigma = 4$ mHz) and the best fit line through the data. The data set includes CMAs with a wide range of
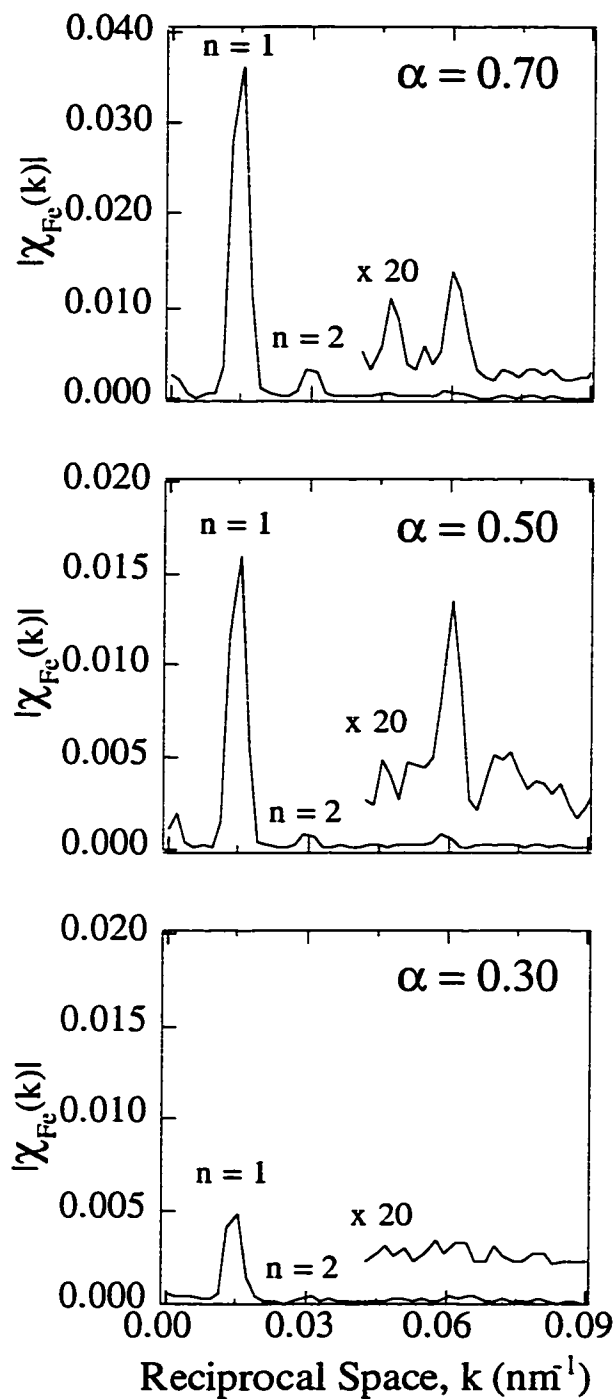
Figure 5.6. Reciprocal space composition profiles for NiFe CMAs deposited in a sinusoidal flow with oscillation frequency of σ = 80 mHz and oscillation amplitudes of α = 0.70, 0.50 and 0.30. The characteristic modulation amplitude at k = 1/Λ decreases as the flow oscillation amplitude is reduced.
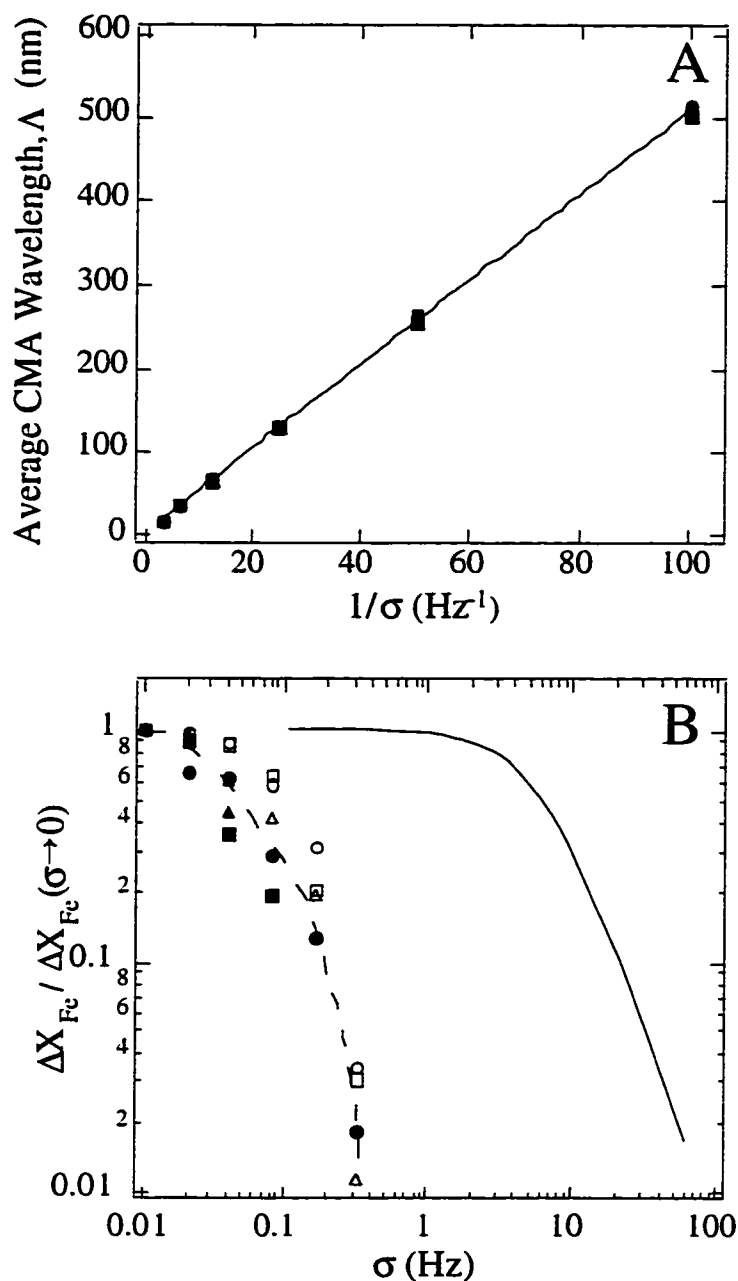
Figure 5.7. (A) Measured average CMA wavelength as a function of disk rotation oscillation frequency. Data from each PSV experiment at every flow oscillation amplitude and frequency (except $\sigma = 4$ mHz) is included along with the best fit line through the data points. The data obey the expected inverse relationship between CMA wavelength and flow oscillation frequency given by Eq. (5.4). (B) Normalized CMA amplitude as a function of disk rotation oscillation frequency for $\alpha = 0.10$ (▲), 0.30 (■), 0.50 (●), 0.70 (△), 0.90 (□) and 0.95 (o). The solid line is the frequency response expected for electrodeposition of an ideal binary alloy with no interactions between the co-depositing species.

wavelengths, from 17 to 540 nm. At all amplitudes and frequencies, the data agree well with the theoretical relationship

$$\Lambda = \left(\frac{\hat{V}_{NiFe}}{2F}\right)\frac{\eta j}{\sigma} \,, \tag{5.4}$$

where $\hat{V}_{NiFe}$ is the mean molar volume of the alloy, η is the plating current efficiency, j is the plating current density, and F is Faraday's constant.

Figure 5.7 (B) shows a log-log plot of the normalized composition modulation amplitude as a function of the flow oscillation frequency. The data points represent results from all experimental runs in which a discernible modulation amplitude existed. The wide spread in the data for any given frequency suggests that using PSV-FFT provides, at best, a semi-quantitative measure of the modulation amplitude. The data indicate the presence of a quasi-steady composition modulation plateau at very low oscillation frequencies and a sharp decline in the flow-induced composition modulation amplitude as the frequency is increased above 20 mHz. The solid line in Fig. 5.7 (B) represents the theoretical frequency response for a mass transfer limited species with Sc = 2300 [74] (the kinematic viscosity of the electrolyte and diffusivity of Fe^{+2} are estimated from lab measurements to be 0.011 cm^2/s and 4.7 x 10^{-6} cm^2/s, respectively). This curve illustrates the expected behavior of an ideal binary alloy with one species mass transfer limited and the other kinetically limited with no interactions between the two co-depositing species. The ideal theory predicts deviation from the quasi-steady regime to occur at oscillation frequencies on the order of 1 Hz due to concentration boundary layer relaxation effects which are normally slower than kinetic time scales [73-75]. Differences between the theoretical curve and the experimental data suggest that the deposition of NiFe does not behave as an ideal binary pair and illustrate that the dynamics of NiFe electrodeposition are extremely slow, even when compared to normal convective-diffusive time scales. The very slow dynamics of NiFe electrodeposition have been noted, but not investigated at frequencies below 200 mHz [76, 77]. It is possible that the slow dynamics of NiFe electrodeposition illustrated here may be responsible for the observation that CMA structures are seemingly not induced in the ca. 1 Hz oscillating flows produced by a conventional industrial paddle cell.
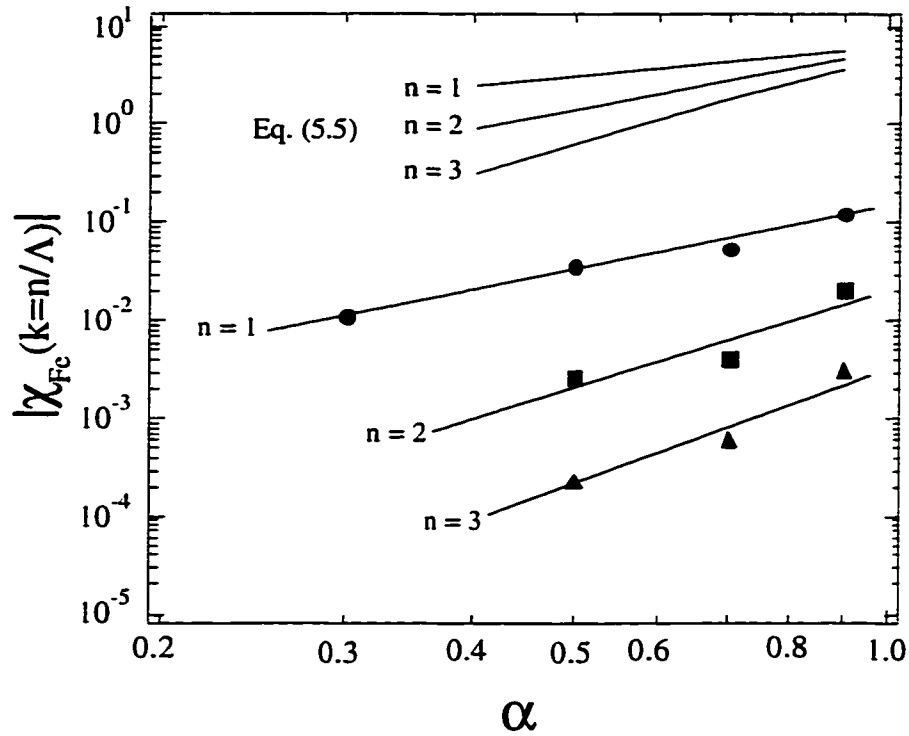
Figure 5.8. Magnitude of the nth peak as a function of the disk rotation oscillation amplitude for CMAs made at a frequency $\sigma = 40$ mHz. Best fit lines are drawn through the data for the fundamental peak ($\bullet$) and the $k = 2/\Lambda$ ($\blacksquare$) and $k = 3/\Lambda$ ($\blacktriangle$) satellites. Reference lines indicate the expected slope for each peak according to Eq. (5.5).

The sensitivity of NiFe deposition to electrolyte flow oscillation can be characterized by the magnitude of the fundamental and satellite peaks in the reciprocal space composition profiles. If NiFe were an ideal binary pair characterized by mass transfer limited Fe deposition and simple kinetically controlled Ni deposition, one would find that the peaks in the FFT composition profile grow in accordance with a power law relationship

$$\left| \chi_{Fe}(k = \frac{n}{\Lambda}) \right| = K_n \alpha^n , \tag{5.5}$$

for all $n \geq 1$, where K_n is a constant for the nth peak [73]. We see that this relationship does not hold for NiFe deposition, but rather that the composition modulation amplitude

is more sensitive to the flow oscillation amplitude than predicted by Eq. (5.5). Figure 5.8 shows the relationship between the measured composition modulation magnitude and the disk oscillation amplitude used during plating of films made at 40 mHz. The data are plotted on a log-log plot to emphasize the expected power law relationship. The solid lines are best-fit plots of the fundamental peak and the $n = 2$ and $n = 3$ satellites. Reference lines have been added above the experimental data to indicate the expected slope for each peak according to Eq. (5.5). For all peaks, the best fit lines exhibit a larger slope than predicted from theory. The slope of the fundamental peak is approximately 2.5, and the slopes for the $n = 2$ and $n = 3$ satellites are roughly 3.5 and 4.5, respectively. The larger than expected slope exhibited by all the peaks in reciprocal space reiterates the well-known fact that the deposition of NiFe is especially sensitive to electrolyte agitation rate [12]. This enhanced dependence on electrolyte mixing suggests that NiFe deposition exhibits highly non-linear kinetics with respect to the concentration of surface species.

Conclusions

We have shown that optimized PSV, when combined with FFT analysis, is a reasonable technique for the compositional characterization of electrodeposited NiFe CMAs. This method allows fast and reliable estimation of CMA wavelength and amplitude and compares favorably to other characterization techniques such as Auger and x-ray spectroscopy. In the characterization of flow-induced NiFe CMAs, PSV was used to illustrate the effect of different electrolyte flow field conditions on the compositional structure of the alloy. The PSV-FFT technique was also used to probe the dynamic time scales of NiFe electrodeposition and to illustrate the enhanced sensitivity of NiFe deposition to oscillating electrolyte flows. Results indicate that critical deposition chemistries occur over time scales much slower than those governing typical mass transport processes. Due to the enhanced sensitivity to low frequency flow oscillations, electroplating flow-induced NiFe CMAs with novel structural characteristics may be possible.

CHAPTER 6

In-Situ Fabrication of Sacrificial Layers in Electrodeposited NiFe Microstructures

Summary

This chapter describes the development of a fabrication and etching process for the *in-situ* formation of sacrificial layers in electrodeposited NiFe magnetic alloys. Sacrificial layers consist of iron-rich material electrodeposited in a nickel-rich matrix. The iron-rich layers are formed using a pulsed electrolyte agitation scheme. The removal of sacrificial layers is investigated using a concentrated acid etching procedure as well as a potential-enhanced etching technique. The formation of sacrificial layers in electrodeposited microgears and planar films is demonstrated. We find that glacial acetic acid preferentially removes the sacrificial layers at a rate of 0.5 μm/hr while leaving the remaining nickel-rich structure unaffected. An applied potential is used to accelerate the etch rate of sacrificial material in dilute acetic acid as well as in a chloride-based etching solution. Under potential control, sacrificial layers are etched at rates approaching 80 μm/hr. The remaining nickel-rich matrix is not significantly affected during etching and retains its structural fidelity. NiFe sacrificial layers of varying compositions are shown to etch at rates proportional to iron content. The implications for using these techniques in conventional through-mold plating applications are discussed.

Background

The use of sacrificial materials is common in fabrication of 3-dimensional microstructures such as integrated circuits and microelectromechanical systems (MEMS) [1, 3, 4, 78]. A common aspect in many of these techniques is the requirement to "build" sacrificial volumes using a time consuming repetition of masking, exposure, deposition and etching procedures. The formation of sacrificial volumes *in-situ* as the microstructure is deposited would represent a significant improvement in the fabrication procedure, eliminating additional masking, exposure and deposition steps [25]. To have utility as a viable micromachining technique, such a process would need to exhibit highly selective and controlled removal of the sacrificial material with minimal alteration of non-sacrificial structures. In this study, we explore the possibilities of creating *in-situ* sacrificial volumes in microstructures using electrodeposited NiFe alloys. The removal

of sacrificial material is studied using a wet chemical procedure as well as a potential controlled etching technique.

Control of plating current and electrolyte agitation during deposition of NiFe microstructures allows the creation of layers of iron-rich material that can be preferentially removed at a later time leaving behind a well defined 2 or 3-dimensional structure. We first illustrate this technique by depositing and selectively removing iron-rich layers from NiFe microgears electrodeposited through a patterned plastic mold. Selective removal of sacrificial layers in the microgears is illustrated using a slow acidic etch process.

An accelerated selective etching study using dilute acid with potential control is used to explore high rate removal of sacrificial layers. NiFe etching characteristics under potential control are investigated through the plating and etching of thin films using the rotating ring-disk electrode (RRDE). NiFe microstructures with well-defined compositional layers are then electrodeposited onto a rotating disk electrode (RDE) and *in-situ* etch selectivity and rate characteristics are explored. Results show that the accelerated etching technique is much faster than the conventional acid etch without compromising selectivity. Some implications for using this technique in conventional through-mold plating applications are explored.

Experimental
Through-Mold Electrodeposition of Microgears

NiFe microgears 230 μm thick and 1200 μm in diameter were electrodeposited from a nickel sulfamate/iron chloride plating bath onto a Si/Ti/Cu substrate through a PMMA mold defined by synchrotron x-ray radiation [56]. The plating electrolyte was composed of 0.2 M nickel sulfamate, 0.02 M iron chloride, 0.4 M boric acid, 1.5 g/l sodium saccharin, 0.2 g/l sodium dodecyl sulfate and 1.0 g/l ascorbic acid, as described in Chapter 2. Microgears were electrodeposited galvanostatically using an EG&G Princeton Applied Research Model 173 Potentiostat at a current density of -60 mA/cm^2, corresponding to a growth rate of approximately 65 μm/hr. Deposition was carried out using the uniform injection cell (UIC), a plating device developed in our laboratory and described in detail in Chapter 3. Use of the UIC permits control of convective mass transfer to the electrode surface during deposition. Microgears were plated using a pulsed

convective mass transfer rate. The pulsed electrolyte agitation leads to deposition of a microstructure with well defined compositional layering in the growth direction, as illustrated in Chapter 5. Plating at low mass transfer rates was used to create thick (approximately 17 μm) nickel-rich layers and deposition at high mass transfer rates was used to create thin (approximately 3 μm) iron-rich layers.

After deposition, the microgears were planarized (while still confined within the PMMA mold) using 15, 6 and 1 μm Engis 1313-T4 oil-based lapping slurries. Microgear parts were further polished using 1 μm Metadi II diamond paste from Buehler. The PMMA was then dissolved from the wafer and iron-rich sacrificial layers were preferentially etched by immersion of the microgears in a glacial acetic acid etching bath at 40 °C for 12 hours. Structural and compositional features of the plated microgears were studied using a JEOL JSM-5200 scanning electron microscope (SEM) with QX 2000 energy dispersive x-ray spectroscopy (EDS) instrumentation and software developed by Link Analytical, Ltd. Quantitative EDS composition maps were constructed using relative peak intensities from the Ni K_α line of the NiFe gears and a polished nickel standard, taking into account ZAF corrections for matrix interactions within the NiFe samples [55].

NiFe Thin Film Deposition and Etching

To determine the effects of applied potential and alloy composition on etching rates, NiFe films were electroplated onto the platinum disk of a rotating ring-disk electrode (RRDE) and subsequently etched under potential control in a dilute acid solution. The same nickel sulfamate/iron chloride plating bath described above was used in electrodeposition of the NiFe thin films. In all RRDE plating and etching experiments, a Pine Instruments Model AFRDE-5 Bi-Potentiostat was used to control electrode polarization conditions and a Pine Instruments Model MSRX rotator was used to control the steady rotation rate (*i.e.* steady mass transfer conditions) of the RRDE. Thin films of NiFe were electrodeposited galvanostatically at -40 mA/cm^2 onto the steadily rotating disk of the RRDE until a total charge of 200 to 800 mC had passed, resulting in deposits between 0.4 and 1.6 μm thick. By careful selection of RRDE rotation rates during deposition, NiFe films were plated with average compositions of 20, 30, 40, 50, 60 and 65 mol% iron (the exact mass transfer conditions used to achieve these compositions are illustrated in Chapter 2).

After each film was plated, the RRDE was removed from the plating bath and cleaned with deionized water to prevent contamination of the etching solution. The RRDE was submerged in the etching solution and rotated at a constant rate. The open circuit potential for the NiFe film was then measured. The disk potential was set to -100 mV vs. SCE (anodic of the open circuit potential for every alloy studied) to etch the film, liberating Ni^{+2} and Fe^{+2} from the film surface and generating current at the disk. The volumetric etch rate of the NiFe alloy was then calculated from the measured disk current during etching, based on the molar volume of the deposit and Faraday's law. In addition to -100 mV, NiFe etching rates at potentials of -150, -200, -250, -300 and -350 mV vs. SCE were investigated as well. Two different acid solutions were studied; one chloride-based and another acetic acid-based. The chloride-based etching solution was composed of 0.2 M HCl and 0.5 M NaCl. The acetic acid solution was composed of 10% (by weight) glacial acetic acid in deionized water. The reasons for choosing these particular solutions for the controlled etch study are discussed later.

In-Situ Etching of Sacrificial Material

Using the same potentiostat, rotator and plating bath described in the RRDE study, NiFe alloys with spatially periodic composition were plated onto the removable disk of a copper rotating disk electrode (RDE). Films 115 μm thick (on average) were plated galvanostatically using an applied current density of -40 mA/cm^2. During deposition, the disk rotation rate was varied in a square wave at 13 minute intervals in the sequence 100 / 400 / 100 / 900 / 100 / 1600 / 100 / 2500 / 100 / 3600 / 100 rpm, creating a deposit with 11 distinct layers. After plating, the RDE was rinsed with deionized water and then immersed in a standard Watt's plating bath [27] from which a 200 μm thick nickel layer was electroplated over the NiFe film.

The plated copper disk electrode was removed from the RDE housing and cut in cross section using a diamond wafering blade. The planar face of the cross sectioned sample was then polished to a mirror finish using 1.0 μm diamond paste and studied using SEM and EDS techniques described above. The cross section sample was then contacted and held at -150 mV vs. SCE in the 10% acetic acid solution for 120 minutes. The sample was removed from the etch solution and lapped to reveal the extent of etching

into each compositional layer. The polished sample was cleaned in an ultrasonic bath with deionized water previous to final analysis using SEM and EDS.

Results and Discussion

Figure 6.1 is a pair of SEM micrographs which show a NiFe microgear electrodeposited at -60 mA/cm^2 under well controlled, modulated mass transfer conditions. As discussed previously, deposition under these mass transfer conditions leads to a deposit with alternating layers of high and low iron composition. After plating, the gear was immersed in the glacial acetic acid etching bath at 40° C for 12 hours. The layered structure of the microgear is revealed by the selective etching process. The thick, bright layers are nickel-rich strata and the relatively thin, darker bands are formally iron-rich strata which were dissolved in the acid bath. The preferential etching of the iron-rich layers reveals the thickness uniformity of the nickel-rich strata and the sharp boundaries between the thick layers and the sacrificial zones illustrate the high selectivity of this technique. This is most easily seen in Figure 6.1 (B). Only moderate etching (in the form of pitting) is seen in areas other than the thin sacrificial layers.

Figure 6.2 is an SEM micrograph (A) and EDS composition map (B) of a single microgear tooth that has been lapped and polished in cross section. Approximately 20 μm of material has been removed from the tip of the gear tooth during the lapping process. On both sides of the tooth, the extent of acidic etch penetration is evident. On the left side of the tooth, all 10 sacrificial layers have been dissolved to some extent while on the right side it appears that only the top two or three layers were etched. The interlayer composition variation within the microgear is illustrated in Figure 6.2 (B). Here, lighter shading represents areas with relatively higher iron content while darker shading represents iron-deficient regions. The layered structure is evident in the composition map, with a series of light bands running horizontally across the tooth throughout its vertical dimension. Quantitative analysis indicates that the thicker, iron-deficient layers exhibit a composition of approximately $Ni_{75}Fe_{25}$ while the layers susceptible to acidic dissolution contain significantly more iron. On average, the composition of these sacrificial layers is $Ni_{35}Fe_{65}$.

A rough estimate of the etching rate in the glacial acetic acid can be made by measuring the penetration of the etch front in the sacrificial layers shown in Fig. 6.2 (A).
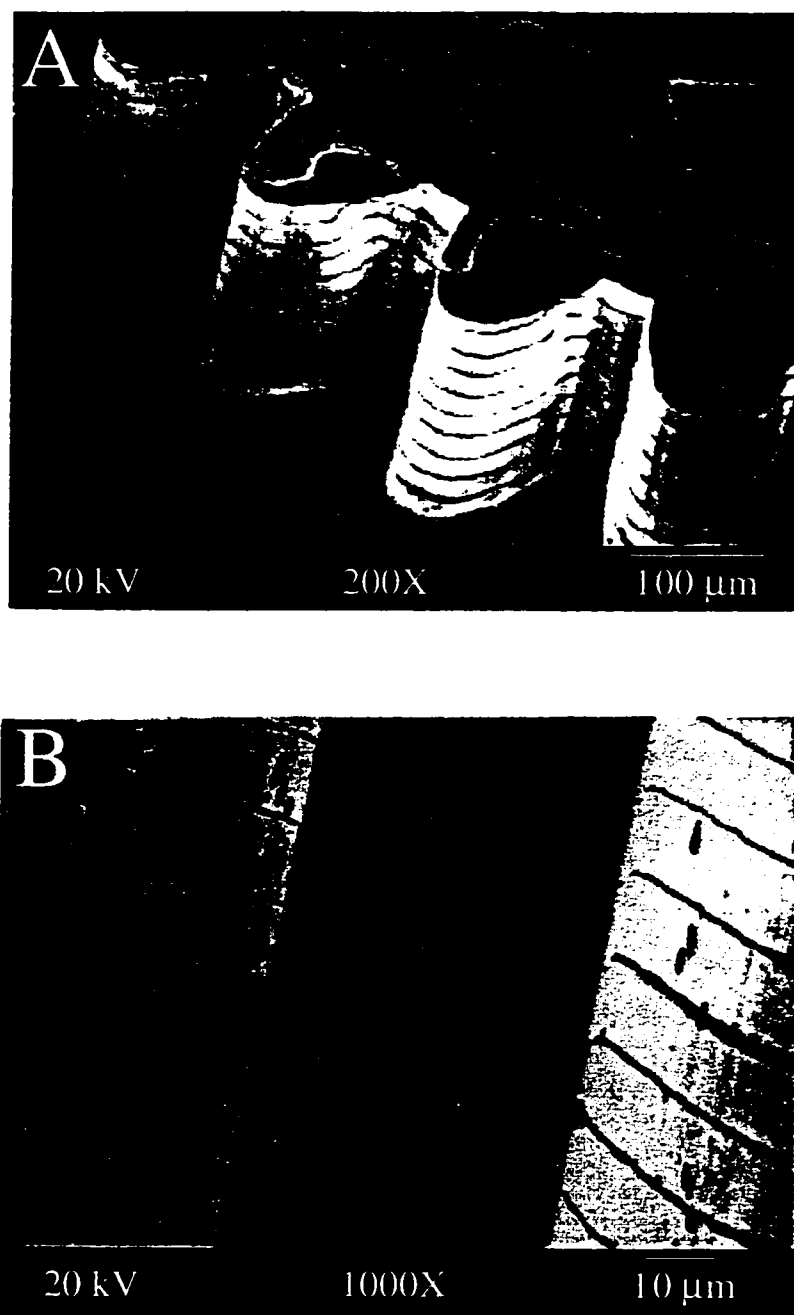
Figure 6.1. Scanning electron micrographs of an electrodeposited NiFe microgear. *In-situ* sacrificial layers are created during plating and revealed using a selective acidic etching technique. Light bands are 17 μm thick iron-deficient layers and dark bands are 3 μm thick iron-rich sacrificial layers.
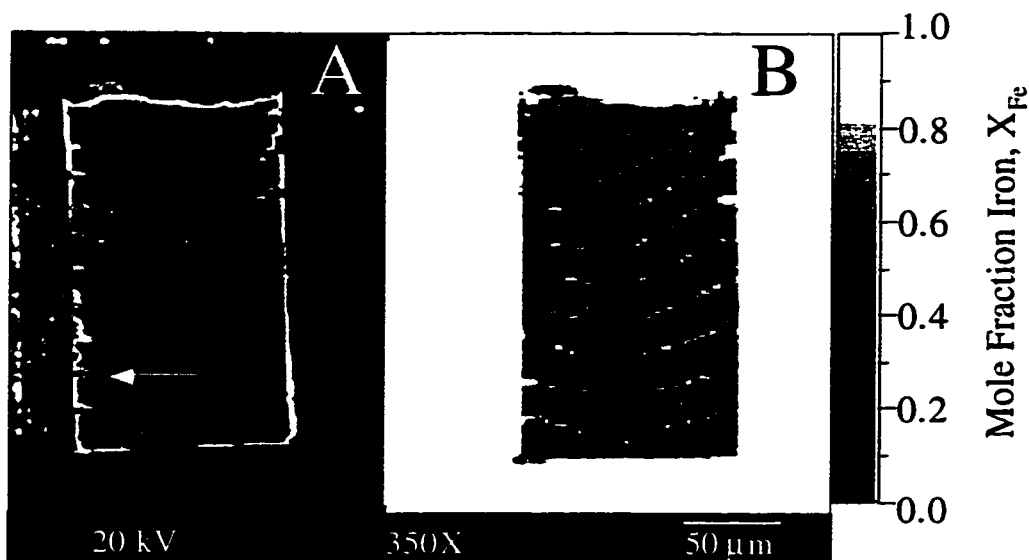
Figure 6.2. Scanning electron micrograph (A) and corresponding composition map (B) of a single microgear tooth after lapping and polishing in cross section. The penetration of the etch front in one sacrificial layer is illustrated by the arrow.

For example, the etch front at the arrow has penetrated a distance of approximately 9 μm into the gear tooth. On the left side of the tooth, the average penetration depth is about 7 μm. To remove the surface area dependence of a volumetric etch rate, a linear etching rate is calculated based on the penetration depth. For the tooth in Fig. 6.2, this rate is approximately 0.5 μm/hr. The minimal etching of the right side of the tooth suggests that the overall dissolution rate of sacrificial material may be even lower than this estimated value and is not necessarily uniform over the entire microgear. Despite the good selectivity displayed in Figs. 6.1 and 6.2, the low etch rate of glacial acetic acid makes it impractical for removal of sacrificial material in most micromachining applications.

To better understand general etching characteristics and to improve sacrificial etch rates, potentiostatic etching studies of NiFe films were performed using chloride-based and acetic acid-based electrolytes. Chloride-based solutions have been used previously to etch NiFe electrodeposits (illustrated in Chapters 2 and 5 and also in [12] and [44]). In

those studies the chloride bath was shown to be a reliable electrolyte for potential controlled oxidation of NiFe and thus, was chosen for investigation in the present study. Due to the high selectivity of glacial acetic acid in etching microgears, an acetic acid formulation was investigated as well. Preliminary studies with the acetic acid bath focused on determination of an optimum solution concentration for use during the potential controlled etch study.

Figure 6.3 illustrates the current-potential relationships for electrodeposited $Ni_{35}Fe_{65}$ films in glacial acetic acid as well as in 50% (by mass) and 10% acetic acid solutions. In Fig. 6.3, the etch rate of the film is proportional to current, for those currents greater than zero. Curve (a) is the cyclic voltammogram in glacial acetic acid, curve (b) in 50% acetic acid and curve (c) in 10% acetic acid. Potential dependent etching is not observed using the glacial acetic acid bath. In fact, negligible etching is achieved. The curve is a flat line at nearly zero current over the entire range of potentials investigated. Diluting the acid solution to 50%, however, allows a measure of control over the etch rates. As shown in curve (b), the current varies from 0 to 1.5 mA/cm^2 over a 1200 mV potential range. Further dilution to 10% gives even more flexibility in rate control, as illustrated in curve (c). Over a potential range of nearly 1400 mV, the current varies from 0 to 3.5 mA/cm^2 using the 10% bath. While the 50% solution exhibits characteristics suitable for the controlled etching study, the primary goal here is to maximize the etch rate of sacrificial material. For this reason, the 10% solution was chosen for further study in the potential controlled etching investigation.

The etching rate dependence on applied potential and NiFe alloy composition is illustrated in Fig. 6.4 for both the 10% acetic acid solution (A) and the chloride solution (B). In both electrolytes, higher etching rates are achieved as the potential is increased. Alloys with relatively high iron content oxidize faster as well. Significant differences between the baths are apparent. The chloride bath is more aggressive than the 10% acetic acid solution. For a given alloy composition and applied potential, the etch rates are an order of magnitude higher when using the chloride bath. The 10% acetic acid bath, however, is more sensitive to alloy composition, a desirable trait for selective etching. For example, at -150 mV vs. SCE, the etch rate of $Ni_{35}Fe_{65}$ is nearly four times that of $Ni_{80}Fe_{20}$. The same conditions in the chloride bath lead to negligible differences in oxidation rates between these two alloys. Due to the higher compositional selectivity of
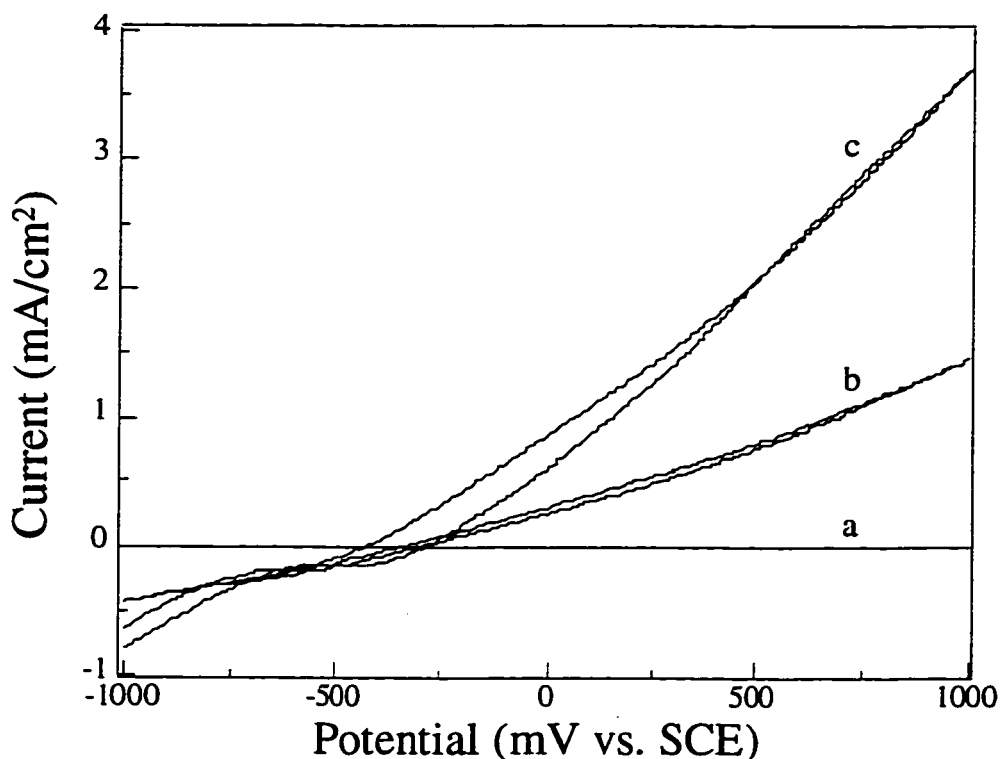
Figure 6.3. Cyclic voltammogram for $Ni_{35}Fe_{65}$ in (a) glacial acetic acid, (b) 50% acetic acid and (c) 10% acetic acid.

the acetic acid bath, this electrolyte was used to study preferential oxidation of *in-situ* sacrificial layers electroplated onto the rotating disk electrode.

Figure 6.5 is a cross section EDS composition map (A) and a line profile (B) of a layered NiFe alloy electroplated onto the RDE. In (A), light bands represent layers with relatively high iron content and the darker bands are iron-deficient layers. The map illustrates the well-defined compositional strata throughout the depth of the deposit resulting from plating at different disk rotation rates. Each layer is approximately 10 μm thick. The black band at the top of (A) is the electroplated nickel overlayer and the copper substrate lies in the area of the figure obscured by the data bar.
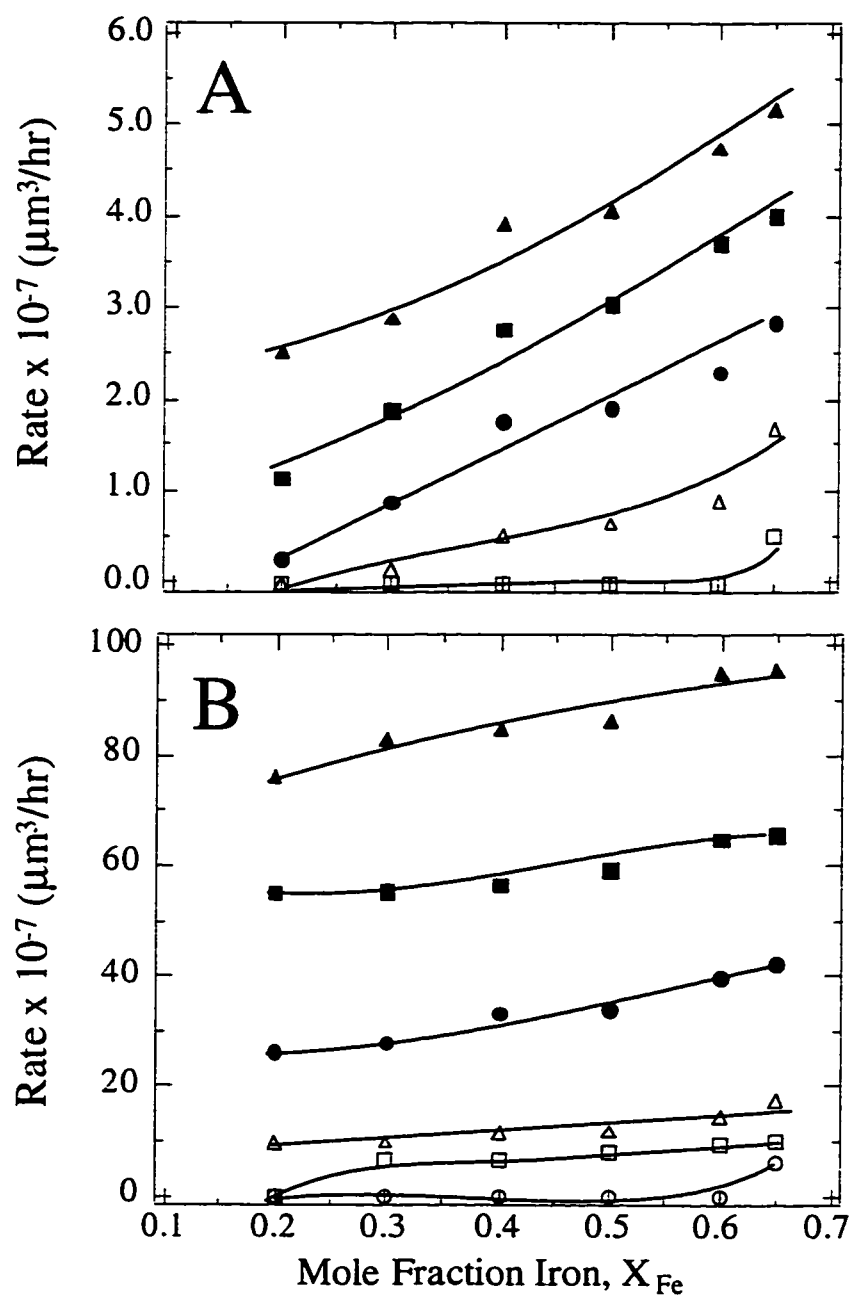
Figure 6.4. Etching rate dependence on applied potential and NiFe alloy composition for the 10% acetic acid bath (A) and the chloride-based electrolyte (B) for potentials of -100 (▲), -150 (■), -200 (●), -250 (△), -300 (□) and -350 (o) mV vs. SCE.
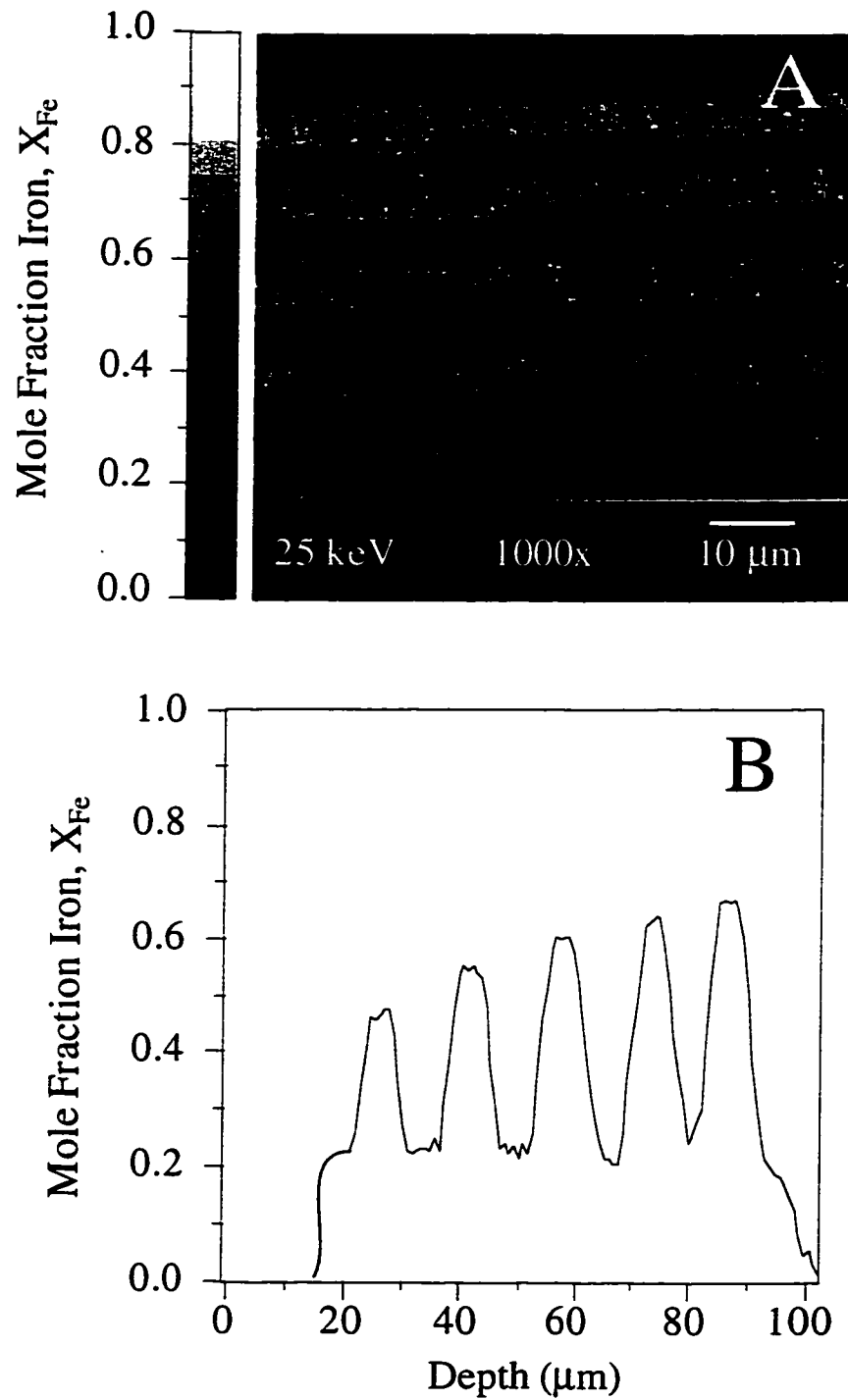
Figure 6.5. Cross section composition map (A) and profile (B) of a layered NiFe alloy. In (A), light bands are iron-rich sacrificial layers sandwiched between iron-deficient layers. The profile in (B) is from bottom to top across the layers shown in (A).

There are 11 total layers in the film with each of the five iron-rich sacrificial layers (lighter shading) sandwiched by two iron-deficient layers. The line profile shown in (B) gives another perspective of the film cross section and allows better quantification of the individual layer compositions. The depth profile starts about 15 μm into the copper substrate and increasing depth is in the growth direction of the film (*i.e.* from bottom to top in (A)). The progression of increasing iron composition in alternating layers is clearly illustrated. The presence of the iron-deficient layers is evident as well. Each iron-deficient layer has a composition of approximately 20 mol% iron. The six layers of high-iron exhibit compositions of (in order, from the substrate) 48, 55, 62, 65 and 68 mol% iron. Based on the results from the potential controlled etching study, the six layers should dissolve at different rates, with the layer of highest iron composition etching fastest. The iron-deficient layers should etch at the lowest rates of all.

Figure 6.6 is an SEM micrograph of the layered NiFe film after 120 minutes at -150 mV vs. SCE in the 10% acetic acid etching solution. The penetration depth of the etch front is revealed by lapping the etched sample. In Fig. 6.6, the copper substrate, the nickel overlayer and the originally polished cross section face are labeled to aid in discussion. The potential controlled etching procedure results in preferential removal of material based on the individual layer compositions. The top-most iron-rich layer was highly susceptible to the etching while the iron-deficient layers remained entirely intact. Using the results shown in Fig. 6.5, we can correlate the measured linear etch rate of each layer to its corresponding composition.

As predicted by Fig. 6.4, we find that the etch rate of the individual layers is directly related to the iron content in each. For example, the composition of the top layer was 68 mol% iron and the average linear etch rate of this layer was approximately 80 μm/hr. The bottom etched layer had a composition of 55 mol% iron and was etched at an average rate of approximately 20 μm/hr. Conversely, layers with compositions of 20 and 48 mol% iron were not etched to a significant extent. The high sensitivity to composition results in well-defined layers with sharp edges and relatively smooth surfaces. Figure 6.7 shows a pair of SEM micrographs that illustrate in higher magnification the morphological characteristics of the remaining layers. A small number of pits are evident on the faces of the remaining $Ni_{80}Fe_{20}$ layers, but in general the layers were quite resistant to etching. The top and bottom surfaces of the layers are relatively smooth as
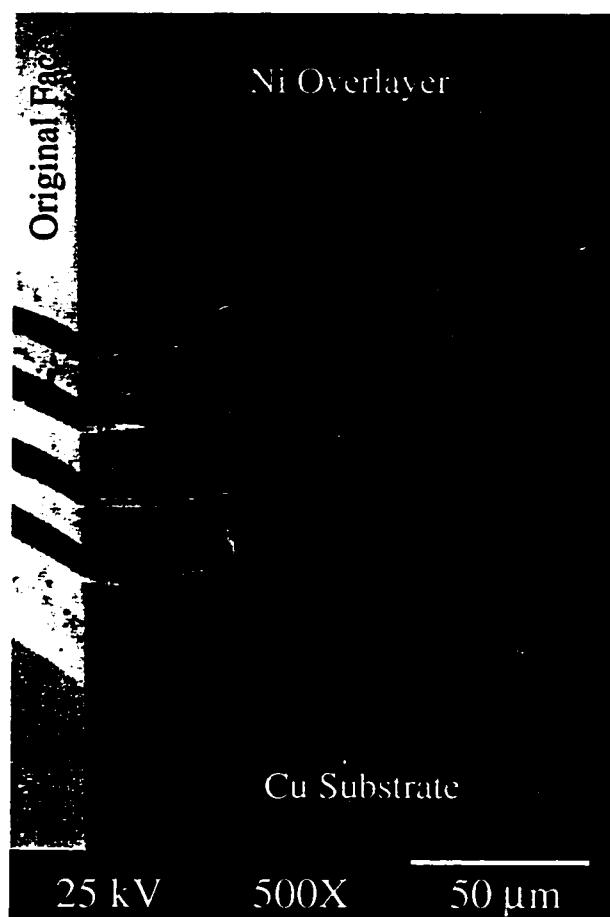
Figure 6.6. Scanning electron micrograph of a layered NiFe alloy after selective dissolution of sacrificial layers using potential control. The sample has been lapped in a plane normal to the original polished face in a direction parallel to the layers.

well, further illustrating that complete removal of the iron-rich regions can be accomplished with little damage to remaining layers.

While the general etching trends mirror the results shown in Fig. 6.4, the results from Figs. 6.5 and 6.6 illustrate interesting differences between the rates determined in the RRDE studies and the rates measured on the layered film. Table 6.1 summarizes the etching rates determined in both the RRDE study and the *in-situ* investigation. As
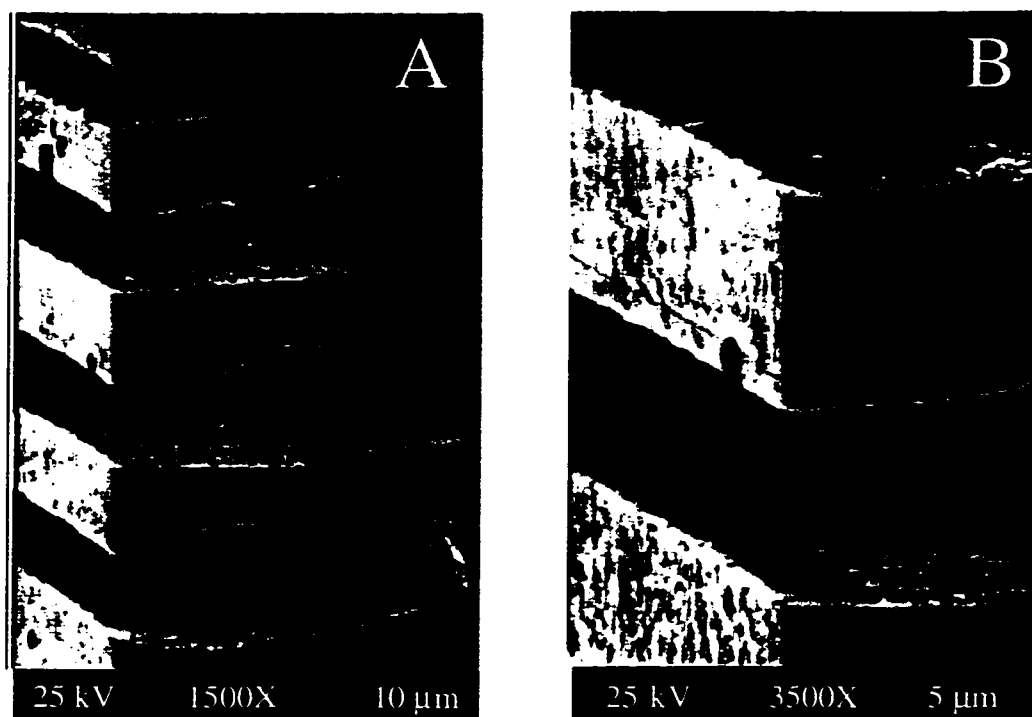
Figure 6.7. Scanning electron micrograph of a layered NiFe alloy after selective dissolution of sacrificial layers using potential control.

illustrated in the table, the etching rates observed *in-situ* are on average 17.5 times those measured using the RRDE under identical polarization conditions. In addition, the etching selectivity is also much higher. For example, the $Ni_{35}Fe_{65}$ layer etched nearly three times faster than the $Ni_{45}Fe_{55}$ layer *in-situ*. On the RRDE, however, the difference in etch rates between the same two films is approximately 1.3 times. These results suggest that local oxidation processes (*e.g.* galvanic coupling) occurring during *in-situ* etching have a significant effect on both the selectivity and rates of etching. In the present study, local oxidation mechanisms increased the selectivity and rate of etching beyond expected levels. For optimum control using this technique, these "corrosion-like" processes must be prevented.

The ability to preferentially remove volumes of iron-rich NiFe deposits opens the possibility for development of alternative micromachining techniques that could be utilized in a variety of applications. For example, in manufacturing of NiFe MEMS

Table 6.1. Linear etch rates of NiFe alloys in 10% acetic acid at -150 mV vs. SCE for RRDE and *in-situ* investigations. The magnitude of *in-situ* etching enhancement for a given alloy composition is determined here by the ratio of *in-situ* to RRDE etching rates.

	Rate (μm/hr)		
X_{Fe}	RRDE	*in-situ*	Enhancement
0.20	0.6	0	0
0.48	1.5	0	0
0.55	2.0	22.3	11.2
0.62	2.2	37.2	16.9
0.65	2.3	56.4	24.5
0.68	*	79.8	undetermined

* - No data available

components using a LIGA or LIGA-like process, it is common to electrodeposit parts through a molded pattern onto a silicon wafer covered with a sputter-coated copper conductive film. After deposition and removal of the mold, the individual MEMS components are released from the wafer by a wet chemical etch process that preferentially attacks the copper layer. For microgears plated in this study the release time for a wafer containing 85 parts using conventional copper etching was on the order of 12 hours. If the plating base was not copper, but rather a high-iron content NiFe alloy, potential controlled etching could be used and the release time would be significantly decreased. In this case, the plating base could be deposited *in-situ*; essentially a thin sacrificial layer could be plated directly through the mold with continued deposition of the desired structure above it. Application of an appropriate potential (depending on the composition of the sacrificial layer and that of the remaining deposit) would preferentially etch the base layer while leaving the final part unaltered. This technique could be applied to many NiFe through-mold plating processes, especially those in which the final part is a low-iron alloy such as Permalloy ($Ni_{80}Fe_{20}$).

A more complex application is the use of sacrificial layers to fabricate 3-D structures in a through-mold plating process. Here, the final part is a 3-dimensional

component that results from preferential removal of sacrificial material deposited *in-situ*. Figure 6.8 shows a microgear that has been split into top and bottom sections by potential controlled removal of the iron-rich sacrificial layer. As was illustrated in Figs. 6.6 and 6.7, a very smooth surface exists at the interface between the (now dissolved) sacrificial layer and the remaining halves of the part. The figure shows that the fabrication and preferential removal of *in-situ* sacrificial layers can be applied across relatively large length scales. This particular example also illustrates one caveat of the technique. Note that the remaining parts were not split in half along a plane. Rather, the split occurred along the surface of the part as it existed when the sacrificial layer was added. The bottom half of the gear (standing on edge in Fig. 6.8) illustrates the time-integrated current distribution at the point in the process history in which the sacrificial layer was added. In this example, the gear teeth were nearly completely formed when the layer was created, resulting in the "bottle-cap" structure shown in Fig. 6.8. Thus, fabrication of 3-
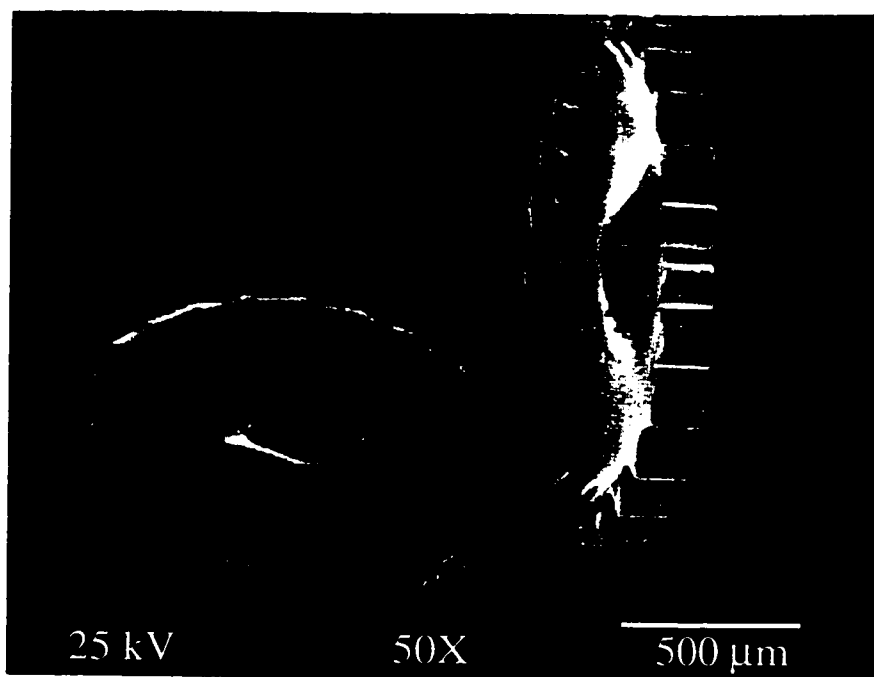
Figure 6.8. Scanning electron micrograph of an electrodeposited NiFe microgear after complete removal of an iron-rich sacrificial layer using potential control.

dimensional structures with predictable surface topography relies not only on precise control of electrolyte mixing, but also on understanding of the current distribution within the molded feature.

Conclusions

Galvanostatic electrodeposition of NiFe alloys with well defined regions of high and low-iron composition is possible through controlled modulation of mass transfer conditions. Using this technique, multilayer structures can be created during deposition of NiFe films and molded microstructures. Layers with high iron content become sacrificial material and are dissolved using a slow concentrated acidic etch technique or by etching in dilute acid under potential control. The concentrated acid etch is highly selective in preferential dissolution of high-iron volumes, but the etching rate of approximately 0.5 μm/hr may not be practical for all micromachining applications. Accelerated removal of sacrificial material is achieved through potential controlled etching. Rates approaching 80 μm/hr are attained for removal of sacrificial layers using potential control. Selectivity of this technique is shown to be at least as good as that when using the concentrated acid etch. The concept of *in-situ* fabrication and dissolution of sacrificial material illustrated here can be applied in a number of through-mold plating processes including deposition of sacrificial release layers and/or deposition of molded 3-dimensional microstructures. As discussed in Chapter 7, future work should focus on these as well as other maskless plating applications.

CHAPTER 7

Conclusions and Recommendations

Conclusions

Presented are studies which explore a number of facets related to electrodeposition of NiFe alloys. Systematic investigations using the rotating ring-disk electrode (RRDE) are used to thoroughly characterize relationships between processing conditions and compositional structure in electrodeposited NiFe thin films. These results form the foundation for subsequent studies of through-mold electrodeposition of NiFe microstructures using a newly designed plating device. Taken together, the studies described here 1) Describe the development and optimization of a plating process suitable for electrodeposition of NiFe microstructures with uniform composition and 2) Illustrate the fabrication of 3-dimensional NiFe microstructures through deposition and subsequent removal of *in-situ* sacrificial layers. Specific research accomplishments of this investigation include the following :

1. Using a systematic approach, we have developed and characterized the performance of a NiFe plating bath that is both versatile and robust. The thorough bath characterization outlines specific formulations and operating guidelines for deposition of alloys with a wide range of compositions. Results from the study are presented in a general form that can easily be applied to electrodeposition of NiFe alloys in any plating device with well understood current distribution and mass transfer characteristics. The bath can be used to deposit NiFe thin films and microstructures with controlled and predictable compositions.

2. An electroplating device suitable for electrodeposition of 3-dimensional microstructures was designed and fabricated. Performance characteristics of the device in through-mold electrodeposition were explored at the workpiece and pattern length scales. Results illustrate that the device delivers controlled and predictable average mass transfer rates at the workpiece length scale, but pattern scale mass transfer variations result from an imperfect porous frit injector.

3. Feature scale composition non-uniformities are minimized by electrodepositing NiFe microstructures from a plating bath relatively insensitive to electrolyte mixing variations.

Controlling deposit composition on this length scale enabled development of a high throughput, high yield NiFe microstructure plating process.

4. Flow-induced composition modulated NiFe alloys (CMAs) are formed over a range of current densities when the convective mass transfer rate is subjected to sub-Hertz oscillations. Potentiostatic stripping voltammetry, when combined with FFT analysis, is a useful technique for compositional characterization of NiFe CMAs electrodeposited using the RRDE. Results show that CMA wavelength scales as the inverse of the flow oscillation frequency and composition modulation amplitude is strongly affected by variations in both electrolyte flow oscillations frequency and amplitude. NiFe alloys with compositional layers ranging in thickness from 3.5 nm to 10 μm have been plated. Composition variation approaching 50 mol% is achieved between successive layers.

5. The concept of flow-induced CMAs is applied to through-mold electrodeposition of NiFe microstructures. Using a pulsed electrolyte agitation technique, iron-rich sacrificial layers are formed in-situ during deposition. Sacrificial layers are removed using both wet chemical etching and potential-enhanced etching processes. Etch rates of sacrificial material ranging from 0.5 to 80 μm/hr are measured with negligible effect on remaining non-sacrificial layers.

Recommendations

1. The characterization of NiFe thin films and microstructures in this study focused primarily on measuring either average or local deposit composition. Results from this work might have a greater impact on those working in MEMS fabrication if the properties of these deposits were also investigated. For example, Permalloy is widely used as a magnetic actuator in many micromachining applications [5-8]. Physical properties of the material including internal stress, magnetostriction, saturation magnetization and magnetic permeability may affect the performance of the device and should be considered in design and fabrication. Since these properties are influenced in part by deposit composition [2, 9, 11], relationships between processing variables, composition and alloy properties may prove beneficial.

2. As discussed in Chapter 3, the porous glass frit injector of the UIC used in this study was imperfect and contributed to non-uniformities on the pattern length scale.

Subsequent generations of the device should incorporate a re-engineered porous frit that ensures uniform axial electrolyte injection. At this time, it appears as though recently developed micromachining technologies may be suitable for fabrication of a high performance porous frit. For example, it may be possible to pattern a thick (> 1 mm) sheet of PMMA with high aspect ratio and spatially uniform micropores using x-ray lithography (as in the LIGA process) [26]. The PMMA sheet could then be cut into a disk and incorporated into an injector housing. Another possibility is the bulk micromachining of a silicon wafer. In theory, one could use a dry etch technique such as deep reactive ion etching to create spatially uniform microchannels with vertical sidewalls throughout the depth of a silicon wafer [26]. Using either technique, an injector with *uniform* pores as small as 10 μm in diameter could be fabricated, likely resulting in greatly improved device performance.

3. It would be of interest to expand on the results presented in Chapter 5 to include plating of NiFe CMAs by pulsed-potential (or pulsed-current) or by a combination of pulsed-potential and flow-induced techniques. Since nucleation and growth mechanisms are potential dependent, it is possible that NiFe CMAs deposited using these methods would exhibit different physical properties than flow-induced alloys with the same composition modulation wavelength and amplitude. Pulse plating of other iron-group CMAs such as NiCu has been demonstrated [70, 71, 79, 80], but plating NiFe CMAs with this technique has not been explored.

4. Further investigation regarding *in-situ* fabrication and removal of iron-rich sacrificial layers in electrodeposited NiFe microstructures is suggested. Specifically, an experimental design which minimizes galvanic coupling and other "corrosion-like" processes is needed to establish more reliable quantification of potential enhanced *in-situ* etching. An investigation in which only one sacrificial layer was plated in a "sandwich" and potentiostatically etched would be a good start. This would at least minimize coupling between the NiFe layers of different compositions. In addition, the understanding of the technique could be expanded through investigation of possible mass transfer limitations in etching. The sacrificial layers plated in Chapter 6 were all 10 μm thick and mass transfer processes did not affect the etch rate. For thinner layers, however, diffusion limitations may negate any differences in etching rate due to

compositional variation. A study in which sacrificial layers of smaller dimensions are plated and etched may provide insight into this issue.

5. The results presented here detailing the NiFe bath characterization, CMA plating, UIC operation and formation of *in-situ* sacrificial layers form the basis of a potentially high-impact 3-dimensional microstructure fabrication technique; maskless, free-form electrodeposition of NiFe microstructures. In this dissertation, it was shown that the relationships between composition, current density and mass transfer are well understood for the family of plating baths described. We have also demonstrated the ability to control the composition at the sub-micron scale through manipulation of process variables (in this case we used flow modulation, although results in Chapter 2 suggest that the same can be done with potential control). Further, we have illustrated that preferential removal of selective alloy compositions is possible through potential control. Each of these processes has been described and applied in related, but separate studies.

Integration of these ideas into a single processing tool would enable simultaneous deposition and etching through control of potential across an array of substrate locations. Such a tool can be fabricated based on the UIC. The device would need a micromachined injector in which each flow channel is associated with a micro counter electrode. The injector would then act as a microelectrode array in which the potential of each electrode element could be independently controlled, dictating which areas of the substrate are plated and which are not. With such a tool, a 3-dimensional structure could be "built up" onto a conductive substrate by simultaneous plating and etching across the substrate on lateral length scales dictated by the spacing of individual electrode elements - eliminating the need for costly masks and molded patterns. Fabrication of the device with integrated electronics and necessary algorithms for potential control actions during free-form deposition, however, make this project challenging and truly interdisciplinary.

References

1. Gobet, J., Cardot, F., Bergqvist, J. and Rudolf, F., *J. Micromech. Microeng.*, **3**, 123 (1993).

2. Andricacos, P. C. and Romankiw, L. T. In *Advances in Electrochemical Science and Engineering*; H. Gerischer and C. W. Tobias, Ed.; VCH: New York, 1994; Vol. 3; pp 227.

3. Löchel, B., Maciossek, A., Quenzer, H.-J. and Wagner, B., *J. Electrochem. Soc.*, **143**, 237 (1996).

4. Romankiw, L. T., *Electrochim. Acta*, **42**, 2985 (1997).

5. Judy, J. W., Muller, R. S. and Zappe, H. H., *J. Microelectromech. Sys.*, **4**, 162 (1995).

6. Ahn, C. H. and Allen, M. G., in *Proceedings of the Fourth International Symposium on Magnetic Materials, Processes, and Devices. Applications to Storage and Microelectromechanical Systems (MEMS)*, **95-18**, 411, The Electrochemical Society, Pennington, NJ, (1995).

7. Sadler, D., Zhang, W., Ahn, C. H., Kim, H. J. and Han, S. H., *IEEE Trans. Mag.*, **33**, 3319 (1997).

8. Liakopoulos, T. M., Xu, M. and Ahn, C. H., in *Technical Digest : 1998 Solid-State Sensor and Actuator Workshop*, 19, Transducers Research Foundation, (1998).

9. Cheung, C., Djuanda, F., Erb, U. and Palumbo, G., *Nanostruct. Mater.*, **5**, 513 (1995).

10. Frankel, G. S. In *Corrosion Mechanisms in Theory and Practice*; P. Marcus and J. Oudar, Ed.; Marcel Dekker, Inc.: New York, 1995.

11. Schumann, F. O., Wu, S. Z., Mankey, G. J. and Willis, R. F., *J. Appl. Phys.*, **79**, 5635 (1996).

12. Andricacos, P. C., Arana, C., Tabib, J., Dukovic, J. and Romankiw, L. T., *J. Electrochem. Soc.*, **136**, 1336 (1989).

13. Grimmett, D. L., Schwartz, M. and Nobe, K., *J. Electrochem. Soc.*, **140**, 973 (1993).

14. Küpper, M. and Schultze, J. W., *Electrochim. Acta*, **42**, 3023 (1997).

15. DeBecker, B. and West, A. C., *J. Electrochem. Soc.*, **143**, 486 (1996).

16. Bade, K., Leyendecker, K., Thommes, A. and Bacher, W., in *Proceedings of the Fourth International Symposium on Magnetic Materials, Processes, and Devices. Applications to Storage and Microelectromechanical Systems (MEMS)*, **95-18**, 697, The Electrochemical Society, Pennington, NJ, (1995).

17. Mehdizadeh, S., Dukovic, J. O., Andricacos, P. C., Romankiw, L. T. and Cheh, H. Y., *J. Electrochem. Soc.*, **140**, 3497 (1993).

18. Mehdizadeh, S., Dukovic, J. O., Andricacos, P. C., Romankiw, L. T. and Cheh, H. Y., *J. Electrochem. Soc.*, **139**, 78 (1992).

19. West, A. C., Matlosz, M. and Landolt, D., *J. Electrochem. Soc.*, **138**, 728 (1991).

20. Dukovic, J. O., *IBM J. Res. Develop.*, **34**, 693 (1990).

21. Newman, J., *Electrochemical Systems*; Prentice-Hall: Englewood Cliffs, NJ, 1973.

22. Matlosz, M., *J. Electrochem. Soc.*, **140**, 2272 (1993).

23. Hessami, S. and Tobias, C. W., *J. Electrochem. Soc.*, **136**, 3611 (1989).

24. Dahms, H. and Croll, I. M., *J. Electrochem. Soc.*, **112**, 771 (1965).

25. Maciossek, A., Löchel, B., Quenzer, H.-J., Wagner, B., Schulze, S. and Noetzel, J., *Microelectron. Eng.*, **27**, 503 (1995).

26. Madou, M., *Fundamentals of Microfabrication*; CRC Press: Boca Raton, 1997.

27. Yahalom, J. and Zadok, O., *J. Mater. Sci.*, **22**, 499 (1987).

28. Cohen, U., Koch, F. B. and Sard, R., *J. Electrochem. Soc.*, **130**, 1987 (1983).

29. Lashmore, D. S. and Dariel, M. P., *J. Electrochem. Soc.*, **135**, 1218 (1988).

30. Baral, D., Ketterson, J. B. and Hilliard, J. E., *J. Appl. Phys.*, **57**, 1076 (1985).

31. Tang, W., Gerhards, C., Heise, J. and Zabel, H., *J. Appl. Phys.*, **80**, 2327 (1996).

32. Thaler, B. J., Ketterson, J. B. and Hilliard, J. E., *Phys. Rev. Lett.*, **41**, 336 (1978).

33. Nee, C. C., Kim, W. and Weil, R., *J. Electrochem. Soc.*, **135**, 1100 (1988).

34. Chassaing, E., Nallet, P., Walls, M. and Hytch, M. J., in *Proceedings of the Fourth International Symposium on Magnetic Materials, Processes, and Devices. Applications to Storage and Microelectromechanical Systems (MEMS)*, *95-18*, The Electrochemical Society, Pennington, NJ, (1995).

35. Chassaing, E., Nallet, P. and Trichet, M. F., *J. Electrochem. Soc.*, **143**, L98 (1996).

36. Hirano, T. and Fan, L.-S., in *SPIE Proceedings : Micromachining and Microfabrication Process Technology II*, *2879*, 252, SPIE, (1996).

37. Grande, W. C. and Talbot, J. B., *J. Electrochem. Soc.*, **140**, 669 (1993).

38. Grande, W. C. and Talbot, J. B., *J. Electrochem. Soc.*, **140**, 675 (1993).

39. Harris, T. M. and St. Clair, J., *J. Electrochem. Soc.*, **143**, 3918 (1996).

40. Harris, T. M., St. Clair, J. and Huynh, T., in *Proceedings of the Fourth International Symposium on Magnetic Materials, Processes, and Devices. Applications to Storage and Microelectromechanical Systems (MEMS)*, *95-18*, 717, The Electrochemical Society, Pennington, NJ, (1995).

41. Grimmett, D. L., Schwartz, M. and Nobe, K., *J. Electrochem. Soc.*, **137**, 3414 (1990).

42. Yin, K. M., Wei, J. H., Fu, J. R., Popov, B. N., Popova, S. N. and White, R. E., *J. Appl. Electrochem.*, **25**, 543 (1995).

43. Leith, S. D., Schwartz, D. T. and Deng, K., in *Technical Digest : 1998 Solid-State Sensor and Actuator Workshop*, 245, Transducers Research Foundation, (1998).

44. Andricacos, P. C., Tabib, J. and Romankiw, L. T., *J. Electrochem. Soc.*, **135**, 1172 (1988).

45. Bard, A. J. and Faulkner, L. R., *Electrochemical Methods*; John Wiley and Sons: New York, 1980.

46. Medina, J. A., Sexton, D. L. and Schwartz, D. T., *J. Electrochem. Soc.*, **142**, 457 (1995).

47. Grimmett, D. L., Schwartz, M. and Nobe, K., *Plat. and Surf. Fin.*, **75**, 94 (1988).

48. Safranek, W. H., *The Properties of Electrodeposited Metals and Alloys*; American Elsevier: New York, 1974.

49. Lorenz, H., Despont, M., Fahrni, N., Brugger, J., Vettiger, P. and Renaud, P., *Sensors and Actuators A*, **64**, 33 (1998).

50. Borner, M. W., Kohl, M., Pantenburg, F. L., Bacher, W., Hein, H. and Schomburg, W. K., *Microelectron. Eng.*, **30**, 505 (1996).

51. Becker, E. W., Ehrfeld, W., Hagmann, P., Maner, A. and Münchmeyer, D., *Microelec. Eng.*, **4**, 35 (1986).

52. Medina, J. A. and Schwartz, D. T., *J. Electrochem. Soc.*, **144**, 155 (1997).

53. Medina, J. A. and Schwartz, D. T., *Electrochim. Acta*, **42**, 2679 (1997).

54. Medina, J. A. and Schwartz, D. T., *J. Electrochem. Soc.*, **142**, 451 (1995).

55. Goldstein, J. I., Newbury, D. E., Echlin, P., Joy, D. C., Romig, J., A.D., Lyman, C. E., Fiori, C. and Lifshin, E., *Scanning Electron Microscopy and X-Ray Microanalysis*; 2nd ed.; Plenum Press: New York, 1992.

56. Guckel, H., Christenson, T. R., Skrobis, K. J., Denton, D. D., Choi, B., Lovell, F. G., Lee, J. W., Bajkar, S. S. and Chapman, T. W., in *Technical Digest : 1990 Solid-State Sensor and Actuator Workshop*, 119, IEEE, (1990).

57. Löchel, B. and Maciossek, A., *J. Electrochem. Soc.*, **143**, 3343 (1996).

58. Löchel, B., Maciossek, A., Quenzer, H.-J., Wagner, B. and Engelmann, G., *Sensors and Actuators A*, **46-47**, 98 (1995).

59. Bonivert, W. D., Hruby, J. M., Hachman, J. T., Malek, C. K., Jackson, K. H., Brennen, R. A., Hecht, M. H. and Wiberg, D., in *Proceedings of the Fourth*

*International Symposium on Magnetic Materials, Processes, and Devices.
Applications to Storage and Microelectromechanical Systems (MEMS), 95-18,*
The Electrochemical Society, Pennington, NJ, (1995).

60. Thommes, A., Stark, W., Leyendecker, K., Bacher, W., Liebscher, H. and Jakob, C.,
in *Proceedings of the Third International Symposium on Magnetic Materials,
Processes and Devices, 94-6*, 89, The Electrochemical Society, (1993).

61. Löchel, B., Maciossek, A., Rothe, M. and Windbracke, W., *Sensors and Actuators A,*
54, 663 (1996).

62. Miyajima, H. and Mehregany, M., *J. Microelectromech. Sys.,* **4**, 220 (1995).

63. Guckel, H., Earles, T. and Klein, J., in *Proceedings of the Fourth International
Symposium on Magnetic Materials, Processes, and Devices. Applications to
Storage and Microelectromechanical Systems (MEMS), 95-18*, The
Electrochemical Society, Pennington, NJ, (1995).

64. Lee, K. Y., LaBianca, N., Rishton, S. A., Zolghamain, S., Gelorme, J. D., Shaw, J.
and Chang, T. H.-P., *J. Vac. Sci. Technol. B*, **13**, 3012 (1995).

65. Andricacos, P. C., *J. Electrochem. Soc.,* **142**, 1824 (1995).

66. Wong, K. H. and Andricacos, P. C., *J. Electrochem. Soc.,* **137**, 1087 (1990).

67. Prentice, G., *Electrochemical Engineering Principles*; Prentice Hall: Englewood
Cliffs, 1991.

68. Nagai, Y., Senda, M. and Toshima, T., *J. Appl. Phys.,* **63**, 1136 (1988).

69. Bird, K. D. and Schlesinger, M., *J. Electrochem. Soc.,* **142**, L65 (1995).

70. Menezes, S. and Anderson, D. P., *J. Electrochem. Soc.,* **137**, 440 (1990).

71. Tench, D. M. and White, J. T., *J. Electrochem. Soc.,* **138**, 3757 (1991).

72. Schwartz, D. T., Stroeve, P. and Higgins, B. G., *AIChE J.,* **35**, 1315 (1989).

73. Schwartz, D. T., *J. Electrochem. Soc.,* **140**, 452 (1993).

74. Tribollet, B. and Newman, J., *J. Electrochem. Soc.,* **130**, 2016 (1983).

75. Schwartz, D. T., *J. Electrochem. Soc.,* **136**, 53C (1989).

76. Baker, B. C. and West, A. C., *J. Electrochem. Soc.,* **144**, 164 (1997).

77. Baker, B. C. and West, A. C., *J. Electrochem. Soc.,* **144**, 169 (1997).

78. Frazier, A. B. and Allen, M. G., *J. Microelectromech. Sys.,* **2**, 87 (1993).

79. Tench, D. M. and White, J. T., *J. Electrochem. Soc.,* **137**, 3061 (1990).

80. Tench, D. M. and White, J. T., *Metall. Trans. A,* **15A**, 2039 (1984).

APPENDIX A

Flow-Induced Composition Modulated NiFe Thin Films with Nanometer Scale Wavelengths

Summary

Described are results showing that an oscillating flow-field can induce spatially periodic composition variations in electrodeposited NiFe thin films. Flow-induced NiFe composition modulated alloys (CMAs) were deposited on the disk of a rotating ring-disk electrode (RRDE) by oscillating the RRDE rotation rate. Deposit composition profiles were analyzed using potentiostatic stripping voltammetry, which allowed the relationship between the alloy deposition parameters and CMA structure to be investigated. Results show that the composition modulation wavelength is inversely proportional to the flow oscillation frequency. CMAs made at disk oscillation frequencies greater than 100 mHz had modulation wavelengths less than 20 nm when plated galvanostatically at -10 mA/cm². Scanning tunneling microscopy images indicate that plating at different current densities leads to deposit growth front morphologies that influence the ability to resolve short wavelength compositional structure. The limitations of stripping voltammetry for composition depth profiling, and the implications of the results for the industrial plating of permalloy in paddle cells, are discussed.

Background

Electrodeposited $Ni_{81}Fe_{19}$ (Permalloy) thin films are used throughout the magnetic data storage industry [1-3]. The industrial plating of Permalloy is often performed in a paddle cell, where electrolyte agitation is accomplished by means of a reciprocating paddle assembly [1, 4-6]. Mass transfer in a paddle cell has two salient features: the time-averaged convective mass transfer rate is quite uniform over the entire cathode surface, and the transient convective mass transfer rate near the cathode oscillates periodically with large-amplitude excursions from the average rate [4-5]. The frequency of convective oscillations in a paddle cell is typically less than or approximately equal to 1 Hz, but this frequency can vary from position to position within the cell [5].

The elementary mechanistic steps in high rate NiFe electrodeposition are quite complex and subject to some uncertainty [7-9]. Nevertheless, the gross characteristics of

.

the process are agreed upon and involve iron and hydrogen being deposited near their mass transfer limited rate and nickel being controlled by kinetics [10]. Thus, by designing a paddle cell to deliver a uniform *time-averaged* convective mass transfer rate over the entire cathode, industrial electroplaters have ensured that their NiFe alloys will have the same *average* composition at each location on the cathode. However, systematic experimental studies of the effects of low-frequency *oscillating* convective mass transfer on NiFe electrodeposition have not been reported in the literature. Theoretical studies suggest that oscillating flow-fields can induce spatially-periodic composition modulations through an alloy deposit provided at least one species is mass transfer limited, one species is kinetics limited, and the flow oscillation period is longer than the concentration field relaxation time [11-12]. All of these conditions are satisfied by NiFe plating with flows that oscillate at sub-Hertz frequencies. Thus, it seems plausible that NiFe electrodeposited in an oscillating flow may form a flow-induced composition modulated alloy (CMA) with the modulation wavelength of the alloy being inversely related to the oscillation frequency of the flow-field.

In this investigation, we explore processing/structure relationships in NiFe thin films electrodeposited in the flow generated by a rotating ring-disk electrode (RRDE) with an oscillating rotation rate. We analyze the deposit composition profiles using stripping voltammetry [10, 13] and explore the limitations of the profiling technique when the deposition and stripping current distributions are nonuniform.

Experimental

A Pine Instruments RRDE with a platinum disk of radius $r_1 = 0.2286$ cm and a platinum ring with inner ring radius $r_2 = 0.2464$ cm and outer ring radius $r_3 = 0.2692$ cm was used in all electroplating and stripping voltammetry experiments. The RRDE, together with a large area platinum mesh counter electrode and a saturated calomel reference electrode (SCE), was used in a 200 ml single chambered electroplating and stripping vessel. The experimentally measured collection efficiency of the RRDE was N = 0.217, which compared well with the theoretical value of 0.219. A Pine Instruments model MSRX rotator was used to control the instantaneous rotation rate of the RRDE. The electrode rotator has rapid acceleration characteristics (>100,000 rpm/s) and its rotation rate was driven by an external voltage source (1000 rpm/V). A Wavetek function generator was used to control the RRDE rotation rate when a square wave

oscillation was needed. A Pine Instruments model AFRDE5 Bi-Potentiostat was interfaced to a Macintosh Centris 650 computer using a National Instruments 12-bit multifunction I/O board. Acquisition of the ring and disk current data was controlled by custom software written in LABVIEW 2.2.1.

Scanning tunneling microscopy (STM) images of NiFe films were acquired using a Digital Instruments Nanoscope II STM equipped with a 0.5 x 0.5 μm scanner head. The microscope was operated in air with mechanically cut platinum/rhodium (87% / 13%) tips in the constant current mode with a tunneling current of 0.5 nA. The bias voltage applied to the sample was 500 mV and the lateral scan rate was 8.68 Hz. A flatten filter in the y-direction was used in each image to reduce the effects of image bow. Electrodeposited NiFe samples for STM analysis were made using a platinum RDE with a removable electrode disk of 0.5 cm diameter. Four independent STM images were obtained for each NiFe thin film sample in order to calculate an average root mean square (RMS) roughness for each deposit.

The plating bath used in all experiments was chloride-based, with no additives, and was identical in composition to that used by Andricacos *et al.* [10]. Nickel and iron salts were added in a 40:1 molar ratio to a bath also containing sodium chloride and boric acid. The bath composition was 0.2 M $NiCl_2 \cdot 6H_2O$, 0.005 M $FeCl_2 \cdot 4H_2O$, 0.5 M NaCl and 0.4 M H_3BO_3 with a measured conductivity of 0.07 $ohm^{-1}cm^{-1}$. The plating bath was operated at room temperature with the pH adjusted between plating runs to 3.00 ± 0.02. A chloride-based stripping bath was used for all stripping voltammetry measurements. The stripping bath composition was 0.2 M HCl and 0.5 M NaCl, and had a measured conductivity of 0.11 $\Omega^{-1}cm^{-1}$. Both baths were prepared using reagent grade salts and 18 MΩ-cm deionized water. As discussed later, we found that the highest quality flow-induced CMAs were produced using plating baths that were allowed to "age" in an ambient environment for approximately four days prior to deposition.

NiFe thin films were plated galvanostatically onto the disk of the RRDE until a total charge of 500 mC had passed. During deposition, the ring potential was set to +800 mV *vs.* SCE to prevent plating on the ring. After each plating run, the RRDE was immersed and slowly rotated in deionized water to remove any residual plating bath components that could contaminate the stripping bath. The RRDE was then immersed in

the HCl/NaCl stripping bath and the NiFe film was oxidized potentiostatically (without ohmic compensation) at a disk potential of 0.0 mV *vs.* SCE, which ensured that the oxidation products liberated from the deposit were Fe^{+2} and Ni^{+2} [10]. The ring potential was set to +800 mV *vs.* SCE to further oxidize the liberated ferrous ions to ferric ions at their mass transfer limited rate, thereby allowing an analysis of the deposit composition. During stripping, the ring and disk currents were continuously recorded and the electrode was rotated steadily at 2500 rpm. The stripping voltammetry analysis we performed is similar to the method proposed by Andricacos *et al.* [10], except that we added additional NaCl supporting electrolyte and used potentiostatic stripping rather than potentiodynamic methods; the reasons for these modifications will become clear later.

Depth Profiling using Stripping Voltammetry

In stripping voltammetry, the average iron mole fraction ($\overline{X}_{Fe}$) in a NiFe thin film is found through the relationship [13]

$$\overline{X}_{Fe} = \frac{2}{N}\frac{Q_R}{Q_D} \quad , \tag{A.1}$$

where Q_D is the total disk charge needed to oxidize the metal film to its divalent state, Q_R is the total charge passed at the ring for the mass transfer limited oxidation of ferrous ion to ferric ion, and N is the steady state collection efficiency of the ring-disk electrode. Ideally, one should also be able to determine the instantaneous composition of the alloy at any time t_s during stripping by monitoring the instantaneous ring and disk currents, $i_R(t_s)$ and $i_D(t_s)$, respectively [1]. The relationship between the instantaneous stripping currents and the instantaneous composition follows directly from Eq. (A.1),

$$X_{Fe}(t_s) = \frac{2}{N}\frac{i_R}{i_D} \quad , \tag{A.2}$$

provided that the deposit is planar, the stripping current distribution is uniform, changes in i_R and i_D evolve slowly enough so that it is appropriate to use the steady state collection efficiency, and the deposit does not dealloy by selective etching of one species. The time-scales over which the ring response should remain quasi-steady can be estimated by knowing the transit time for a disk-generated species to cross the disk-ring gap [14]. For the geometry and rotation rate used in our system, the transit time is

approximately 20 ms, which is small compared to the time-scales we observe for variations in the disk current.

Obtaining a compositional depth profile also requires one to know the amount of alloy that has been stripped from the deposit at time t_s. Assuming that the molar volume of a NiFe alloy is given by the weighted average of the pure component molar volumes of Ni and Fe, $\hat{V}_{Ni}$ and $\hat{V}_{Fe}$, respectively, then the etched depth, $\delta(t_s)$, is written

$$\delta(t_s) = \frac{1}{A_D N F}\left(\hat{V}_{Fe}\int_0^{t_s} i_R\, dt + \hat{V}_{Ni}\left(\frac{N}{2}\int_0^{t_s} i_D\, dt - \int_0^{t_s} i_R\, dt\right)\right) , \qquad (A.3)$$

where A_D is the disk area and F is Faraday's constant.

Together, Eqs. (A.2) and (A.3) suggest that it is possible to determine a composition depth profile using stripping voltammetry. We will show that obtaining uniform deposition and stripping current distributions ultimately limits the depth profiling capabilities of stripping voltammetry when an RRDE is used.

Results and Discussion

The electroplated NiFe films prepared for these studies were deposited using two distinctly different classes of flow. Specifically, deposition occurred in either the steady flow of a steadily spinning RRDE or in the time-periodic flow of a RRDE with an oscillating rotation rate. Aside from the time-periodic flow induced by the oscillating RRDE, all deposition parameters were held constant in time.

Films deposited in a steady flow should mirror the results reported by Andricacos et al. [10], provided our bath "aging" procedure does not substantially alter the electrodeposition process. Table A.1 shows a comparison between our results and those of Andricacos et al. for two current densities and numerous steady disk rotation rates. The average composition results reported in Table A.1 deviate by no more than three mole percent from those reported by Andricacos et al., even though we used a modified stripping voltammetry procedure and the previously mentioned bath preconditioning. The average composition of each film was calculated using Eq. (A.1) by integrating the ring and disk currents until the disk current reached zero (all stripping curves had small

Table A.1. Average mole fraction iron, $\overline{X}_{Fe}$, in NiFe films plated at current density j and steady disk rotation rate Ω. All films were plated with a total charge of 500 mC.

j (mA/cm^2)	Ω (rpm)	$\overline{X}_{Fe}$	$X^{\dagger}_{Fe}$
-10	100	0.15	0.12
	400	0.22	0.22
	900	0.28	---
	1600	0.32	0.34
	2500	0.34	---
	3600	0.40	0.38
-20	100	0.08	0.06
	400	0.13	0.13
	900	0.19	---
	1600	0.22	0.23
	2500	0.25	---
	3600	0.28	0.31

† **Results from Andricacos et al. [10]**

cathodic background currents since O_2 was not sparged from the bath). The left side of Fig. A.1 shows typical potentiostatic stripping voltammetry ring and disk current data for NiFe deposits plated at -10 mA/cm^2 and steady rotation rates of 400, 1600, and 3600 rpm. The right side in Fig. A.1 shows the corresponding results determined using Eqs. (A.2) and (A.3). Notice in Eq. (A.3) and Fig. A.1 that the stripping depth is not necessarily linear with stripping time for these potentiostatic experiments, especially near the end of the stripping period. Also make note that nickel-enriched deposits strip more slowly than iron-enriched deposits.
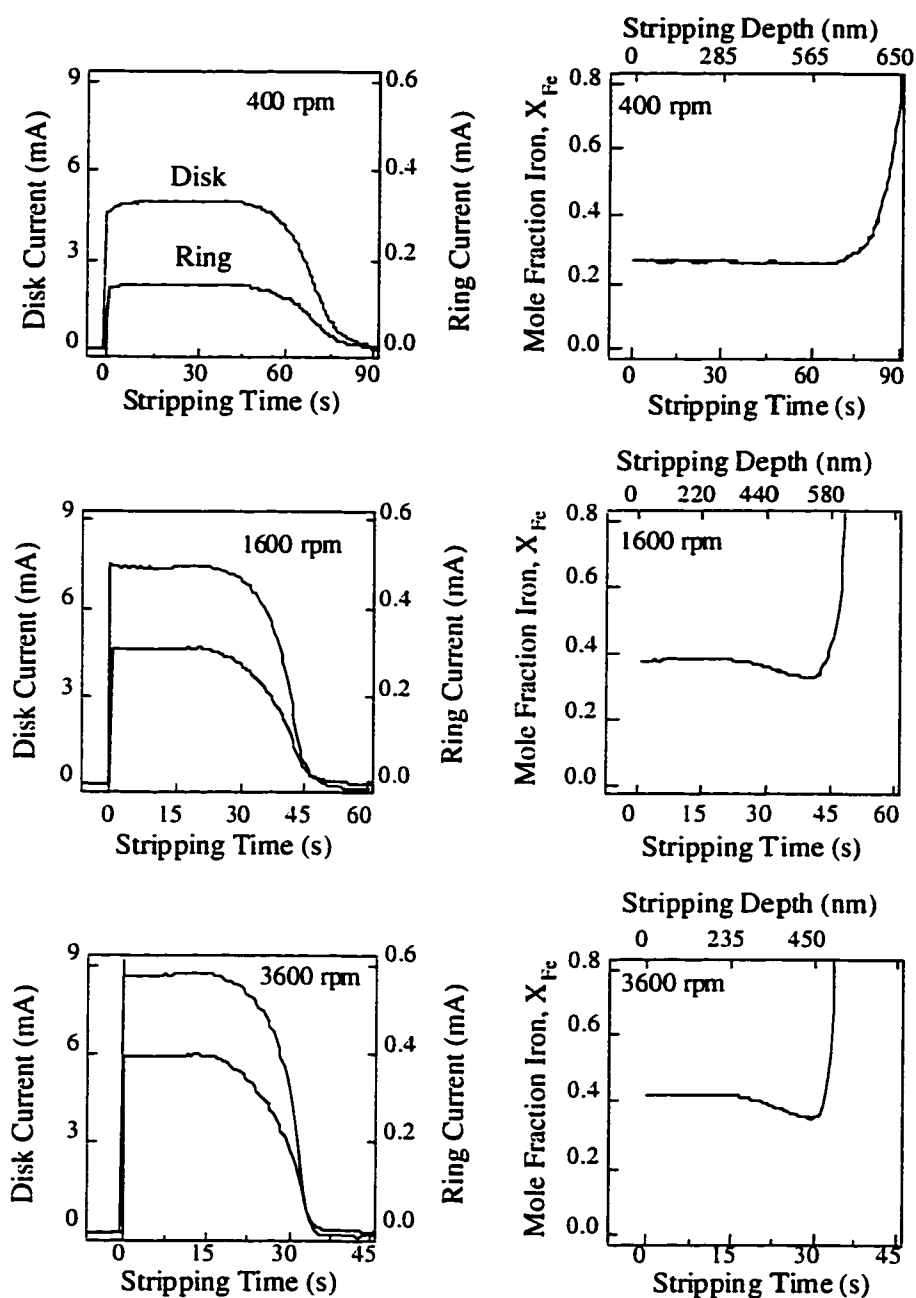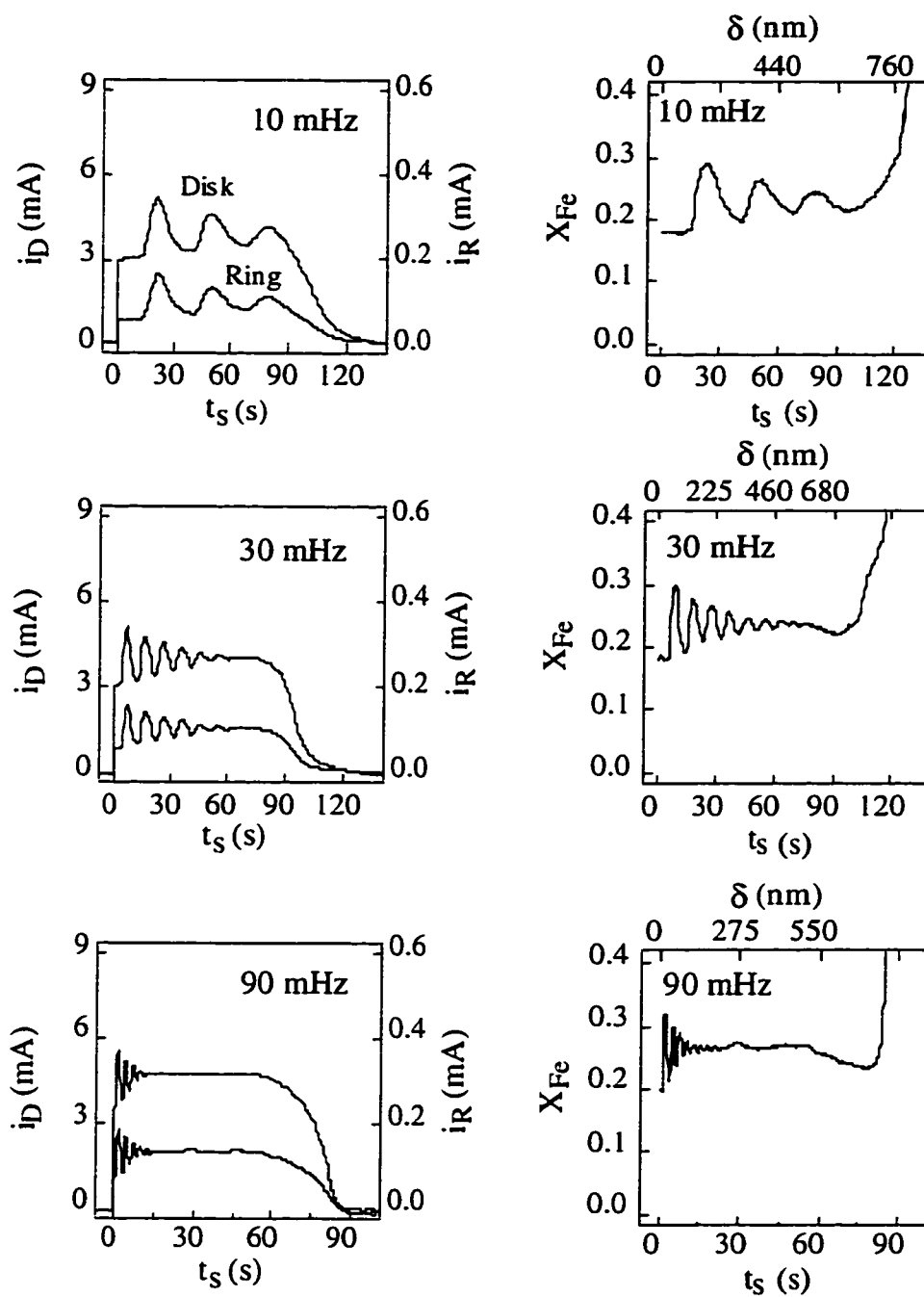
Figure A.1. Potentiostatic stripping curves for alloys plated galvanostatically using steady disk rotation rates of 400 (top), 1600 (middle), and 3600 rpm (bottom). Left hand column shows the disk and ring currents as a function of stripping time. Right hand column shows corresponding iron mole fraction and stripping depth calculated for each stripping curve. Electrodeposition conditions : -10 mA/cm^2.

Figures A.2 and A.3 show typical stripping voltammetry results for NiFe thin films that were electrodeposited at -10 mA/cm^2 in a time-periodic flow. During deposition, the rotation rate of the RRDE was oscillated with a square wave having minimum and maximum values of 400 and 3400 rpm, respectively. Oscillation frequencies investigated ranged from 10 to 300 mHz. The left side of Figs. A.2 and A.3 shows the ring and disk current stripping data and the right side of Figs. A.2 and A.3 shows the analyzed results found using Eqs. (A.2) and (A.3). Electrodeposition was always terminated during the 400 rpm leg of the square wave oscillation, just before the rotator sped up to 3400 rpm. Under potentiostatic stripping conditions, one finds clear oscillations in the disk and ring currents.

Three distinct features shown in Fig. A.1 and Table A.1 warrant detailed discussion. First, it is clear that the deposition rates for iron and hydrogen are sensitive to the mass transfer environment present during NiFe plating, as is well known [10]. The average iron mole fraction in the film increases from 0.22 to 0.40 and the current efficiency of the plating process decreases as the RRDE rotation rate is increased from 400 to 3600 rpm (the current efficiency can be seen indirectly by the relative thickness of each deposit). Second, near the completion of stripping, the apparent iron content of the alloy rises abruptly. This feature of the composition curve always exists, since the ring current response lags behind the disk current by the transit time across the gap. Thus, when the disk current drops to zero at the end of stripping, the ring will still measure a finite current, leading to an apparent iron mole fraction in excess of unity.

The most important feature shown in Fig. A.1, in that it relates directly to CMA fabrication and stripping voltammetry analysis, is the gradual fall in disk and ring currents and the associated downward drift in calculated iron mole fraction. For example, in Fig. A.1 (1600 rpm) the measured iron mole fraction is constant at 0.38 up to a stripping time of 20 s. At this point both disk and ring currents begin to fall. For a deposit of uniform thickness that is also stripped uniformly, we would expect the disk and ring currents to exhibit a steep cut-off at the point where the film was completely removed. The deviation of our data from this profile is likely due to nonuniformities in the plating and stripping current distributions on the disk electrode.

Figure A.2. Potentiostatic stripping curves for alloys plated galvanostatically using oscillating disk rotation frequencies of 10, 30 and 90 mHz (top to bottom). Left hand column shows the disk and ring currents as a function of stripping time. Right hand column shows corresponding iron mole fraction and stripping depth calculated for each stripping curve. Electrodeposition conditions : -10 mA/cm².
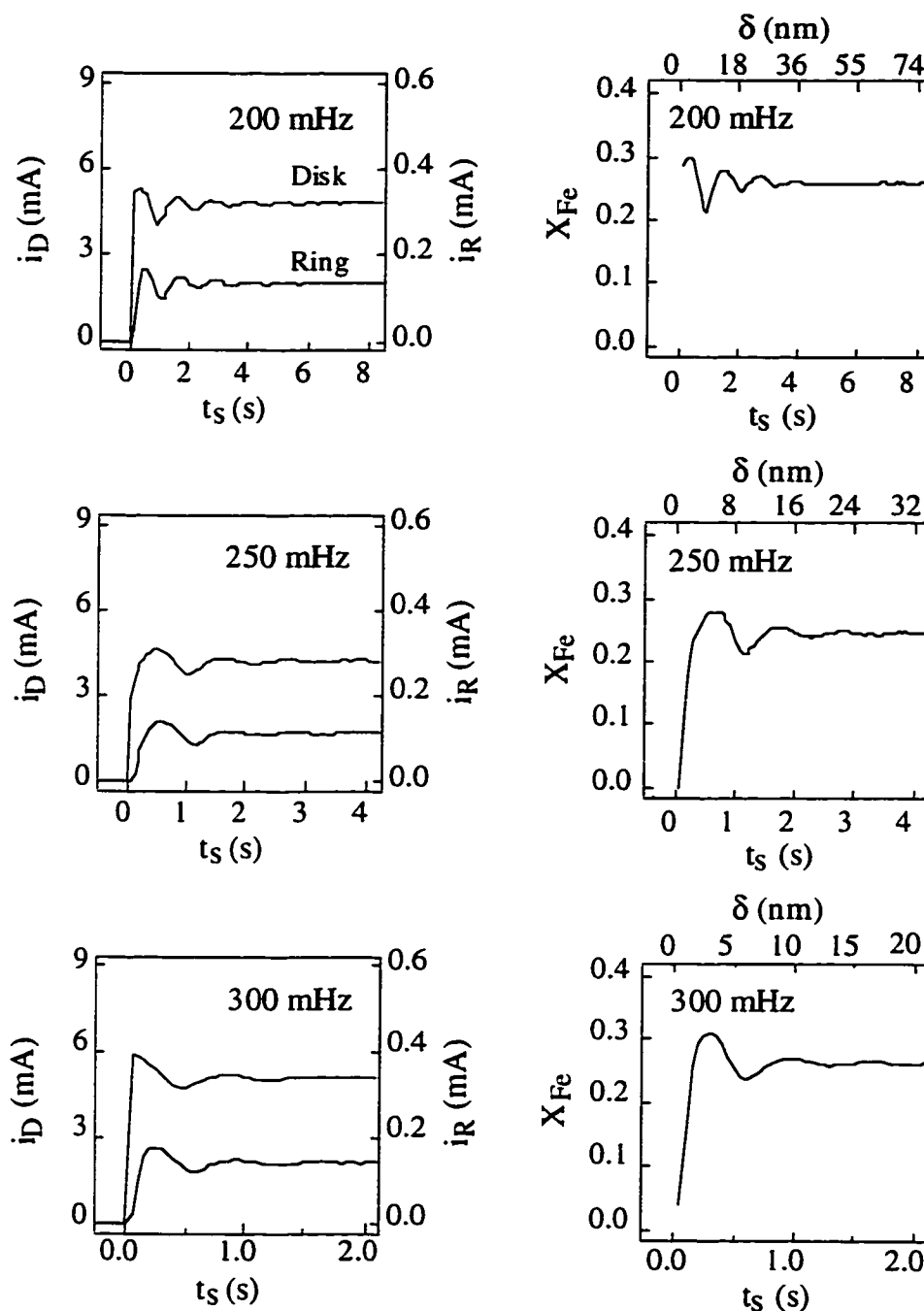
Figure A.3. Potentiostatic stripping curves for alloys plated galvanostatically using oscillating disk rotation frequencies of 200, 250 and 300 mHz (top to bottom). Left hand column shows the disk and ring currents as a function of stripping time. Right hand column shows corresponding iron mole fraction and stripping depth calculated for each stripping curve. Electrodeposition conditions : -10 mA/cm^2.

The extent and contribution of radial variations in plating current density are difficult to know for certain since a suitable description of the current distribution for plating with the NiFe system does not exist. However, one can estimate the uniformity of the secondary current distribution for a single electrode reaction [15] and then apply this theory to our case (in an approximate manner) by considering the partial currents independently, but using the total current density in calculating ohmic contributions. The partial current distribution for the reduction of Fe^{+2} and H^+ should be essentially uniform since both are limited by mass transfer to the disk [16]. Conversely, the reduction of Ni^{+2} takes place at currents where charge transfer kinetics are significant and ohmic drop through solution may contribute to nonuniformity. Using Ni^{+2}/Ni^o exchange current densities estimated from the work of Andricacos et al. [10], we found the RDE current distribution parameters (defined in [15]) to be approximately $J \rightarrow 0$, $\delta = 2.5$, and $N = 30$ (at 400 rpm) and $N = 85$ (at 3400 rpm) for plating at - 10 mA/cm^2. These numbers suggest that the Ni^{+2} partial current density may be approximately 20% greater at the edge of the disk than at the center during the plating of NiFe in our bath.

During stripping, the current distribution is likely to be even more nonuniform than during plating because of the significantly higher stripping currents used and the rapid oxidation kinetics. The conductivity of the stripping solution was adjusted to almost twice that of the plating bath in an effort to minimize ohmic nonuniformity, but the measured stripping currents were as much as five times larger than the plating currents. Stripping nonuniformity results in the removal of the film at the edges of the disk first; this effect is visually observable during stripping voltammetry experiments. For example, the time to reach a point where the disk edge has been completely stripped is about 20 s in Fig. A.1 (1600 rpm). At this point, the current signal (and iron composition) appear to slowly decrease. The slowly declining current at times > 20 s results from the stripping of a NiFe deposit away from the edge of the disk electrode. Visually, the deposit looks like a shrinking disk on top of the platinum substrate.

Figures A.2 and A.3 unambiguously show that the square wave rotation rate oscillation imposed during plating results in the deposition of a NiFe CMA. The disk current oscillates due to the suppressed oxidation rate of Ni-enriched layers and the ring current responds in tandem with the flux of ferrous ion liberated from the disk. As the flow oscillation frequency (σ) is increased, the CMA modulation wavelength (Λ) is seen

to decrease, as expected. However, Figs. A.2 and A.3 show that the peak-to-peak composition modulation amplitude (ΔX_{Fe}) appears to decline as etching progresses through the deposit. Normally, one expects the composition modulation to have well-defined lamellae near the disk, with progressively less defined layers as the deposit grows and the growth front becomes rougher. Figures A.2 and A.3 show the opposite effect. The decline in the peak-to-peak modulation amplitude is likely due to the nonuniform current distribution during stripping, since the further stripping progresses the more the etch-front becomes distorted. Thus, we use the very first modulation in each stripping curve to *estimate* the amplitude of the composition modulation (ΔX_{Fe}) throughout the alloy, keeping in mind that this likely represents a lower limit for the alloy as a whole. Nevertheless, in alloys with long wavelengths (see Fig. A.2, 10 mHz) it is possible to see that the composition modulations extend all the way through the film. It is worthwhile noting that the attenuated depth profile signal observed in Figs. A.2 and A.3 is characteristic of most destructive CMA profiling techniques, including ultrahigh vacuum methods [17-18]. Finally, the concentration profiles reported here should not be significantly skewed by ohmic coupling between the disk and ring, since the ring is operating on a well-defined mass transfer limited plateau and the potential due to coupling is calculated to be < 35 mV for our system [19].

The effect of plating current density on NiFe CMA formation is illustrated in Fig. A.4. As in Figs. A.2 and A.3, the RRDE rotation rate was oscillated between 400 and 3400 rpm and the disk and ring currents are represented as shown. Deposits were made using plating current densities of -5, -7.5, -10, and -20 mA/cm^2 at a disk oscillation frequency of 60 mHz. Figure A.4 illustrates that the best flow-induced CMAs are obtained when the films are plated in the vicinity of -10 mA/cm^2. At -5 mA/cm^2 no modulations are observed. This is consistent with the observation that at low current densities NiFe plating is not especially sensitive to agitation rate [10]. Conversely, at -20 mA/cm^2 NiFe is very sensitive to agitation rate, yet the quality of the CMAs (as measured by stripping voltammetry) is poor. One difference between the films plated at -10 mA/cm^2 and those plated at -20 mA/cm^2 is the film growth morphology. STM studies of NiFe thin films electrodeposited at -10 and -20 mA/cm^2 find that the deposit surfaces (*i.e.* the terminal growth fronts) exhibit average RMS roughnesses of 11 and 15 nm, respectively, after 500 mC of plating. Figure A.5 is a series of STM images which show the surface morphology of typical NiFe films made in our laboratory. For
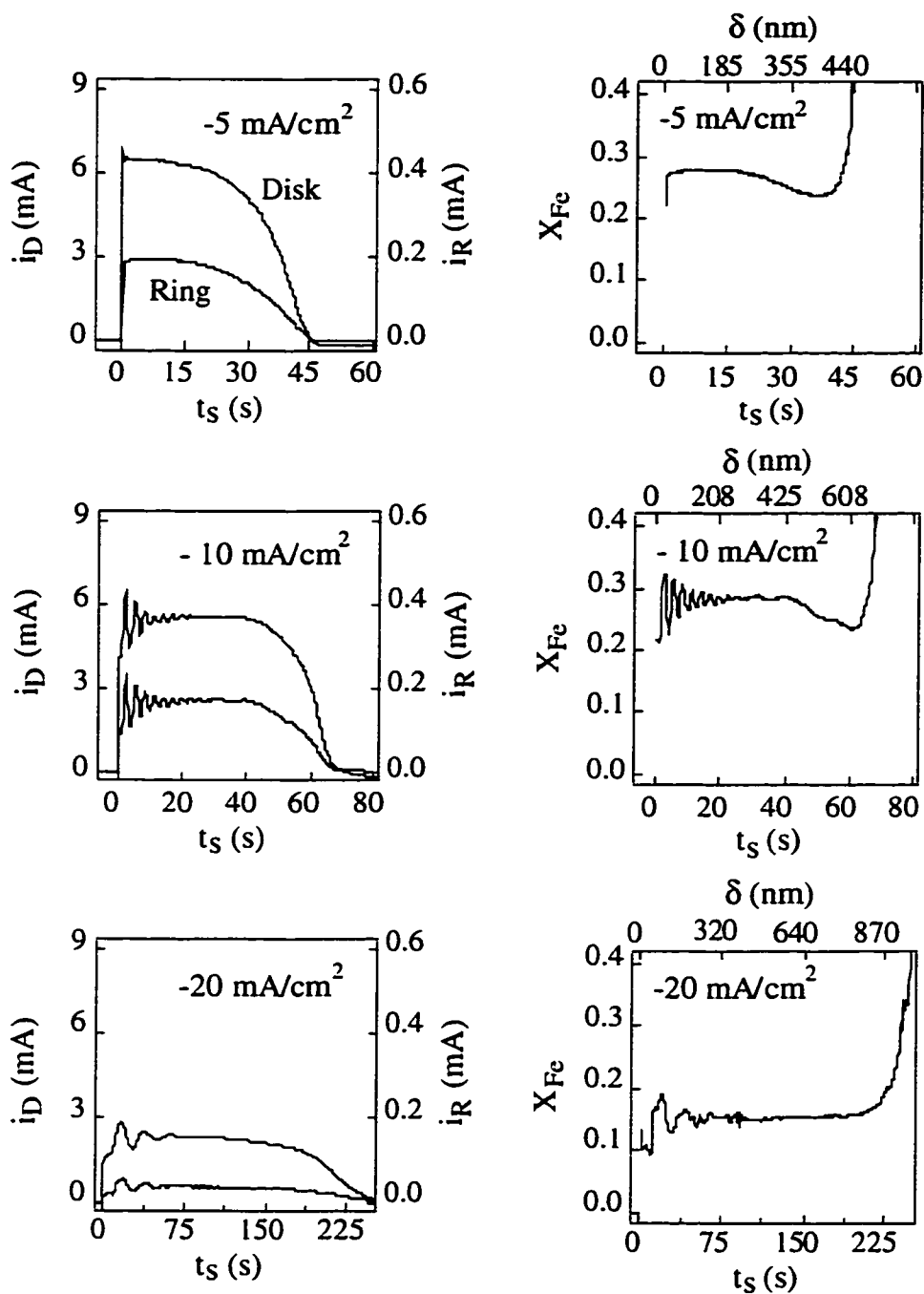
Figure A.4. Potentiostatic stripping curves for alloys plated galvanostatically using an oscillating disk rotation frequency of 60 mHz and plating densities of -5 (top), -10 (middle), and -20 mA/cm² (bottom). Left hand column shows the disk and ring currents as a function of stripping time. Right hand column shows corresponding iron mole fraction and stripping depth calculated for each stripping curve.
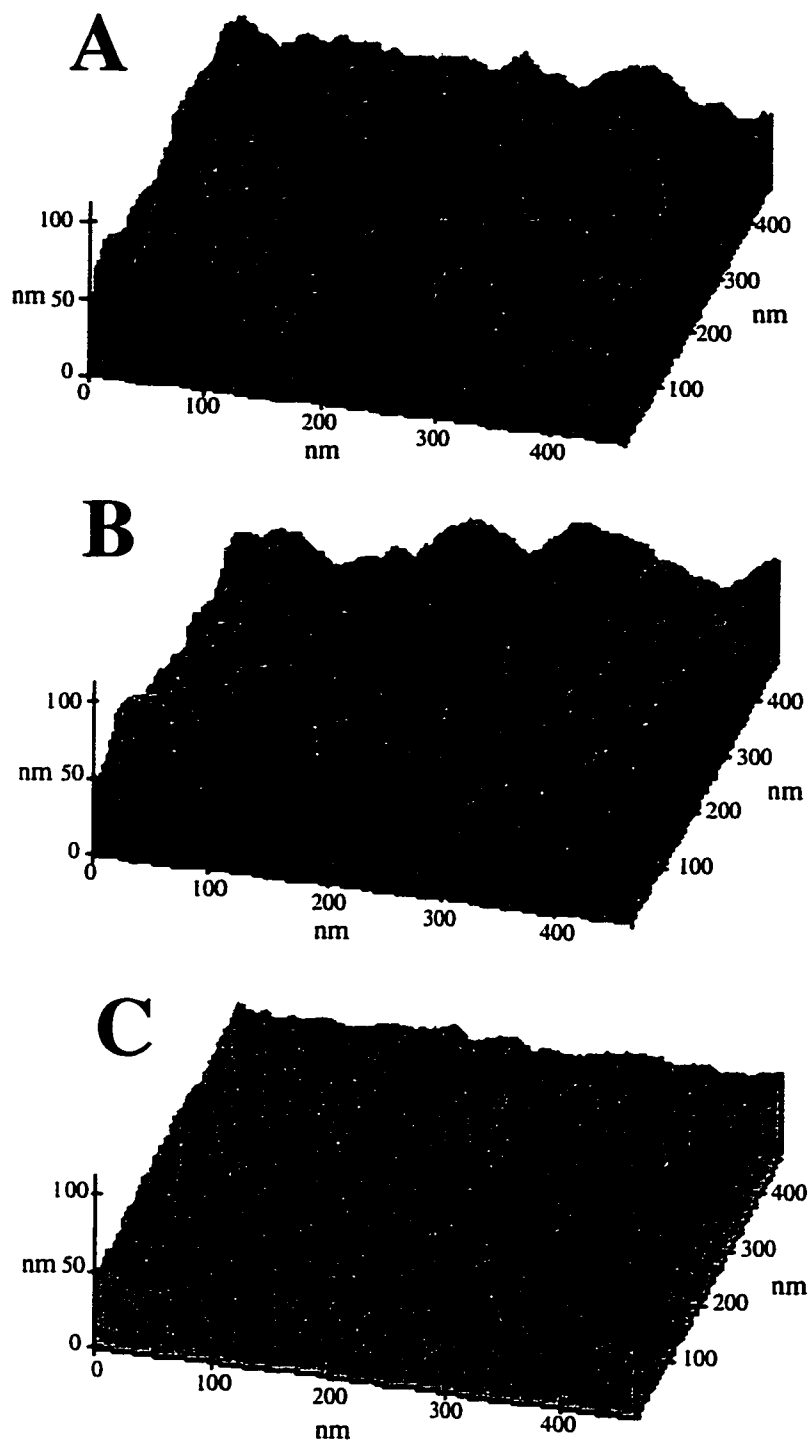
Figure A.5. Typical STM images of (A) NiFe plated at -10 mA/cm² with a 60 mHz flow oscillation, (B) NiFe plated at -20 mA/cm² with a 60 mHz flow oscillation and (C) polished platinum disk substrate.

reference, an image of a polished Pt disk substrate which exhibits a RMS roughness of ≈ 2 nm is included. Not only are the films made at -10 mA/cm^2 smoother, but they are characterized by finer grains and distinct crystalline features while those deposited at -20 mA/cm^2 appear to be comprised of larger, hemispherical growth centers.

In short, Figs. A.2, A.3 and A.4 show that flow-induced NiFe CMAs are formed, although there is some question about whether depth profiling using potentiostatic stripping is a quantitative or qualitative technique. Theoretically, one expects a flow-induced NiFe CMA to have a modulation wavelength (Λ) that follows the simple relationship

$$\Lambda = \left(\frac{\hat{V}_{NiFe}}{2F} \right) \frac{\eta j}{\sigma}, \tag{A.4}$$

where $\hat{V}_{NiFe}$ is the mean molar volume of the alloy, η is the plating current efficiency, j is the plating current density and σ is the oscillation frequency in Hz. The relationship between the measured CMA wavelength and the rotation rate oscillation frequency is summarized in Fig. A.6 (A). Figure A.6 (A) clearly shows that Λ has the expected inverse dependence on σ. In addition, doubling the plating current density increased the slope of the best-fit curve in Fig. A.6 (A) by slightly more than two-fold, reflecting the increased current efficiency found in NiFe plating at high current densities [10]. The CMAs made at the highest disk oscillation frequencies are characterized by nanometer-scale modulation wavelengths.

Plotted in Fig. A.6 (B) is the measured peak-to-peak composition modulation (ΔX_{Fe}) versus the CMA wavelength for alloys plated at - 10 mA/cm^2. The values of ΔX_{Fe} measured for -10 mA/cm^2 were highly reproducible (e.g. four replicates at 60 mHz had a range of $0.10 < \Delta X_{Fe} < 0.14$), but those obtained at different plating current densities were found to be rather scattered (as suggested by Fig. A.4). The data in Fig. A.6 (B) show that the measured CMA amplitude drops off for very short (< 20 nm) wavelengths. Theory for flow-induced CMA formation suggests that the amplitude of the modulation should decrease when the flow-field oscillation period becomes comparable to the concentration field relaxation time [11-12], but even the highest oscillation
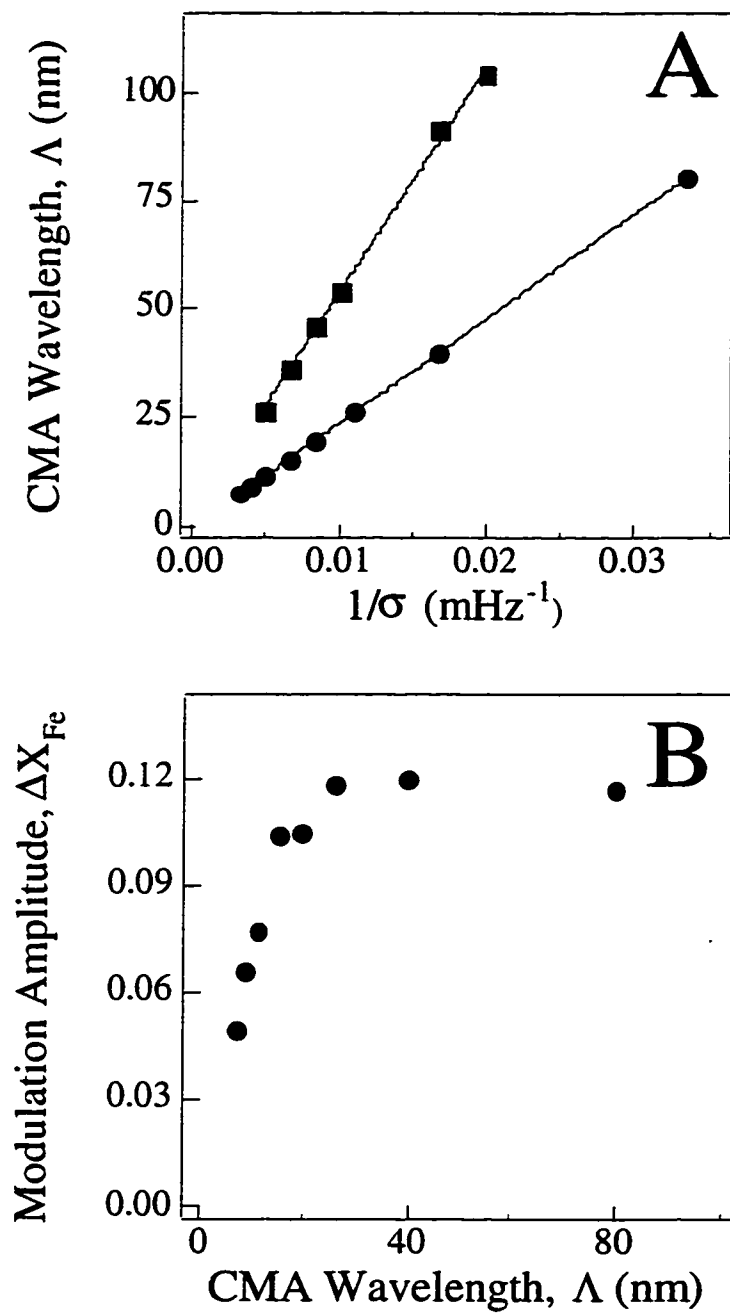
Figure A.6. (A) Dependence of NiFe CMA wavelength on flow oscillation frequency (j = -10 and -20 mA/cm²). (B) Measured CMA amplitude as a function of the CMA wavelength (j = -10 mA/cm²).

frequencies used here are too small for these effects to be important. Rather, an examination of the deposit growth front morphology (Fig. A.5) offers a better explanation for the decline in ΔX_{Fe} when $\Lambda \leq 20$ nm. When the magnitude of surface roughness becomes comparable to Λ, resolving the compositional variation in the film becomes difficult, leading to the decline in ΔX_{Fe} observed in the small-wavelength data of Fig. A.6 (B). The shortest wavelength flow-induced CMAs we made and were able to resolve were 7 nm. From the results in Fig. A.6, it appears stripping voltammetry provides a rapid method for obtaining characteristic values of Λ, but is less reliable for ΔX_{Fe}.

A final interesting aspect of flow-induced CMA fabrication was the observed plating bath performance. As mentioned previously, we found throughout the course of experimentation that the plating electrolyte would reach an optimum "age" from which the smallest modulation wavelengths were obtained. As originally formulated the bath would perform poorly for CMA deposition, but with time the performance would improve and plateau, leading to well-defined CMAs with $\Lambda < 10$ nm. As time progressed and more films were deposited from the electrolyte, the bath would start to produce CMAs of lesser quality. No effort was made to correlate the electrolyte's ability to form fine structured, flow-induced CMAs with time, exposure to the atmosphere or the number of plating runs, but it is likely that the formation of Fe^{+3} by atmospheric oxygen and the oxidation of Fe^{+2} at the counter electrode played some role [20]. It is also possible that the electrolysis of trace impurities may influence the electrodeposition process as well.

Conclusions

Flow-induced composition modulated NiFe alloys are formed over a range of deposition current densities when the flow-field is subjected to sub-Hertz oscillations. These conditions are routinely employed in the industrial manufacture of magnetic devices, so it is quite possible that NiFe alloys plated in the paddle cell have nanometer-scale composition modulations. It remains to be seen what effect, if any, this flow-induced compositional structure might have on the properties of NiFe materials.

References

1. Andricacos, P. C. and Romankiw, L. T. In *Advances in Electrochemical Science and Engineering*; H. Gerischer and C. W. Tobias, Ed.; VCH: New York, 1994; Vol. 3; pp 227.

2. Judy, J. H., *MRS Bull.*, **15**, 63 (1990).

3. Jagielinski, T., *MRS Bull.*, **15**, 36 (1990).

4. Rice, D. E., Sundstrom, D., McEachern, M. F., Klumb, L. A. and Talbot, J. B., *J. Electrochem. Soc.*, **135**, 2777 (1988).

5. Schwartz, D. T., Higgins, B. G. and Stroeve, P., *J. Electrochem. Soc.*, **134**, 1639 (1987).

6. Castellani, E. E., Powers, J. V. and Romankiw, L. T., *U.S. Patent 4 102 756*, (1978).

7. Matlosz, M., *J. Electrochem. Soc.*, **140**, 2272 (1993).

8. Hessami, S. and Tobias, C. W., *J. Electrochem. Soc.*, **136**, 3611 (1989).

9. Dahms, H. and Croll, I. M., *J. Electrochem. Soc.*, **112**, 771 (1965).

10. Andricacos, P. C., Arana, C., Tabib, J., Dukovic, J. and Romankiw, L. T., *J. Electrochem. Soc.*, **136**, 1336 (1989).

11. Schwartz, D. T., Stroeve, P. and Higgins, B. G., *AIChE J.*, **35**, 1315 (1989).

12. Schwartz, D. T., *J. Electrochem. Soc.*, **136**, 53C (1989).

13. Andricacos, P. C., Tabib, J. and Romankiw, L. T., *J. Electrochem. Soc.*, **135**, 1172 (1988).

14. Bard, A. J. and Faulkner, L. R., *Electrochemical Methods*; John Wiley and Sons: New York, 1980.

15. Newman, J., *J. Electrochem. Soc.*, **113**, 1235 (1966).

16. White, R. and Newman, J., *J. Electroanal. Chem.*, **82**, 173 (1977).

17. Cohen, U., Koch, F. B. and Sard, R., *J. Electrochem. Soc.*, **130**, 1987 (1983).

18. Yahalom, J. and Zadok, O., *J. Mater. Sci.*, **22**, 499 (1987).

19. Miksis, J. J. and Newman, J., *J. Electrochem. Soc.*, **123**, 1030 (1976).

20. Grande, W. C. and Talbot, J. B., *J. Electrochem. Soc.*, **140**, 669 (1993).

Vitae

Steven David Leith

Education

University of Washington, Seattle, Washington
Ph.D. Chemical Engineering; November, 1998
Electrodeposition of NiFe 3-D Microstructures

University of Colorado, Boulder, Colorado
M.S. Chemical Engineering; December, 1993
Sulfur Transport in Limestone : A Model for Prediction of Sulfate Accumulation in Field Exposed Briquettes

University of Washington, Seattle, Washington
B.S. Chemical Engineering; June, 1991

Publications

Leith, S.D. and Schwartz, D.T., "*In-Situ* Fabrication of Sacrificial Layers in Electrodeposited NiFe Microstructures, *J. Micromech. Microeng.*, (submitted December, 1998)

Leith, S.D. and Schwartz, D.T., "Through-Mold Electrodeposition using the Uniform Injection Cell (UIC) : Workpiece and Pattern Scale Uniformity", *Electrochim. Acta*, (submitted December, 1998)

Leith, S.D. and Schwartz, D.T., "High Rate Through-Mold Electrodeposition of Thick (>200 µm) NiFe MEMS Components with Uniform Composition", *J. Microelectromech. Sys.*, (submitted September, 1998)

Leith, S.D., Ramli, S. and Schwartz, D.T., "Characterization of Ni_xFe_{1-x} ($0.10 \leq x \leq 0.95$) Electrodeposition from a Family of Sulfamate-Chloride Electrolytes", *J. Electrochem. Soc.* (in press)   .

Leith, S.D., Wang, W. and Schwartz, D.T., "Characterization of Compositional Structure in Flow-Induced NiFe CMAs", *J. Electrochem. Soc.* Vol. 145, 2827-2833, (1998)

Leith, S.D., Schwartz, D.T. and Deng, K., "Development of an Electroplating Process for High Throughput, High Yield Manufacturing of Magnetic Components", *Technical Digest 1998 Solid-State Sensor and Actuator Workshop*, Hilton Head, SC June 8-11, 245-247, Transducer Research Foundation, Cleveland (1998)

Leith, S.D. and Schwartz, D.T., "Fabrication and Characterization of NiFe Thin Film Composition Modulated Alloys", in *Electrochemical Synthesis and Modification of Materials*, Corcoran, S.G., Searson, P.C., Moffat, T.P. and Andricacos, P.C. (eds.), Materials Research Society, Pittsburgh, PA (1997)
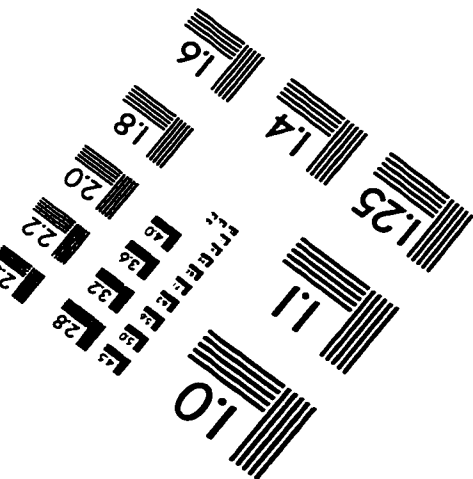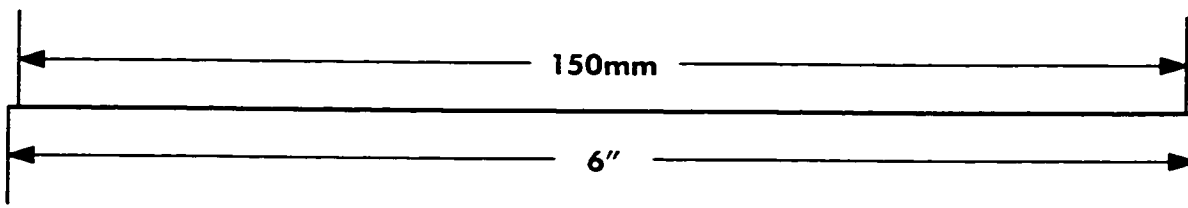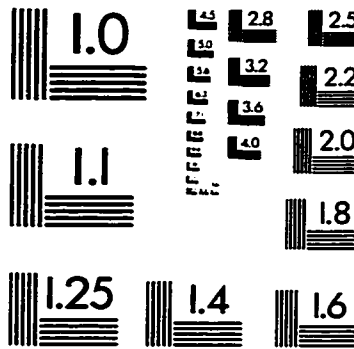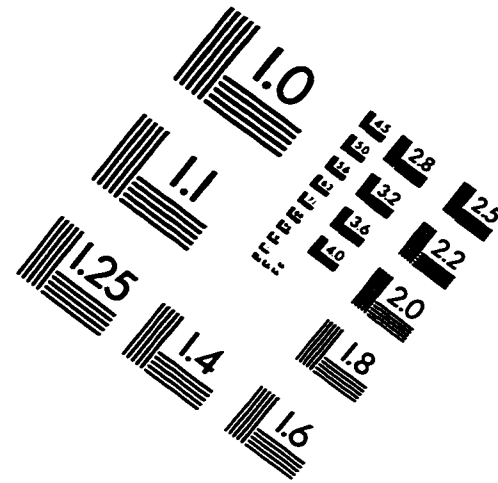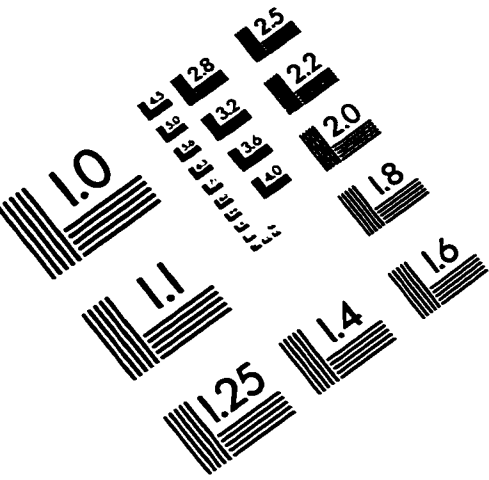
Leith, S.D., Reddy, M.M. and Ramirez, W.F. "Modeling Damage to Limestone Exposed to Atmospheric Pollutants", in *Material Issues in Art and Archaeology V*, Vandiver, P.B., Druzik, J.R., Merkel, J. and Stewart, J. (eds.), Materials Research Society, Pittsburgh, PA (1997)

Leith, S.D. and Schwartz, D.T., "Characterization of NiFe Multilayers Plated in an Oscillating Flow", in *Electrochemically Deposited Thin Films III*, Paunovic, M. (ed.), The Electrochemical Society, Pennington, NJ (1997)

Leith, S.D., Reddy, M.M., Ramirez, W.F. and Heymans, M.J., "Limestone Characterization to Model Damage from Acidic Precipitation : Effect of Pore Structure on Mass Transfer", *Environ. Sci. Technol.*, Vol. 30, No. 7, 2202-2210 (1996)

Leith, S.D. and Schwartz, D.T., "Flow Induced Composition Modulated NiFe Thin Films with Nanometer Scale Wavelengths", *J. Electrochem. Soc.*, Vol. 143, 873-878, (1996)

IMAGE EVALUATION
TEST TARGET (QA-3)

150mm

6"